STUDIES OF 20 < A < 30 NUCLEOSYNTHESIS

IN

AGB STARS AND NOVAE

By
KIANA SETOODEHNIA, B.Sc.
B.Sc, Shiraz University, 2004

A Thesis
Submitted to the School of Graduate Studies
in Partial Fulfillment of the Requirements
for the Degree
Master of Science

McMaster University

MASTER OF SCIENCE (2007) McMaster University
(Physics) Hamilton, Ontario

TITLE: Studies of $20 < A < 30$ Nucleosynthesis in AGB Stars and Novae
AUTHOR: Kiana Setoodehnia, B.Sc. (Shiraz University)
SUPERVISOR: Professor Alan A. Chen
NUMBER OF PAGES: xv, 146

STUDIES OF $20 < A < 30$ NUCLEOSYNTHESIS IN AGB STARS AND NOVAE

Abstract

In this thesis, a variety of topics are investigated. Part I discusses asymptotic giant branch (AGB) stars. We review their evolution and their contribution to the galactic chemical evolution. We particularly pay attention to the nucleosynthesis in different layers of the AGB stars, and discuss diverse chains of reactions that can happen under different circumstances.

Out of many of such reactions, three are the subjects of our special attention. The ^{23}Na(p,α)^{20}Ne, ^{23}Na(p,γ)^{24}Mg and ^{26g}Al(p,γ)^{27}Si reactions are important reactions that are part of the NeNa and MgAl cycles. Their reaction rates used to be uncertain by orders of magnitude, and thus have been subjects of investigation. Recently, there has been new experimental information released on these reactions. In this project, we have used this new information, and have calculated the new reaction rates for those reactions. The results show less uncertainty range in all three reaction rates compared to the prior measurements.

We then have used these new less uncertain rates to calculate the AGB yields of hydrogen through to ^{62}Ni. However, these reaction rates only affect the yields of Ne to Si isotopes noticeably, which are presented in Appendix A. Dr. Karakas has calculated the AGB yields by computing stellar evolution and nucleosynthesis models for a 6 $M_{\odot}$ AGB star with three different metallicities (Z = 0.02, 0.004 and 0.008) using the new reaction rates. The results show that the changes in the yields due to individually using the updated ^{23}Na(p,γ)^{24}Mg or ^{23}Na(p,α)^{20}Ne reaction rate are

noticeable for some isotopes. However, these new reaction rates result in completely opposite changes in most of the yields; moreover, the updated ^{26g}Al(p,γ)^{27}Si reaction rate has no effect on any of the stellar yields except on the yield of ^{28}Si obtained by the $Z = 0.02$ model. Thus, by using all three new reaction rates simultaneously in the nucleosynthesis network, we only see major changes for a few isotopes, e.g. significant destruction of ^{20}Ne and considerable production of ^{23}Na, ^{24}Mg and ^{28}Si. There is no noticeable effect on any of the remaining AGB yields.

Part II of this project discusses the significance of studying the nuclear structure of ^{26}Si and ^{30}S, which are not yet well understood. We discuss classical novae and their nucleosynthesis. We pay attention to some reactions, whose rates are still uncertain, e.g. the ^{25}Al(p,γ)^{26}Si, and ^{29}P(p,γ)^{30}S reactions. To lower the uncertainty range in such reaction rates, the structure of ^{26}Si and ^{30}S should be better understood.

We have carried out an experiment at Wright Nuclear Structure Laboratory (WNSL) at Yale University to be able to determine whether or not further studies of the structure of ^{26}Si and ^{30}S can be pursued by the (^{12}C,^{6}He) reaction mechanism. We investigated the ^{20}Ne(^{12}C,^{6}He)^{26}Si and ^{12}C(^{24}Mg,^{6}He)^{30}S reactions. The time for collecting the data for the whole experiment was only about five days. Taking into consideration the number of experiments that were done in five days, some of them resulted in low statistics. The ^{20}Ne(^{12}C,^{6}He)^{26}Si experiment gave a null result. This is due to the fact that the target that was used was old, and the ^{20}Ne in that target has been diffused out. Thus, we could not determine whether the (^{12}C,^{6}He) reaction mechanism proves to be a good method to study the structure of ^{26}Si. As for the nuclear structure of ^{30}S, we could see the ground state and the first excited state. The time was not enough to collect enough data to be able to determine this structure; however, the (^{12}C,^{6}He) reaction mechanism for studying the structure of ^{30}S looks promising.

To My Parents

&

In the Memory of My Uncle, Hooshang Hooshidar

Acknowledgments

There are many people I would like to thank, who have directly and indirectly helped me achieve this degree and finish this project. Their support is greatly acknowledged. Paramountly, with a deep sense of appreciation, I would like to express my sincere thanks to my supervisor, Dr. Alan A. Chen, for giving me the opportunity to enter the graduate program at McMaster University. My first year in graduate school was tough, but his immense multidimensional friendly help and support has motivated me to pursue my studies. I would like to thank him for his advantageous advice over the past two years. I appreciate his valuable suggestions and assistance during the course of this work, which would not have been possible without him.

I would also like to genuinely thank the members of my committee, Prof. Jim Waddington and Dr. Alison Sills, for their guidance and their support. Furthermore, I am very grateful to Prof. Peter Parker for his extended direction of the experimental part of this project. His profound knowledge has helped me learn many things about data analysis procedure and things that are relevant to Nuclear Astrophysics. As well, I would like to thank Dr. Reza Nejat, whose moral support has always helped me overcome the problems of living far away from my family in a different environment.

Extra deep thanks to Dr. Amanda I. Karakas for carrying out very important computational work regarding to computing the stellar nucleosynthesis models of AGB stars to determine the effect of proton capture reaction rate uncertainties on the resultant stellar yields. She has also provided us with 6 different plots regarding

to surface abundances of different species and percentage differences between different sets of yields. These plots are shown in chapter 3 and Appendix A, respectively. The first part of this work would not have been done without her help.

I would also wish to express my thanks to the post-doctoral researcher at Yale University, Dr. Jason Clark, and also to Catherine Deibel and Chris Wrede, current PhD students in Nuclear Astrophysics group at Yale University, for teaching me how to work with the data analysis software, and many other techniques with which the data analysis could be done; and also for participating in taking long day and night shifts during our experiment at Yale. They have also provided me with the sort routine, with which we analyzed our experimental data.

Special thanks to my colleagues Christian Ouellet, Jun Chen and Daid Kahl, who are graduate students in our team. They have constantly assisted me in learning more about computer-related matters and even English; and for their friendship and their encouragement over the past years.

Further thanks go to the staff members of our department, Daphne Kilgour , Tina Stewart , Mara Esposto, Cheryl Johnston, and Rosemary McNeice. They have helped to provide a very joyful environment, in which graduate students including me can do research in the best way possible.

Finally, I am profoundly grateful to my family: my parents, Sirous and Parvin Setoodehnia, my siblings, Kambiz and Katayoon, and to my friends, Maryam Rokh bakhsh, Mehran Hooshidar, Beile Gao and many others all around the world. I could not survive the graduate school in a foreign country without their encouragement and their support. The motivation they have given me to accomplish what I always wished for is sincerely acknowledged.

This work was funded by National Science and Engineering Research Council of Canada.

Table of Contents

Abstract iii

Acknowledgments vi

List of Figures xi

List of Tables xiv

I Nuclear Reaction Rates and Their Impact on the AGB Yields 1

Chapter 1
AGB Phase of Evolution 2
Introduction 2
1.1 Evolution of Low- to Intermediate-Mass Asymptotic Giant Branch Stars 4
1.2 Early AGB Phase of Evolution 5
1.3 The Thermally Pulsing Phase 7
1.4 Nucleosynthesis in AGB Stars 9
1.4.1 Nucleosynthesis during the TP-AGB Phase of Evolution; He-Burning Shell and s-Process Nucleosynthesis 10
1.4.2 Nucleosynthesis during the Interpulse Phase of Evolution in AGB Stars; H-Burning Shell and the Hot Bottom Burning . . 12
1.4.2.1 The CNO Cycle 14
1.4.2.2 The NeNa Cycle 15

1.4.2.3 The MgAl Cycle 16
1.4.3 The Third Dredge-up Process 18
1.5 Termination of the AGB Evolutionary Phase 19
1.6 The Roles of the AGB Stars 20

Chapter 2
Stellar Thermonuclear Reaction Rates **22**
2.1 Overview 22
2.2 Stellar Thermonuclear Reaction Rate Mechanism 24
2.3 Non-Resonant Reaction Rates 30
2.4 Resonant Reaction Rates 34

Chapter 3
The Impact of Reaction Rates on AGB Yields **38**
3.1 Stellar Yield Calculation 38
3.2 Stellar Yield Uncertainties 40
3.3 Nuclear Reaction Rates 42
3.3.1 The ^{23}Na(p,α)^{20}Ne Reaction Rate 43
3.3.2 The ^{23}Na(p,γ)^{24}Mg Reaction Rate 50
3.3.3 The ^{26g}Al(p,γ)^{27}Si Reaction Rate 55
3.4 Summary of the Yield Results 61
3.5 Future Work 69

II Nuclear Level Structure and its Impact on Novae Nucleosynthesis **70**

Chapter 4
Astrophysical Importance of ^{26}Si and ^{30}S **71**
4.1 Classical Novae 71
4.2 Properties of Classical Novae 73
4.3 Nucleosynthesis in Classical Novae and Their Role in the Galactic Alchemy 74
4.4 Motivations behind Studying the Nuclear Structure of ^{26}Si and ^{30}S 75
4.4.1 Recent Measurements of the ^{26}Si Level Structure 77
4.4.2 Recent Measurements of the ^{30}S Level Structure 81

Chapter 5
Experimental Details **84**
5.1 The Yale ESTU Tandem Van de Graaff Accelerator 84
5.2 Beams and Targets 86
5.3 The Yale Split-Pole Magnetic Spectrograph 87
5.4 The Focal Plane Detector 89
5.5 Electronics 92
5.6 The Data Acquisition System 92

Chapter 6
Analysis and Results **95**
6.1 Particle Identification 95
6.2 The ^{20}Ne(^{12}C,^{6}He)^{26}Si Experiment 100
6.3 The ^{12}C(^{24}Mg,^{6}He)^{30}S Experiment 113
6.4 Future Work 118

Chapter 7
Conclusion **120**

Appendix **122**

Appendix A
Stellar Yields **122**

Bibliography **146**

List of Figures

1.1 Post-main sequence evolutionary tracks for 1, 5 and 10 solar mass stars. 6
1.2 Schematic diagram of the structure of an AGB star. 8
1.3 Schematic evolution of an AGB star through two thermal pulse cycles. 9
1.4 Schematic diagram of the He- and H-shells in an AGB star. 12
1.5 Schematic diagram of the NeNa cycle. 16
1.6 Schematic diagram of the MgAl cycle. 17

2.1 The Maxwell-Boltzmann energy distribution of a gas characterized by a temperature T. 29
2.2 The Gamow peak and the Gamow window. 33

3.1 The reevaluated ^{23}Na(p,α)^{20}Ne reaction rate as a function of temperature. 48
3.2 The uncertainty range in the reevaluated ^{23}Na(p,α)^{20}Ne reaction rate as a function of temperature. 48
3.3 The reevaluated ^{23}Na(p,γ)^{24}Mg reaction rate as a function of temperature. 51
3.4 The uncertainty range in the ^{23}Na(p,γ)^{24}Mg reaction rate as a function of temperature. 52
3.5 The reevaluated ^{26g}Al(p,γ)^{27}Si reaction rate as a function of temperature. 57
3.6 The uncertainty range in the ^{26g}Al(p,γ)^{27}Si reaction rate as a function of temperature. 57
3.7 The time variation of selected surface abundances for the 6 $M_\odot$, Z = 0.004 model using the standard set of reaction rates. 66
3.8 The time variation of selected surface abundances for the 6 $M_\odot$, Z = 0.004 model using the updated ^{23}Na(p,γ)^{24}Mg reaction rate. 67

3.9 The time variation of selected surface abundances for the 6 $M_{\odot}$, Z = 0.004 model using the updated ^{23}Na(p,α)^{20}Ne reaction rate. 68

4.1 Anatomy of the classical nova outburst. 72
4.2 The level scheme of ^{26}Si. 78
4.3 The level scheme of ^{30}S. 83

5.1 Schematic diagram of the layout of WNSL. 85
5.2 Schematic diagram of the Enge split-pole spectrograph. 88
5.3 Schematic diagram of the focal plane detector. 91
5.4 Schematic diagram of the electronics used in our experiment. 93

6.1 Particle simulations for the Cathode vs. Scintillator plot at $E_{\rm beam}$ = 80 MeV in the ^{12}C(^{12}C,^{6}He)^{18}Ne reaction. 96
6.2 The Rear Position vs. Front Position histogram for the ^{12}C(^{12}C,^{6}He)^{18}Ne reaction at $\theta^{\rm lab} = 5^{\circ}$ and 80 MeV beam energy. 97
6.3 Cathode vs. Scintillator, Cathode vs. Front Position and Scintillator vs. Front Position 2D histograms for the ^{12}C(^{12}C,^{6}He)^{18}Ne reaction at $E_{\rm beam}$ = 80 MeV. 98
6.4 The effect of 2D gates on different histograms. 99
6.5 The ^{6}He momentum spectrum corresponding to the ^{26}Si states from the ^{20}Ne(^{12}C,^{6}He)^{26}Si reaction at $\theta^{\rm lab} = 5^{\circ}$ and $E_{\rm beam}$ = 70 MeV. . . . 101
6.6 Cathode vs. Scintillator 2D histogram for the ^{12}C(^{12}C,^{6}He)^{18}Ne reaction at $E_{\rm beam}$ = 70 MeV. 102
6.7 The ^{6}He momentum spectrum corresponding to the ^{18}Ne states from the ^{12}C(^{12}C,^{6}He)^{18}Ne reaction at $\theta^{\rm lab} = 5^{\circ}$ and $E_{\rm beam}$ = 70 MeV. . . . 103
6.8 The spectrum of ^{18}Ne from the ^{12}C(^{12}C,^{6}He)^{18}Ne experiment done by Hahn *et al.* 104
6.9 The ^{6}He momentum spectrum corresponding to the ^{18}Ne states from the ^{12}C(^{12}C,^{6}He)^{18}Ne reaction at $\theta^{\rm lab} = 5^{\circ}$ and $E_{\rm beam}$ = 80 MeV. . . . 106
6.10 The spectrum achieved by gating around the ^{6}He particles in the ^{20}Ne(^{12}C,^{6}He)^{26}Si reaction at $\theta^{\rm lab} = 5^{\circ}$ and $E_{\rm beam}$ = 80 MeV. 109
6.11 The spectrum achieved by gating around the ^{6}He particles in the ^{13}C(^{12}C,^{6}He)^{19}Ne reaction at $\theta^{\rm lab} = 5^{\circ}$ and $E_{\rm beam}$ = 80 MeV. 110
6.12 The spectrum achieved by gating around the scattered ^{12}C particles in the ^{20}Ne(^{12}C,^{12}C)^{20}Ne scattering experiment at $\theta^{\rm lab} = 15^{\circ}$ and $E_{\rm beam}$ = 80 MeV. 111

6.13 The spectrum achieved by gating around the scattered ^{12}C particles in the ^{12}C(^{12}C,^{12}C)^{12}C scattering experiment at $\theta^{\text{lab}} = 15^{\circ}$ and $E_{\text{beam}} =$ 80 MeV. 112
6.14 The spectrum achieved by gating around the scattered ^{12}C particles in the ^{13}C(^{12}C,^{12}C)^{13}C scattering experiment at $\theta^{\text{lab}} = 15^{\circ}$ and $E_{\text{beam}} =$ 80 MeV. 112
6.15 The spectrum achieved by gating around the ^{6}He particles in the ^{24}Mg(^{12}C,^{6}He)^{30}S reaction at $\theta^{\text{lab}} = 5^{\circ}$ and $E_{\text{beam}} = 70$ MeV. 114
6.16 Particle simulations for the Cathode vs. Scintillator plot at $E_{\text{beam}} = 90$ MeV in the ^{12}C(^{24}Mg,^{6}He)^{30}S reaction. 115
6.17 Cathode vs. Scintillator 2D histograms for the ^{13}C(^{24}Mg,^{6}He)^{31}S and ^{12}C(^{24}Mg,^{6}He)^{30}S reactions at $E_{\text{beam}} = 90$ MeV. 116
6.18 The momentum spectrum of ^{6}He particles corresponding to the states of ^{30}S in the ^{12}C(^{24}Mg,^{6}He)^{30}S reaction at $\theta^{\text{lab}} = 5^{\circ}$ and $E_{\text{beam}} = 90$ MeV. 117

A.1 The percentage differences between the standard yields and the yields obtained from using the updated ^{23}Na(p,γ)^{24}Mg reaction rate. 123
A.2 The percentage differences between the standard yields and the yields obtained from using the updated ^{23}Na(p,α)^{20}Ne reaction rate. 123
A.3 The percentage differences between the standard yields and the yields obtained from using the updated ^{26g}Al(p,γ)^{27}Si reaction rate for the $Z = 0.02$ model. 124

List of Tables

3.1 Resonances below 1 MeV which contribute to the ^{23}Na(p,α)^{20}Ne reaction rate, and their properties. 45
3.2 The lower, recommended and upper limits of the ^{23}Na(p,α)^{20}Ne reaction rate (in units of cm^3/mole/s) as a function of temperature. . . . 46
3.3 The REACLIB fit parameters for the ^{23}Na(p,α)^{20}Ne reaction rate. . . 49
3.4 ^{24}Mg resonances below 1 MeV which contribute to the ^{23}Na(p,γ)^{24}Mg reaction rate, and their properties. 51
3.5 The lower, recommended and upper limits of the ^{23}Na(p,γ)^{24}Mg reaction rate (in units of cm^3/mole/s) as a function of temperature. . . . 53
3.6 The REACLIB fit parameters for the ^{23}Na(p,γ)^{24}Mg reaction rate. . . 54
3.7 ^{27}Si resonances below 1 MeV, which contribute to the ^{26g}Al(p,γ)^{27}Si reaction rate, and their properties. 58
3.8 The lower, recommended and upper limits of the ^{26g}Al(p,γ)^{27}Si reaction rate as a function of temperature. The rates are in units of cm^3/mole/s. 59
3.9 The REACLIB fit parameters for the ^{26g}Al(p,γ)^{27}Si reaction rate. . . 60

4.1 A comparison of the excitation energies (in MeV) and J^π values of ^{26}Si states from different tabulated values in the literature. 79
4.2 Continuation of Table 4.1 80

6.1 The experimental setup for the ^{20}Ne(^{12}C,^{6}He)^{26}Si test run in January 2007. 100
6.2 The experimental setup for the ^{12}C(^{12}C,^{6}He)^{18}Ne run in July 2007. . 106
6.3 The peaks used for calibration of the focal plane and their properties. 107
6.4 The experimental setup for the ^{12}C(^{24}Mg,^{6}He)^{30}S experiment. 114

A.1 The standard set of stellar yields for the $6\,M_{\odot}$, $Z = 0.02$ model. . . . 125
A.2 The stellar yields computed using the updated $^{26g}Al(p,\gamma)^{27}Si$ reaction rate for the $6\,M_{\odot}$, $Z = 0.02$ model. 126
A.3 The stellar yields computed using the updated $^{23}Na(p,\alpha)^{20}Ne$ reaction rate for the $6\,M_{\odot}$, $Z = 0.02$ model. 127
A.4 The stellar yields computed using the updated $^{23}Na(p,\gamma)^{24}Mg$ reaction rate for the $6\,M_{\odot}$, $Z = 0.02$ model. 128
A.5 The standard set of stellar yields for the $6\,M_{\odot}$, $Z = 0.004$ model. . . 129
A.6 The stellar yields computed using the updated $^{26g}Al(p,\gamma)^{27}Si$ reaction rate for the $6\,M_{\odot}$, $Z = 0.004$ model. 130
A.7 The stellar yields computed using the updated $^{23}Na(p,\alpha)^{20}Ne$ reaction rate for the $6\,M_{\odot}$, $Z = 0.004$ model. 131
A.8 The stellar yields computed using the updated $^{23}Na(p,\gamma)^{24}Mg$ reaction rate for the $6\,M_{\odot}$, $Z = 0.004$ model. 132
A.9 The standard set of stellar yields for the $6\,M_{\odot}$, $Z = 0.008$ model. . . 133
A.10 The stellar yields computed using the updated $^{26g}Al(p,\gamma)^{27}Si$ reaction rate for the $6\,M_{\odot}$, $Z = 0.008$ model. 134
A.11 The stellar yields computed using the updated $^{23}Na(p,\alpha)^{20}Ne$ reaction rate for the $6\,M_{\odot}$, $Z = 0.008$ model. 135
A.12 The stellar yields computed using the updated $^{23}Na(p,\gamma)^{24}Mg$ reaction rate for the $6\,M_{\odot}$, $Z = 0.008$ model. 136

Part I

Nuclear Reaction Rates and Their Impact on the AGB Yields

Chapter 1

Evolution of Low- to Intermediate-Mass Asymptotic Giant Branch Stars

Introduction

Throughout history, the grandeur and mystery of the night sky have stimulated the curiosity and provoked the astonishment of mankind. Our desire to explore the secrets of the universe over both small and large scales, over the course of the years, has motivated us to attempt to discover the keys to understanding the structure of the universe. Through the interplay of exploration, discovery, and analysis, we now have a number of diverse sciences, such as nuclear physics and astrophysics.

These two fields of research may look unrelated at first glance; however, the universe on its large scale, governed by the astrophysical laws (radiation laws, e.g. Wien's displacement law; and gravity laws), is still partly constructed from infinitesimal building blocks of chemical elements, which are in turn governed by the laws of nuclear physics. The connection between astrophysics and sub-atomic physics was initiated in the 1930's when the basic nuclear reactions were worked out by Hans Bethe and C. F. Weizsäcker [1, 2]; and when nuclear physics explained the origin of energy in stellar systems, and began to address the question of the chemical element synthesis. In an effort to understand the origin of the chemical elements, inquiries

during the last fifty years have revealed that the chemical elements from which our bodies are constructed originated in distant space [3]. Detailed understanding of this cosmic heritage requires knowledge of astrophysics and nuclear physics merged into a single field called nuclear astrophysics [3].

Nuclear astrophysics provides us with a more integral picture of the universe from which we can begin to understand and explain a number of important astrophysical phenomena: stellar evolution; stellar energy generation; the formation of white dwarfs, neutron stars and black holes; the chemical evolution of galaxies; X-ray bursts; stellar element synthesis and the observed solar and galactic isotopic abundances. [3].

Knowledge of elemental abundances in stars and galaxies has progressed during the course of time and it continues to furnish the basic stimulus for the investigation of element synthesis in stellar environments. The theory of the synthesis of elements was introduced in 1957 by Burbidge, Burbidge, Fowler and Hoyle [4]. They fastidiously analyzed the observed abundances of stars and gathered all the information into a coherent theory, referred to as the theory of *nucleosynthesis*. This theory explains the creation of heavier elements in stars by various nuclear processes and nuclear reactions.

Various nuclear reactions in stars take place during different stages of stellar evolution. As the stars evolve, the initial hydrogen and helium, which were produced in the Big Bang, are fused into heavier nuclei, some of which are in turn ejected into the interstellar medium during the final stages of the stellar lifetime. These ejecta change the local abundances and thus contribute to the formation of new stellar generations with different abundances. The main feature of the nucleosynthesis theory is that all elements from carbon to uranium are produced entirely within stars [3].

Like any other theory, this theory has to be tested by matching its predictions to the results of experiments and observations. The observational data in this case will be the abundances of nuclear species as a function of time coming from composition of earth, meteorites, stellar spectra and so on. In recent years there has been significant progress in stellar nucleosynthesis modeling, which has helped us understand the mixing and nuclear burning processes inside stars. With this approach we are able to follow the entire stellar evolution from H-burning in the cores

of stars to extreme fates of stellar death such as supernovae. However, these models crucially depend on the rates of nuclear reactions in the nucleosynthesis network. The role of an experimental nuclear astrophysicist is to study the nuclear reactions in the laboratory, so as to provide the nuclear structure information with which the nuclear reaction rates can be calculated more accurately [5].

In recent years, scientists have become interested in asymptotic giant branch (AGB) nucleosynthesis as well as explosive nucleosynthesis, which focus on the nuclear processes in the AGB stars; and in novae and X-ray bursts, respectively [6, 7, 8, 9]. In this thesis we follow the asymptotic giant branch nucleosynthesis in part I, where we aim to study the impact of the recently improved reaction rates on the AGB yields; and the explosive nova nucleosynthesis in part II, where, we aim to determine the feasibility of pursuing the studies of the structure of ^{26}Si and ^{30}S via the (^{12}C,^{6}He) reaction mechanism.

1.1 Evolution of Low- to Intermediate-Mass Asymptotic Giant Branch Stars

There are many reviews of the Asymptotic Giant Branch phase of evolution during the past decades starting with Iben and Renzini (1983) [10] followed by Wood (1993), Lattanzio *et al.* (1996), Herwig *et al.* (1997), Blöcker (2001), Lattanzio (2002), Karakas (2003), Habing & Olofsson (2004), Herwig (2005) and others.[1]

Stars with masses in the range of $0.8\,M_{\odot} < M < 8\,M_{\odot}$ pass through the asymptotic giant branch (AGB) phase of evolution towards the end of their lifetime [14, 18]. The Asymptotic Giant Branch phase of evolution follows the horizontal branch phase, and shows similarities with the red giant branch (RGB) phase; however, these two phases have to be discerned from one another.

Looking at the evolutionary track in the HR diagram in Fig. 1.1, the star burns hydrogen in its core during the main sequence. The core contracts once hydrogen is exhausted in the core, and the rise in temperature causes hydrogen to start burning in a shell around the core. At this point, the outer layers expand and the

[1]References [11, 12, 13, 14, 8, 15, 16, 17], respectively.

star ascends through the red giant branch. eventually, there is enough heat produced to burn helium in the core. The helium burning phase in the core starts at Zero Age Horizontal Branch (ZAHB), and will be continued during the horizontal branch (HB). ZAHB stars have a helium burning convective core surrounded by an unburned helium shell. This shell itself is surrounded by a hydrogen burning shell inside a hydrogen rich envelope. The hydrogen burning shell produces helium which is accumulated on the helium core, causing it to increase its mass and luminosity. At this point the star gradually evolves toward the Asymptotic Giant Branch. The star will begin this phase of evolution following some movements back and forth from ZAHB on the evolutionary track, approaching the Hayashi line when the central helium in its core is exhausted. When the star reaches the Hayashi track[2], the evolutionary track bends upward along a path referred to as the Asymptotic Giant Branch. At this time, the star has exhausted helium in its core and has developed a C-O core instead. Following the exhaustion of helium in the core, the star has lost its source of nuclear energy generation, and thus it contracts. Along with the contraction of the helium-exhausted core, neutrinos are produced and carry away the energy generated by the gravitational contraction. As a consequence, the central density increases, and in contrast the temperature decreases temporarily. At this stage, electron degeneracy pressure plays an important role in the total pressure in the carbon-oxygen core. The degenerate C-O core is surrounded by two thin unburned helium and hydrogen burning shells, respectively, and the star is now a so-called AGB star which is evolving along the early AGB phase of evolution.

1.2 Early AGB Phase of Evolution

In the early AGB phase of evolution, the CO core (resulting from He-burning in the core in the previous phase) becomes degenerate, and thus the temperature rises up to a point where helium starts burning in a thin shell around the CO core. The ignition of the helium shell releases a huge amount of energy, which goes into

[2]The Hayashi track is an approximately vertical path of stellar evolution on the Hertzsprung-Russell diagram along which a protostar evolves towards the main sequence. While on the Hayashi track, as the star contracts, its luminosity decreases but its surface temperature remains almost the same. The track is named after Chushiro Hayashi.

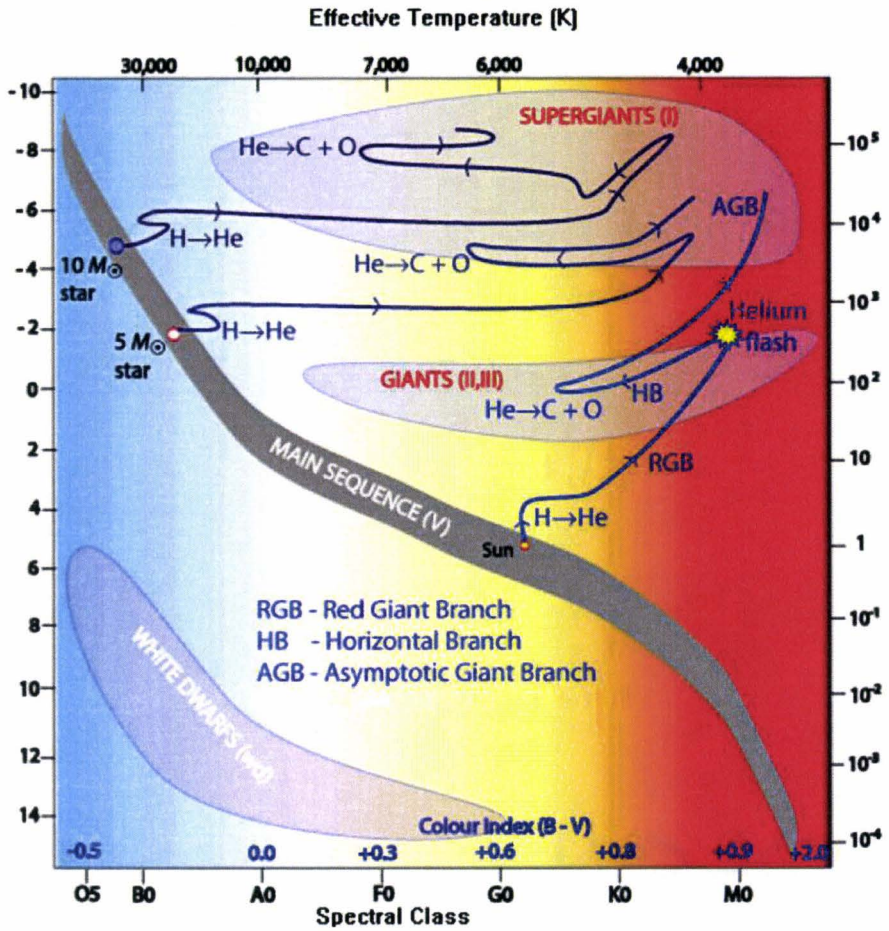

Figure 1.1: Post-main sequence evolutionary tracks for 1, 5 and 10 solar mass stars. On this diagram: the main sequence is where the stars are burning hydrogen in their cores; RGB is the red giant branch, where the stars finish the hydrogen fuel in their core and as a result they contract. The rise in temperature heats up the hydrogen shell, and thus hydrogen starts burning in the shell. This new radiation pressure causes the outer layers to expand and the stars ascend through the red giant branch; HB is the horizontal branch, where the stars are burning helium in their cores and hydrogen in a shell around the core. The numbers on the right axis of the diagram show the luminosity compared to the sun and the numbers on the left axis are the absolute magnitudes (M_v). The diagram is adopted from Ref. [19].

the expansion of the layers. Thus, the base of the H-rich envelope is expanded and cooled. So the hydrogen burning process in its shell is temporarily switched off.

Expansion causes the temperature to drop. In contrast, nuclear burning

causes the temperature to rise. Such phenomena create a temperature gradient, which causes convection zones to be developed. In intermediate-mass stars, $M > 3.5\,M_{\odot}$ [20], as well as in more massive stars, the surface convection zone penetrates the helium layer in the so-called second dredge-up phase[3] and results in significant changes in the composition of the envelope: the helium abundance is increased; carbon and oxygen are partly replaced by ^{14}N; the abundance of ^{15}N is decreased; and finally the ^{12}C/^{13}C ratio is partly changed [15]. For lower mass stars, H-burning in the shell remains quite efficient, and prevents the outer convection from penetrating deeper into the star. Thus the second dredge-up does not occur in low mass stars. Introducing H-rich material to the region which was previously H-poor, the second dredge-up process decreases the mass of the H-exhausted core.

Depending on the initial chemical composition, in those stars with masses on the order of $\sim 8\,M_{\odot}$ at solar metallicities, the electron degeneracy pressure in the C-O core is not high enough to prevent carbon from ignition. Thus, in such stars carbon starts burning in the core. On the other hand, stars with initial masses less than $8\,M_{\odot}$ enter the thermally pulsing AGB phase.

1.3 The Thermally Pulsing Phase

During the early AGB phase, for stars with masses in the range of $3.5\,M_{\odot}$ to $8\,M_{\odot}$, the surface convection zone penetrates deeply into the helium layer from the top, thus mixing fresh hydrogen with the material in the helium layer; at the same time the helium burning shell also approaches the convection zone from below. Penetration of the convection zone into the helium layer, finally supplies enough heat to reignite hydrogen in its shell. The situation at this point is that there exist two burning shells, one of which is burning helium and the other is burning hydrogen. The shells are separated by a small mass interval, called the inter-shell region as can be seen in Fig. 1.2. This situation gives rise to an instability[4] resulting in a series of

[3]The first dredge-up takes place at the base of the Red Giant Branch where the hydrogen is exhausted in the core, leaving behind a contracting helium core. The convective envelope moves inward and mixes the outer layers with internal matter. This results in the dilution of helium in regions just above the deepest layer reached by the outer convection zone. This process also changes the surface abundances. For more information, see Ref. [21].

[4]The instability is due to the fact that the helium burning shell around the C-O core is very thin and the rate of the energy generation in the helium burning shell is highly sensitive to tem-

thermal pulses in which the helium burning shell increases in luminosity, thus causing the expansion of the inter-shell region and cooling the hydrogen burning shell until it switches off again. The whole picture from where the hydrogen is reignited to production of the helium flashes is called the thermal pulsing AGB (TP-AGB) phase of the evolution. The AGB star then continues through a quiescent He-burning phase. The dominant energy source for the thermal pulse is the triple-α reaction. The helium burning occurs in the He-shell where the electrons are not degenerate, and as a result the energy produced by the burning process raises the pressure and thus initiates the expansion. Eventually the helium burning shell is expanded and cooled to the point where the helium shell-burning process switches off. At this stage the inter-shell region contracts. The temperature rises up again and the hydrogen is reignited inside the H-shell. This phase is called the interpulse phase: the pulse has faded away and hydrogen has reignited in its shell. Quiescent H-burning continues until the mass of its ashes which are helium-rich is sufficient to initiate another pulse. At this time, H-burning in the shell is disturbed and switched off by the second pulse. This cycle is repeated many times. Fig. 1.3 shows a schematic evolution of an AGB star through two thermal pulse cycles.

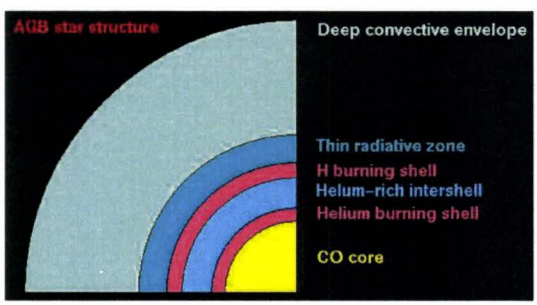

Figure 1.2: Schematic diagram of the structure of an AGB star.

It is worth discussing in some detail the convective phenomena and the important nucleosynthesis events that can occur during the AGB phase of evolution. These topics will be discussed in the next section.

perature [21].

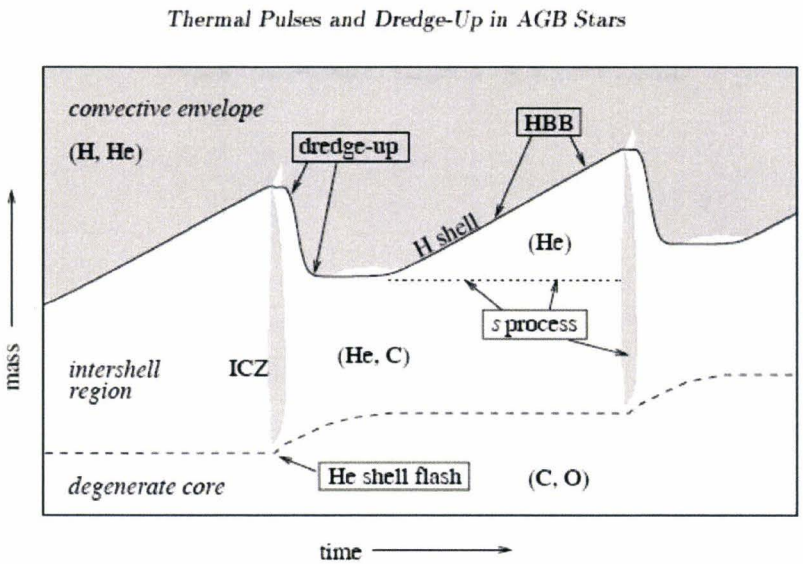

Figure 1.3: Schematic evolution of an AGB star with mass $M > 3.5\,M_{\odot}$ through two thermal pulse cycles. The shaded areas are the convective regions, the solid line is the H-exhausted core mass, and the He exhausted core mass is shown as a dashed line. The main composition of each region is shown in parenthesis. The time axis is highly non-linear, with the shell flash and dredge-up phases expanded compared to the interpulse phase [22]. ICZ stands for the inter-shell convection zone. The diagram is taken from Ref. [22].

1.4 Nucleosynthesis in AGB Stars

The main nucleosynthesis in low- and intermediate-mass stars takes place in the Asymptotic Giant Branch phase of evolution. As discussed previously, AGB stars are fueled by two nuclear burning shells, namely, the hydrogen and helium burning shells. These two shells are the sites for different nucleosynthesis processes. The nuclear reaction networks in the AGB stars mostly involve H- and He-burning reactions, e.g. proton capture reactions through the CNO, NeNa and MgAl cycles at the site of the H-burning shell and α-capture reactions at the site of the He-burning shell [15]. Two of the latter reactions (α-capture reactions of ^{13}C and ^{22}Ne) release a significant number of neutrons and consequently neutron capture reactions also occur [15]. Different reaction networks occur at different locations in the star. We

will discuss AGB nucleosynthesis in more detail in the following two subsections.

1.4.1 Nucleosynthesis during the TP-AGB Phase of Evolution; He-Burning Shell and s-Process Nucleosynthesis

From the seminal work of Iben [23], it is known that the rather short TP-AGB phase of evolution (compared to the overall stellar lifetime) is crucial because it is in this stage of evolution where stars experience substantial nucleosynthesis which leads to the production of very heavy elements (heavier than iron). During the thermal pulses or He-flashes, the temperature is high enough, on the order of 10^8 K, for a very rich nucleosynthesis to begin. The products of the He-burning process are dredged up from the He-burning shell to the inter-shell region by convection, resulting ultimately in the production of trans-iron elements via s-process.

During the thermal pulse, the nuclear energy in the He-burning shell is produced via the dominant triple-α reaction ($^4\mathrm{He} + {}^4\mathrm{He} + {}^4\mathrm{He} \rightarrow {}^{12}\mathrm{C}$) as well as the less dominant $^{12}\mathrm{C}(\alpha,\gamma)^{16}\mathrm{O}$ reaction [15]. Consequently, the He-burning shell primarily produces ^{12}C. ^{16}O is also produced to a lower extent, and thus the abundance of ^{16}O is roughly an order of magnitude smaller than the final ^{12}C abundance [10].

The energy released by these reactions results in the creation of a convection zone, which follows the He-flash and extends from the helium burning shell to the inter-shell region moving upward to the hydrogen shell. This convection zone dredges-up the ashes of He-burning, mainly ^{12}C, from the base of the helium shell to the inter-shell region, and reaches up far enough to ingest protons from the hydrogen shell [15]. Therefore, it mixes protons with the He-burning ashes.

One consequence of this partial mixing in the inter-shell region is the production of ^{13}C via the $^{12}\mathrm{C}(\mathrm{p},\gamma)^{13}\mathrm{N}(\beta^+,\nu)^{13}\mathrm{C}$ reaction sequence, and ^{13}C in turn produces ^{16}O and neutrons via the $^{13}\mathrm{C}(\alpha,\mathrm{n})^{16}\mathrm{O}$ reaction. This latter reaction is one of the neutron production sources, which provides an environment of sufficiently low neutron flux for further neutron capture reactions to occur, which eventually results in the production of heavy elements in the AGB stars.

For example, some of the neutrons produced by the $^{13}\mathrm{C}(\alpha,\mathrm{n})^{16}\mathrm{O}$ reaction can be captured by ^{14}N, which in turn is produced in the H-burning shell during the

preceding interpulse period. This results in the production of ^{14}C and protons. ^{14}C can capture an α-particle, resulting in the production of ^{18}O. The protons from the ^{14}N(n,p)^{14}C reaction can be captured by ^{18}O and the sequence ^{18}O(p,α)^{15}N(α,γ)^{19}F produces a substantial amount of ^{19}F. ^{19}F is in turn destroyed during the He-flash through the ^{19}F(α,p)^{22}Ne and the ^{19}F(n,γ)^{20}F reactions [24]. The destruction of ^{19}F via α-capture and neutron-capture reactions is due to the availability of α-particles as well as neutrons (mostly from the ^{13}C(α,n)^{16}O reaction) in the site of the He-shell burning during the thermal pulse [15]. Note that ^{19}F will not be destroyed via the ^{19}F(p,α) or the ^{19}F(p,γ) reactions, since these reactions would require protons to occur which are not available in the He-shell, and thus these two reactions are not likely to take place in the site of the He-shell burning during the thermal pulse period [15].

Another important consequence of thermal pulses is the production of ^{22}Ne. Substantial amount of ^{22}Ne is created during the thermal pulse via the ^{14}N(α,γ)^{18}F(β^+,ν)^{18}O(α,γ)^{22}Ne reaction sequence. Note that the ^{14}N in this series of reactions comes from the CNO cycle of the previous interpulse phase. We will discuss the production of ^{14}N in more detail in the next subsection. ^{22}Ne in turn is another source of neutrons (via the ^{22}Ne(α,n) reaction[5]) for the production of the s-process elements.

Depending on the dominant neutron source, a different s-element pattern is expected. This is due to the fact that the ^{13}C neutron source, activated at lower temperatures $\sim 0.8 \times 10^8$ K, can offer higher neutron exposures owing to the larger abundance of ^{12}C in the inter-shell region [15]. There is also a wealth of other He-burning products such as ^{20}Ne and ^{24}Mg, which are produced by subsequent (α,γ) reactions [15]. The latter nuclei will become important later on during the interpulse phase. They are seed nuclei for chains of reactions responsible for production of energy after the pulse dies down through the NeNa and MgAl cycles at the base of H-burning shell to be discussed next.

[5]This reaction has been recently investigated by Karakas *et al.* [25].

1.4.2 Nucleosynthesis during the Interpulse Phase of Evolution in AGB Stars; H-Burning Shell and the Hot Bottom Burning

After the thermal pulse dies down, the interpulse phase begins, and hydrogen begins to burn in its shell. At this time, the dredged-up material in the inter-shell region is driven to the H-burning shell by convection, and thus the access to fuel is enhanced. This triggers diverse nuclear burning in a process called hot bottom burning at the base of the H-burning shell. Fig. 1.4 shows a schematic structure of an AGB star, and the flash driven inter-shell convective zone which is responsible for starting the HBB. HBB produces interesting pattern of nucleosynthesis through some very interesting chains of reactions to be discussed in the following subsections, resulting in the production of lighter elements. Finally, these elements as well as s-process elements in turn are introduced to the surface by a rather complicated recurrent convective mixing process called the third dredge-up, which is discussed in the next subsection.

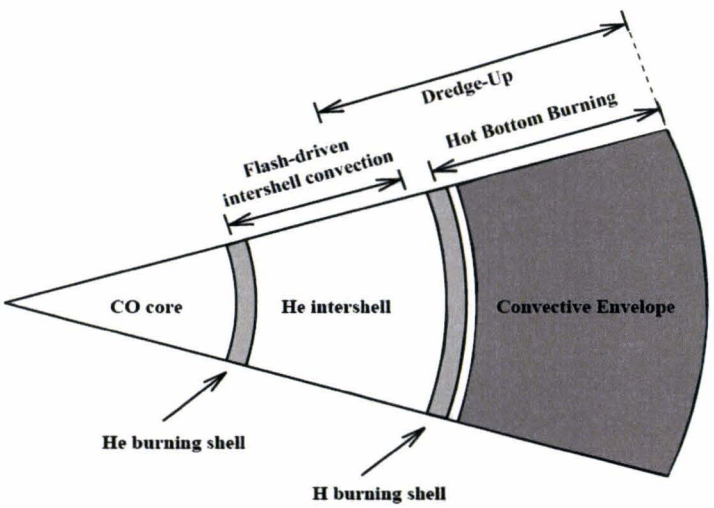

Figure 1.4: Schematic structure of an AGB star. The material from the inter-shell region are transported to the base of the H-burning shell by the convective envelope inside the inter-shell region, which is produced by the He-flash. Then, the third dredge-up process carries this material to the surface of the star. The figure is taken from Ref. [26].

During the interpulse period, only in the intermediate-mass AGB stars with masses in the range of $3.5\,M_{\odot}$ to $5-8\,M_{\odot}$ when the temperature at the base of the convective envelope reaches 20×10^{6} K, can the convective envelope penetrate the H-burning shell, thereby activating the so-called hot bottom burning (hereafter, HBB process) [15]. As a result, these stars depending on their initial metallicity[6], undergo a nucleosynthesis which involves a series of proton capture reactions at the base of the H-burning shell.

The nucleosynthesis signatures of HBB includes Li production via the so-called beryllium-transport mechanism[7]; enhancement in helium and nitrogen abundances; depletion of ^{18}O; a low ^{12}C/^{13}C ratio; a low C/O ratio; efficient destruction of ^{19}F via the ^{19}F(p,α) and ^{19}F(p,γ) reactions; and enhancement of the abundances of ^{23}Na, ^{25}Mg, ^{26}Mg and ^{26}Al nuclei. HBB burns hydrogen and the main nuclear reactions are: the CNO cycle when the temperature at the base of H-burning shell reaches 35 million K; the NeNa cycle when the temperature reaches 50 million K and the MgAl cycle when even higher temperatures on the order of 70 million K are reached.

A number of pieces of observational evidence support the idea that HBB certainly happens in intermediate-mass to more massive AGB stars: almost all of the ^{12}C and ^{16}O in the envelope is converted to ^{14}N via the CNO cycle in the HBB process (that is why HBB is responsible for preventing the production of carbon stars); the existence of M-stars with bolometric masses ($-6 > M_{bol} > -7$) with enhancement of surface lithium abundance [27]; the overabundance of nitrogen and helium in some AGB stars [28]; and finally, high isotopic ratios of ^{26}Al/^{27}Al found in some meteoritic oxide grains of pre-solar origin [29].

We now proceed to discuss the HBB reaction cycles and nucleosynthesis in more detail.

[6]For a given initial mass, the core mass of an AGB star is larger for lower metallicities. Thus the lower initial-mass boundary for HBB decreases with lower metallicity [17].

[7] Lithium is produced via the ^{3}He(α,γ)^{7}Be(β^{-},ν)^{7}Li reaction sequence at a convective base temperature greater than 40 million K.

1.4.2.1 The CNO Cycle

During the HBB process in AGB stars, when the temperature at the base of the convective envelope exceeds 35 million K, a network of reactions involving carbon and oxygen, whose abundances are high and whose coulomb barriers are small, is activated. This sequence of reactions is called the CNO cycle and is primarily responsible for the production of ^{13}C and ^{14}N in the inter-shell region during the interpulse period, when the HBB is active. Most of the ^{13}C is then destroyed via the ^{13}C(α,n)^{16}O reaction; however, the ^{14}N abundance remains high enough to feed other sequences of reactions, which finally leads to the production of the s-process elements in the next thermal pulse, as was discussed before. The high abundance of ^{14}N is due to the slow hydrogen burning rate of this nucleus.

The reaction sequence of the CNO cycle, historically known as the CN cycle, is as follows [30]:

^{12}C(p,γ)^{13}N(β^+,ν)^{13}C(p,γ)^{14}N(p,γ)^{15}O(β^+,ν)^{15}N(p,α)^{12}C

By summing the particles before and after the cycle, we obtain [30]:

$^{12}\mathrm{C} + 4\mathrm{H} \rightarrow {}^{12}\mathrm{C} + {}^{4}\mathrm{He} + 2\beta^+ + 2\nu$

As the temperature goes up, the (p,α) reaction at the end of the CNO reaction sequence, which provides the catalytic material for further CNO cycling, competes with a (p,γ) reaction on the same seed nucleus. This latter reaction prevents the CNO cycle from operating by turning the catalytic material into heavier nuclei that cannot be used in the CNO cycle. Thus, depending on which one of these two reactions has a higher reaction rate, the catalytic material can be preserved or be lost. As an example, at higher temperatures ($T_9 \geq 0.02$, where T_9 is the temperature in units of GK), ^{18}O is destroyed via the ^{18}O(p,γ)^{19}F reaction[8]. ^{19}F in turn can be destroyed via the ^{19}F(p,γ)^{20}Ne reaction, which operates more efficiently at higher temperatures; and thus, the CNO catalytic material will be lost through this reaction. The CNO cycle then ceases to be an energy source in hydrogen burning; however, the ^{20}Ne which will be produced substantially, will form the basis for further hydrogen burning through the NeNa cycle to be discussed in the next subsection.

[8] ^{18}O is produced via the ^{17}O(p,γ)^{18}F(β^+,ν)^{18}O reaction. ^{17}O is in turn produced via the same scenario: If oxygen is initially abundant, the reaction sequence ^{15}N(p,γ)^{16}O(p,γ)^{17}F(β^+,ν)^{17}O will occur; and thus, ^{17}O is created.

1.4.2.2 The NeNa Cycle

The temperature at the base of convective envelope during HBB can be hot enough, depending on the initial mass and metallicity of the star, for activation of two other cycles, called the NeNa and MgAl cycles. Through these cycles, the operation of the HBB in the intermediate-mass AGB stars is associated with the creation of sodium, heavy magnesium isotopes and radioactive ^{23}Mg, which are important observational markers.

Fig. 1.5 displays the sequence of reactions in the NeNa cycle. It starts from the nucleus ^{20}Ne when the temperature at the base of convective envelope reaches about 50 million K. The reaction sequence of the cycle is as follows [3]:

^{20}Ne(p,γ)^{21}Na(β^+,ν)^{21}Ne

^{21}Ne(p,γ)^{22}Na(β^+,ν)^{22}Ne

^{22}Ne(p,γ)^{23}Na(p,α)^{20}Ne

This cycle is responsible for the synthesis of elements between ^{20}Ne and ^{23}Na, and it plays an important role in understanding the origin of ^{22}Ne in meteoritic samples. But more importantly, the NeNa cycle is responsible for the enhancement of ^{23}Na abundances in AGB stars due to the fact that proton captures on ^{21}Ne and ^{22}Ne are very fast. ^{21}Ne is destroyed considerably during HBB. On the other hand the ^{22}Ne abundance is significantly increased during the thermal pulse via the ^{18}O(α,γ) reaction, and then during the inter-pulse phase ^{22}Ne will be destroyed by HBB. In contrast to proton captures on ^{21}Ne and ^{22}Ne, the proton capture on ^{23}Na is relatively slow [31, 32]. Thus the abundance of ^{23}Na increases until the complete consumption of ^{21}Ne and ^{22}Ne. ^{23}Na is efficiently produced in the HBB process if sufficient amount of carbon is dredged-up by the thermal pulse-driven convection zone. ^{12}C is eventually converted to ^{14}N, which can in turn be replaced by ^{22}Ne. Eventually, ^{23}Na itself will be destroyed by the competing ^{23}Na(p,α) and ^{23}Na(p,γ) reactions. Currently available rate information reveals that the stellar rate for the ^{23}Na(p,α) reaction is large enough to guarantee the operation of the NeNa cycle; however, at higher temperatures, ^{23}Na is mostly destroyed via the ^{23}Na(p,γ) reaction which will bypass the NeNa cycle into another important cycle, called the MgAl cycle.

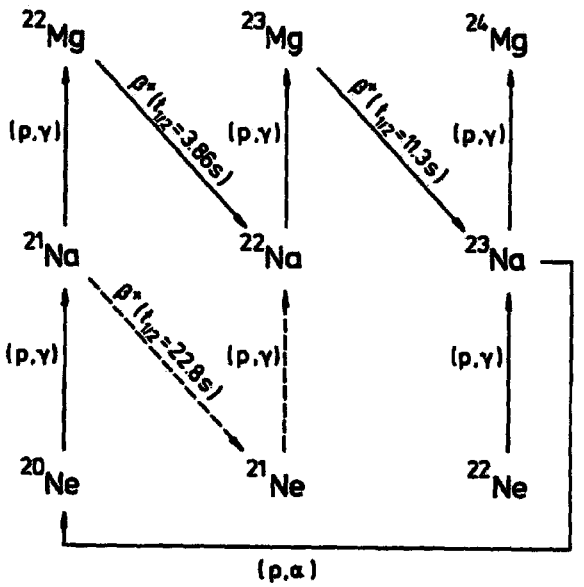

Figure 1.5: Schematic diagram of the NeNa cycle [33].

1.4.2.3 The MgAl Cycle

With the discovery of an excess of ^{26}Mg in certain inclusions of the Allende meteorites [34], it was suggested that radioactive ^{26}Al ($T_{1/2} = 7.2 \times 10^5$ y) could be concentrated in the material of the solar cloud at the time of its condensation. This brought the MgAl cycle to attention since this cycle was thought to be one of the sources of production of ^{26}Al. The MgAl cycle is responsible for synthesis of elements between ^{24}Mg and ^{27}Al via hydrogen burning. Fig. 1.6 shows the reactions of the NeNa and MgAl cycles.

The magnesium and aluminium isotopes are produced in three different sites inside AGB stars: the H-burning shell via the MgAl cycle; the He-burning shell via α-capture on ^{20}Ne, and finally at the base of convective envelope during HBB process, again via the MgAl chain. During the interpulse phase, when HBB is active if the temperature of the base of the convective envelope reaches $\sim$ 70 million K [35], the MgAl cycle is activated, and results in large depletion of ^{22}Ne and ^{24}Mg, followed by significant enhancements of ^{25}Mg, ^{26}Mg and ^{26}Al [36]. There is also a moderate enhancement of ^{23}Na as well as ^{27}Al [36].

In the temperature range $T_9 \leq 0.4$, the half-lives of all the radioactive species in this cycle are short compared with the timescales of nuclear burning, except for the ground state of ^{26}Al. As a result, ^{26}Al which is produced via the ^{25}Mg(p,γ) reaction, is destroyed via the ^{26}Al(p,γ)^{27}Si reaction. Therefore this reaction is crucial in determining the amount of ^{26}Al present when the MgAl cycle is ceased. As will be discussed in the third chapter, this reaction has been recently investigated and its rate has been improved; thus this improved reaction rate can be used in order to obtain more accurate yield for ^{26}Al synthesized in AGB stars.

Eventually, the catalytic material required for the operation of these cycles will be lost, and that is how HBB and its associated burning processes will be halted [15]. The termination of HBB is discussed in the next section. Finally, the last two sections present the termination of the AGB phase of evolution and its impact on the chemical evolution of galaxies.

In order to understand the operation of the NeNa and MgAl cycles, we need to know the reaction rates for the competing ^{23}Na(p,α) and ^{23}Na(p,γ) reactions as well as that of ^{26}Al(p,γ) reaction, which take place in the NeNa and MgAl cycles. These three reaction rates used to carry large uncertainties and thus needed to be investigated in more detail (see chapter 3).

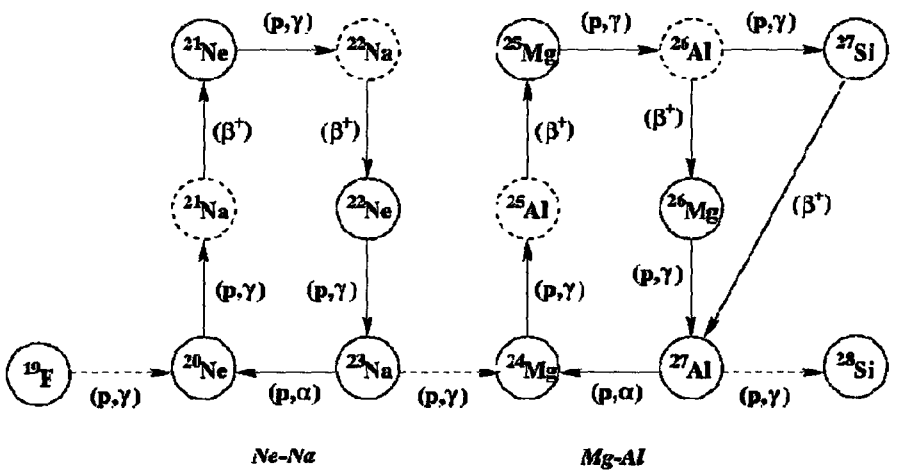

Figure 1.6: Schematic diagram of the NeNa and MgAl cycles. Unstable isotopes are indicated by dashed circles. The diagram is adopted from Ref. [36].

1.4.3 The Third Dredge-up Process

Towards the end of the AGB phase of evolution, the AGB stars lose significant amount of their mass through strong stellar winds. This causes the reduction of the mass of the envelope above the hydrogen burning shell. Moreover, hydrogen burning at the base of the envelope through the HBB process also reduces the mass of the H-shell, simply because hydrogen is burning in subsequent reactions, and thus it will be depleted. Finally, since the fuel necessary for performance of the HBB will be lost over time, HBB is finally terminated just before the star leaves the AGB phase of evolution.

Following each interpulse phase, in intermediate-mass AGB stars, a very important convective mixing occurs, called the third dredge-up process. The convective zone penetrates the deepest layers of the star and brings up all the freshly synthesized elements produced in HBB to the stellar surface, along with the s-process elements produced during the pulse in the inter-shell region. Thus the third dredge-up process alters the surface abundances of the AGB stars, especially those of H, He, C, N, O, Ne, Mg and Al isotopes.

It has been long known that the third dredge-up process increases the C/O ratio. This is because the third dredge-up process dredges up carbon from the interior of the star to its surface. Following their work in 2002 [37], Marigo *et al.* have investigated the relation between HBB and its competing third dredge-up process [20]. They have concluded that the efficiency of HBB may be reduced if during the early stage of TP-AGB evolution, a massive AGB star experiences efficient carbon dredge-up so as to become a carbon star. This is owing to the fact that the carbon-rich chemical composition is associated with increased molecular opacities which affect the temperature of layers above the core, thus creating a cooling effect both at the base of convective envelope, where HBB is activated, and at the atmosphere. The decrease in the temperature at the base of the convective envelope results in a reduction of the nuclear reaction rates of HBB, and the lower effective temperature at the atmosphere results in larger mass-loss rates. Hence the operation of HBB is either turned off very early, or is prevented altogether.

1.5 Termination of the AGB Evolutionary Phase

Depending on the initial mass and the mass loss rate, AGB stars will have very different fates. The low mass AGB stars ($M_{star} \leq 2.5\,M_{\odot}$) will finally become carbon stars due to several third-dredge-up episodes which cause a significant amount of carbon to appear on the stellar surface. The C/O ratio will increase because the temperature at the base of the convective envelope in such stars will not be raised too high, so the HBB either will not be experienced or will be turned off quickly. As a result, HBB cannot burn sufficient carbon to prevent such stars from becoming carbon stars.

For the intermediate-mass AGB stars (2.5 to $8\,M_{\odot}$ [21]), this phase of evolution is finally terminated by severe mass loss over the last 2 - 3 helium-shell-flash cycles through strong stellar winds. The mass loss is dominated by the helium flashes or the thermal pulses. If the thermal pulse phase is sufficiently long, the flash forces the mass outflow from the stellar surface to be accelerated [38] and the star will expand rapidly until the gas becomes cool enough that heavy elements can condense into dust grains. The dust grains in turn absorb and scatter stellar radiation and transfer this energy to the gas by collisions, so that the flow velocity may exceed the escape velocity [39]. Mass-loss grows with time until the so-called super-wind regime sets in, which quickly turns the star into a planetary nebula by stripping away all the envelope and leaving a bare core. This core will evolve towards the regime of the central star of planetary nebulae and will finally be transformed into a C-O white dwarf. This is due to the fact that such stars are not able to burn carbon in their cores, and as a result the white dwarf mainly consists of carbon and oxygen.

More massive AGB stars will go through significant shell-burning processes and mass loss episodes, depending on their initial mass:

(i) If the initial mass of the star is in the range of $8\,M_{\odot} < M_{star} \leq 11\,M_{\odot}$, its C-O core will eventually become hot enough for fusion of carbon nuclei, and thus carbon starts burning in the core. This will occur, because the AGB star is massive enough such that the mass loss processes are unable to reduce the mass of the core below $\sim 1.4\,M_{\odot}$, in which case the star is able to ignite carbon in its core. The energy released by carbon burning raises the temperature in the

convective envelope, and a thermal runaway takes place. Then the star moves off the AGB phase and enters the Super Asymptotic Giant Branch (SAGB).[9] After the exhaustion of carbon in the core, the second dredge-up occurs and a period of the interpulse phase begins, where hydrogen is burning inside a thin shell. The interpulse phase will be followed by subsequent thermal pulses and the third dredge-up processes. Eventually, the severe stellar winds will remove the hydrogen-rich surface layers and the star becomes the central white dwarf of the planetary nebula [40]. However, in this case, in contrast to the intermediate-mass stars, the white dwarf will consist of oxygen and neon, known as an O-Ne white dwarf.

(ii) If the star's initial mass is more than 11 $M_{\odot}$, it undergoes successive burning stages in its core by using the ashes of the previous core burning stage, as fuel [40]. So the subsequent core-burning reactions can potentially lead to the formation of iron-peak elements. When the mass of the core exceeds $\sim 1.4\, M_{\odot}$, the electron degeneracy will not be able to balance gravity, and thus the core collapses in free fall [40]. Eventually, the star will explode in a type II, Ib or Ic supernova.

If the AGB stars are in binary systems, the companion star can increase the mass loss rate of the AGB star, which leads to faster transition from the AGB phase to the planetary nebula and final white dwarf configuration.

1.6 The Roles of the AGB Stars

Asymptotic Giant Branch stars are known as the sources of the majority of presolar grains [41, 42]. For instance, one of the most important indicators that AGB stars could be the origin of presolar SiC grains is that they show the signature of s-process nucleosynthesis. A detailed analysis of the composition of Sr, Zr, Mo and Ba in single SiC grains and in AGB models was presented by Lugaro *et al.* [43].

Nucleosynthesis in AGB stars plays an important role in the chemical evolution of galaxies: repeated dredge-up events enrich the stellar surface with freshly

[9] Very luminous stars with highly evolved cores are called super-AGB stars and their core is made of a mixture of oxygen-neon.

synthesized nuclei which are then lost to the interstellar medium through strong stellar winds. Thus, AGB stars are one of the cosmic sources for the recycling of matter. AGB stars may also be potential polluters for globular cluster stars [44].

Chapter 2

Stellar Thermonuclear Reaction Rates

In the previous chapter, the AGB nucleosynthesis and energy generating reactions which determine the final evolutionary paths for such stars were discussed. This chapter presents a summary of the theoretical formalism from which one calculates the rates at which different reactions take place in various stellar environments as a function of temperature.

2.1 Overview

Nuclear reactions play a key role in the production of energy and nucleosynthesis in stars. In such reactions, lighter nuclei fuse to form heavier ones. The kinetic energy available to particles in stellar interiors is that of their thermal motions, and hence the reactions which are induced by this motion are called thermonuclear reactions [45]. However, the average kinetic energy due to thermal motion is smaller than the Coulomb barrier, and thus classically there would not be any reactions at all. The only possibility for occurrence of the thermonuclear reactions in stars comes from a quantum mechanical effect found by G. Gamow [46]: there is a small but finite probability of penetrating ("tunneling") through the Coulomb barrier, even if the particle's energy is less than that of the barrier. One year after the discovery of the quantum tunneling effect, R. Atkinson and F. Houtermans [47] in 1929 discovered that thermonuclear reactions can provide the energy source for stars. Ten years after their fundamental work, it was found that two different types of thermonuclear

reactions are of importance in the stellar interior: the proton-proton chain, which was proposed by C. Critchfield and H. Bethe [48], and the C-N cycle, which was proposed independently by H. Bethe [49] and C. von Weizsäcker [50].

However, as was discussed in Chapter one, the proton-proton chain and the CN cycle are not the only chains of reactions providing energy for the stars. For stellar temperatures as low as 10^7 K, only the lightest nuclei have a chance to react. For reactions of heavier particles, the temperature, and thus the kinetic energy of the particles, have to be considerably larger to provide a comparable penetration probability.

It is not easy to measure the probability that a given nuclear reaction will take place. In the laboratory, the cross-section is a measure of the probability per pair of particles for a reaction to occur [30]. However, inside the stars, there are several factors, e.g., the temperature and velocity distribution of nuclei, which are crucial for the reactions to take place. Thus, to obtain the stellar thermonuclear reaction rate, one integrates the nuclear reaction cross-section over the thermal velocity distribution of the nuclei.

Well-separated stages of different nuclear burning reactions that liberate energy, will necessarily change the chemical composition of stars. It is the slow change of chemical composition that causes the structure of the star to evolve. If, as for the case of AGB stars, the star loses part of its mass into space, the ejected debris will alter the chemical composition of the interstellar medium as well, and thus the star contributes to the galactic chemical evolution.

As was mentioned in the previous chapter, all heavy elements are synthesized in the stellar interior by various thermonuclear reactions that occur in different stages of stellar evolution. For these reasons it is worthwhile to discuss the subject of thermonuclear reaction rates in more detail. This chapter presents the stellar nuclear reaction rate theory and describes the determination of stellar reaction rates. The next chapter will present some important nuclear reactions for AGB nucleosynthesis, the evaluation of their rates and the effect of improved reaction rates on the yields, which help us understand their observed abundances.

2.2 Stellar Thermonuclear Reaction Rate Mechanism

The Q-value of a nuclear reaction is the energy released by that reaction or the energy required for the reaction to proceed. From this energy and the number of reactions per unit volume per second, we can calculate the energy liberated per unit volume per second as a simple product. The calculation of energy generation rates involves the use of the concept of the cross-section for a reaction.

Consider a reaction $a + X \rightarrow Y + b$. In this reaction, we assume that nuclei of type "X" are the stationary targets and nuclei of type "a" are the projectiles. The cross section for this reaction is defined as [30]:

$$\sigma(\text{cm}^2) = \frac{\text{number of reactions/nucleus X/unit time}}{\text{number of incident particles/cm}^2\text{/unit time}} \tag{2.1}$$

This definition of the cross section is symmetric in the two types of particles, since the relative velocity is viewed as the same from either particle. Nuclear cross sections are in general energy-dependent, and as a result are also velocity-dependent. Thus $\sigma = \sigma(v)$, where v represents the relative velocity between the projectile and the target nucleus.

Now consider the nuclei of types "X" and "a" present in the stellar gas with N_X particles of type "X" and N_a particles of type "a" per cubic centimeter, and velocities v_X and v_a with relative velocities v.

Since the cross section only depends on the relative velocity v, one can assume either particles of type "X" or "a" as the projectiles with velocity v. If we assume any one to be projectiles, then the other must be considered at rest. Consequently, the projectiles see N target nuclei per cubic centimeter, and each target nucleus has an area $\sigma(v)$ [3]. Thus, the effective area F per cubic centimeter that the projectiles see equals the cross section for a single target nucleus multiplied by the number of target nuclei per cubic centimeter. So, assuming that the nuclei of type X are target nuclei, $F = \sigma(v)N_X$ [3]. Since each projectile sees this area F, the total number of nuclear reactions occurring depends on the flux of incident particles, which is defined as the product of the number density of projectiles and their velocities, $N_a v$ [3]. Finally,

the reaction rate is given by the effective area of the target nuclei, F, times the flux of projectile nuclei [3]:

$$r = N_X N_a v\sigma(v) \tag{2.2}$$

In this equation, r is in units of reactions per cubic centimeter per second. If both types of nuclei are moving, as is the case inside the stellar gas, then v is still the magnitude of their relative velocity.

In the stellar gas, there exists a mixture of nuclei in thermodynamic equilibrium, and the velocities of the reacting particles vary over a wide range of values. Thus, each of the reacting particles has a velocity distribution spectrum $\phi_i(v_i)$. Moreover, there exists some spectrum of relative velocities, $\phi(v)$, between both reacting particles. These individual velocity spectra and the relative velocity spectrum are defined such that [3]:

$$\int_0^\infty \phi(v_i)\, d^3v_i = 1 \tag{2.3}$$

$$\int_0^\infty \phi(v)\, dv = 1 \tag{2.4}$$

Since $\phi(v)dv$ represents the probability that the relative velocity v has a value between v and $v + dv$, the product $v\sigma(v)$ in equation (2.2) has to be convoluted together with the velocity distribution $\phi(v)$ to arrive at a value for $v\sigma(v)$ averaged over the velocity distribution, $< \sigma v >$, defined as:

$$< \sigma v > = \int_0^\infty \phi(v) v\sigma(v)\, dv \tag{2.5}$$

The quantity $< \sigma v >$ is referred to as the reaction rate per particle pair. The total reaction rate will then be:

$$r = N_X N_a < \sigma v > \tag{2.6}$$

If the reacting particles are identical, the number product $N_X N_a$ must be divided by 2, for otherwise we would count each pair twice. So, we can introduce a Kronecker symbol δ_{aX} in the equation (2.6), which leads to [30]:

$$r = N_X N_a < \sigma v > (1 + \delta_{aX})^{-1} \tag{2.7}$$

Computing thermonuclear reaction rates is not an easy task. The problem mainly reduces to the evaluation of $< \sigma v >$ and, in order to calculate this quantity, we need to know the form of the function $\phi(v)$.

Inside the star, the stellar gas is almost always non-degenerate (note that exceptions are white dwarfs and neutron stars for which the stellar gas is degenerate). Furthermore, the gas is in thermodynamic equilibrium and the nuclei are moving non-relativistically. Thus, the velocity distribution $\phi_i(v_i)$ is given by a 3-dimensional Maxwell-Boltzmann velocity distribution as follows:

$$\phi_i(v_i)\, dv_{ix}\, dv_{iy}\, dv_{iz} = (\frac{m_i}{2\pi kT})^{\frac{3}{2}} \exp(-\frac{m_i v_i^2}{2kT})\, dv_{ix}\, dv_{iy}\, dv_{iz} \tag{2.8}$$

where m_i, k and T are the mass of nuclei of type i, Boltzmann's constant and temperature, respectively. The probability that a particle of species i has a velocity v_i is just the product $N_i \phi_i(v_i)$, where N_i is particle density of type i.

It is clear that the reaction rate involves an integral over [30]

$$N_i \phi_i(v_i)\, dv_{ix}\, dv_{iy}\, dv_{iz}\, N_j \phi_j(v_j)\, dv_{jx}\, dv_{jy}\, dv_{jz}$$

$$= N_i N_j \frac{(m_i m_j)^{\frac{3}{2}}}{(2\pi kT)^3} \exp(-\frac{m_i v_i^2 + m_j v_j^2}{2kT})\, d^3v_i d^3v_j \tag{2.9}$$

which physically represents the product of the probability that particle i has velocity v_i in the volume d^3v_i times the probability that particle j has the velocity v_j in the volume d^3v_j. Since the reaction rate is expressed in terms of the velocity v, we need to know the form of $\phi(v)$. The following calculation shows that the distribution of relative velocities between two species of particles is also Maxwellian.

As stated in Ref. [51], for two non-relativistic particles of masses m_i and m_j with velocities v_i and v_j, the center of mass velocity V is defined as:

$$V = \frac{m_i v_i + m_j v_j}{m_i + m_j} \tag{2.10}$$

So the individual velocities become

$$v_i = V + \frac{m_j}{m_i + m_j} v \tag{2.11}$$

$$v_j = V - \frac{m_i}{m_i + m_j} v \tag{2.12}$$

where $v = v_i - v_j$ is the relative velocity of particle i with respect to particle j. The total initial kinetic energy before the collision is:

$$T_i = \frac{1}{2} m_i v_i^2 + \frac{1}{2} m_j v_j^2 \tag{2.13}$$

By plugging equations (2.11) and (2.12) into equation (2.13), the initial kinetic energy becomes

$$T_i = \frac{1}{2} M V^2 + \frac{1}{2} \mu v^2 \tag{2.14}$$

where $M = m_i + m_j$ is the total mass and $\mu = \frac{m_i m_j}{M}$ is the reduced mass. The first expression on the right hand side of equation (2.14) can be thought of as the kinetic energy of a mass M moving with the velocity V of the center of mass, and thus it is the kinetic energy of the center of mass; the second expression is the kinetic energy of a single particle with mass μ moving with the relative velocity v, and thus it is the kinetic energy of the two particles in the center of mass system.

Returning to equation (2.9), we can rewrite the kinetic energy term $(1/2 \times (m_i v_i^2 + m_j v_j^2))$ as the sum of the kinetic energy of the center of mass and the kinetic energy of the relative motion in the center of mass system. Thus, the probability product is reduced to

$$N_i \phi_i(v_i)\, d^3 v_i N_j \phi_j(v_j)\, d^3 v_j = N_i N_j \frac{(m_i m_j)^{\frac{3}{2}}}{(2\pi k T)^3} \exp\left[-\frac{(m_i + m_j) V^2}{2kT} - \frac{\mu v^2}{2kT}\right] d^3 v_i d^3 v_j \tag{2.15}$$

In order to transform the integral over $d^3 v_i d^3 v_j$ to an integral over $d^3 V d^3 v$, we use the theory of jacobian determinants [30] which states that given two functions $f(x, y)$ and $g(x, y)$ of two variables x and y, an integral over $dxdy$ may be replaced

by an integral over $dfdg$ using the following ratio:

$$\frac{dA_{f,g}}{dA_{x,y}} = \text{magnitude of} \begin{vmatrix} \frac{\partial f}{\partial x} & \frac{\partial f}{\partial y} \\ \frac{\partial g}{\partial x} & \frac{\partial g}{\partial y} \end{vmatrix} \tag{2.16}$$

So in our case, the ratio is

$$\begin{vmatrix} \frac{\partial v_{ix}}{\partial V_x} & \frac{\partial v_{ix}}{\partial v_x} \\ \frac{\partial v_{jx}}{\partial V_x} & \frac{\partial v_{jx}}{\partial v_x} \end{vmatrix} = \begin{vmatrix} 1 & \frac{m_j}{m_i+m_j} \\ 1 & \frac{-m_i}{m_i+m_j} \end{vmatrix} = -1 \tag{2.17}$$

Using this ratio, the probability product in equation (2.15) can be rewritten as [30]

$$\{(\frac{m_i+m_j}{2\pi kT})^{\frac{3}{2}} \exp(-\frac{(m_i+m_j)V^2}{2kT})\, d^3V\}[(\frac{\mu}{2\pi kT})^{\frac{3}{2}} \exp(\frac{-\mu v^2}{2kT})\, d^3v] \tag{2.18}$$

The expression in the curly brackets represents the Maxwell-Boltzmann velocity distribution of the velocity of the center of mass; the expression in the square brackets represents the Maxwell-Boltzmann distribution of the relative velocity (the distribution considered initially). Since these distributions are normalized, the integral over d^3V yields unity, and thus the reaction rate integral is reduced to [30]

$$r = N_i N_j \int v\sigma(v)(\frac{\mu}{2\pi kT})^{\frac{3}{2}} \exp(-\frac{\mu v^2}{2kT})\, d^3v \tag{2.19}$$

Considering the fact that d^3v may be replaced by $4\pi v^2 dv$ (assuming spherical symmetry), the above expression can be reduced further to

$$r = 4\pi N_i N_j \int v^3\sigma(v)(\frac{\mu}{2\pi kT})^{\frac{3}{2}} \exp(-\frac{\mu v^2}{2kT})\, dv \tag{2.20}$$

Moreover, from equations (2.5) and (2.6), the integral form of the total reaction rate can be written as

$$r = N_X N_a \int_0^\infty \phi(v) v\sigma(v)\, dv \tag{2.21}$$

Now by comparing equations (2.20) and (2.21), we conclude that

$$\phi(v)\,dv = 4\pi(\frac{\mu}{2\pi kT})^{\frac{3}{2}} \exp(-\frac{\mu v^2}{2kT})v^2\,dv \tag{2.22}$$

which confirms that the distribution of the relative velocities of two species of nuclei in the stellar gas is of the form of a Maxwell-Boltzmann distribution as illustrated in Fig. 2.1.

From equations (2.6) and (2.22), it is obvious that [3]

$$< \sigma v >= 4\pi(\frac{\mu}{2\pi kT})^{\frac{3}{2}} \int_0^\infty v^3\sigma(v) \exp(-\frac{\mu v^2}{2kT})\,dv \tag{2.23}$$

Using the center of mass kinetic energy $E = \frac{1}{2}\mu v^2$, we finally obtain [3]

$$< \sigma v >= (\frac{8}{\pi\mu})^{\frac{1}{2}} \frac{1}{(kT)^{\frac{3}{2}}} \int_0^\infty \sigma(E)E \exp(-\frac{E}{kT})\,dE \tag{2.24}$$

Thus, the stellar thermonuclear reaction rate is given by [3]

$$r = N_X N_a (1+\delta_{aX})^{-1}(\frac{8}{\pi\mu})^{\frac{1}{2}} \frac{1}{(kT)^{\frac{3}{2}}} \int_0^\infty \sigma(E)E \exp(-\frac{E}{kT})\,dE \tag{2.25}$$

To calculate the stellar thermonuclear reaction rate, it is crucial to know the

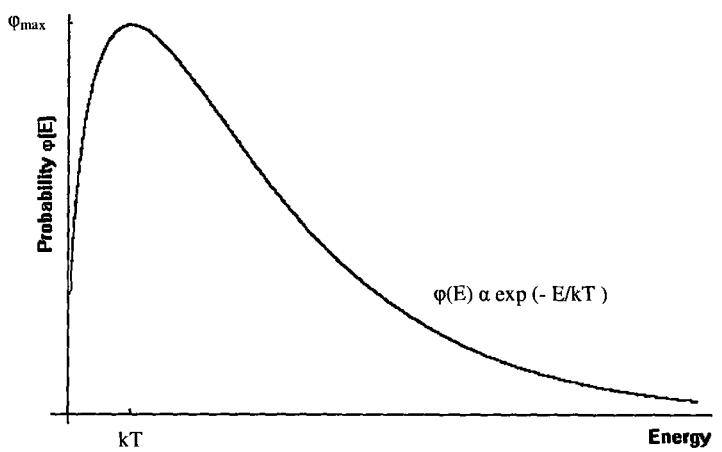

Figure 2.1: The Maxwell-Boltzmann energy distribution of a gas characterized by a temperature T. The distribution shows a maximum at $E = kT$. The diagram is adopted from Ref. [3]

functional form of the cross section, $\sigma(v)$, or equivalently $\sigma(E)$. In the next section this will be described in detail.

2.3 Non-Resonant Reaction Rates

Due to the quantum tunneling probability, even particles with sub-barrier energies[1] can react. The quantum tunneling probability, $P_l(E)$ is given by the WKB approximation as [30, 52]:

$$P_l(E) \propto exp(-\frac{2\sqrt{2\mu}}{\hbar}\int_{R_0}^{R_c}\sqrt{V_l(r)-E}\,dr) \tag{2.26}$$

where R_c is the classical turning point at $E = V$; R_0 is the contact distance between the nuclear surfaces and is equal to $R_0 = 1.4(A_1^{\frac{1}{3}} + A_2^{\frac{1}{3}})$, where A_i is the respective atomic mass number of each nucleus; and $V_l(r)$ is the sum of the centrifugal and the Coulomb potentials defined as follows:

$$V_l(r) = \frac{l(l+1)\hbar^2}{2\mu r^2} + \frac{Z_1 Z_2 e^2}{r} \tag{2.27}$$

where l is the quantum number of relative angular momentum between two particles; r is the spatial separation; μ is the reduced mass; and Z_i is the elementary nuclear charge of each nucleus in integer units. Clearly, the tunneling probability is highest for $l = 0$, and with this simplification the argument of the exponential of expression (2.26) can be expressed as [51, 53]:

$$\frac{4Z_1Z_2e^2}{\hbar v}[\frac{\pi}{2} - (\frac{E}{E_c})^{\frac{1}{2}}(1-\frac{E}{E_c})^{\frac{1}{2}} - \arcsin(\frac{E}{E_c})^{\frac{1}{2}}] \tag{2.28}$$

where E_c is the effective height of the Coulomb barrier.

At low energies, where $E \ll E_c$, the probability that the incoming particles will penetrate the barrier can be approximated by [3]:

$$P = \exp(-2\pi\eta) \tag{2.29}$$

[1]Energies less than the Coulomb barrier.

The quantity η is the so-called Sommerfeld parameter and is equal to

$$\eta = \frac{Z_a Z_X e^2}{\hbar v} \tag{2.30}$$

Thus

$$2\pi\eta = 31.29 Z_a Z_X (\frac{\mu}{E})^{\frac{1}{2}} \tag{2.31}$$

where E is the center of mass energy in units of keV, μ is the reduced mass in units of amu and Z is the atomic number [3]. Equation (2.31) is referred to as the *Gamow factor* and is an approximation for the tunneling probability.

The tunneling probability, equation (2.29), falls off rapidly for energies below the Coulomb barrier. The cross section is also proportional to $\pi\lambda^2$, which is a representation of the geometrical cross section and where λ represents the de Broglie wavelength, reflecting the wave-like aspect of quantum mechanical processes. It is given by [3]

$$\pi\lambda^2 \propto (\frac{1}{p})^2 \propto \frac{1}{E} \tag{2.32}$$

Primarily because of the exponential behavior of the probability for tunneling, it follows that the cross section, where σ is now expressed as a function of energy E instead of the relative velocity v, also tends to show the same behavior and drops rapidly for energies below the Coulomb barrier. Thus

$$\sigma(E) \propto \exp(-2\pi\eta) \tag{2.33}$$

So

$$\sigma(E) \propto \begin{cases} \frac{1}{E} \\ \exp(-2\pi\eta) \end{cases} \tag{2.34}$$

Finally, we conclude that [3]

$$\sigma(E) = \frac{1}{E} \exp(-2\pi\eta) S(E) \tag{2.35}$$

where the function $S(E)$ is called the astrophysical S-factor. It represents the intrinsically nuclear effects contributing to the probability for a nuclear reaction to take place [3]. For non-resonant reactions, where the interaction energy of the particles

differs from the energy at which a quasi-stationary state is resonated, this function varies very smoothly with energy.

Substituting equation (2.35) into equation (2.24), one obtains [3]

$$< \sigma v >= (\frac{8}{\pi\mu})^{\frac{1}{2}} \frac{1}{(kT)^{\frac{3}{2}}} \int_0^\infty S(E) \exp[-\frac{E}{kT} - \frac{b}{E^{\frac{1}{2}}}] \, dE \tag{2.36}$$

where the quantity b is related to the barrier penetrability and is given by [3]

$$b = (2\pi)^{\frac{1}{2}} \pi e^2 \frac{Z_1 Z_2}{\hbar} = 0.989 Z_a Z_X \mu^{\frac{1}{2}} (\text{MeV})^{\frac{1}{2}} \tag{2.37}$$

The quantity b^2 is equal to the so-called Gamow energy (E_G). We need to determine the cross section at relevant Gamow energy for any reaction.

In equation (2.36), the first exponential term in the integral is a measure of the number of available particles in the high-energy tail of the Maxwell-Boltzmann distribution, and this term is only important at low energies (note that from Fig. 2.1, this distribution approaches zero at high energies) [3]. The second exponential only plays a role at higher energies and is related to the penetration through the Coulomb barrier [3]. The integral in equation (2.36) cannot be performed analytically, and one usually goes back to the saddle-point method or the method of steepest descent [30, 54]. The product of the two terms as shown in Fig. 2.2, gives rise to a peak of the integrand in equation (2.36) at an energy E_0. This peak is referred to as the Gamow peak, and it is the most effective energy region for thermonuclear reactions to occur [3]. If no resonance appears, the astrophysical S-factor is often assumed to be constant over the energy range close to the Gamow peak.

$$S(E) = S(E_0) = \text{constant} \tag{2.38}$$

As can be seen in Fig. 2.2, the peak of the Maxwell-Boltzmann distribution, kT, is much smaller than the Gamow peak, E_0, which is in turn much smaller than the Coulomb barrier. Thus, the cross section at the Gamow energy is on the order of 10^{-12} to 10^{-9} barn (barn = 10^{-28} m^2); hence, it is difficult to measure the cross section directly at the Gamow energy. The usual procedure to measure the cross section is measuring it over as wide a range as possible, and then extrapolate down

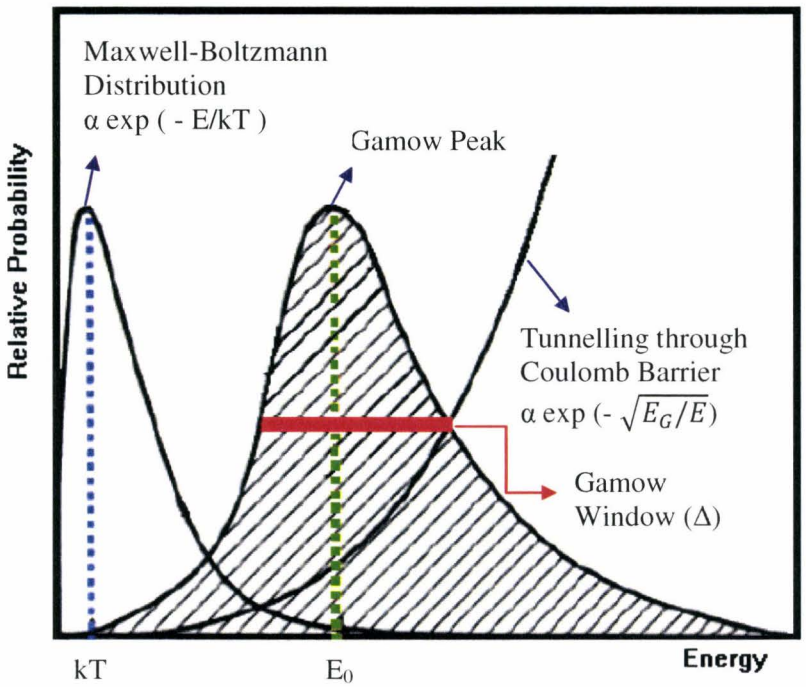

Figure 2.2: The Gamow peak (E_0) (the dashed area, note that the peak is not to scale) is calculated by the convolution of the Maxwell-Boltzmann energy distribution and the tunneling function, and it always occurs at higher energies than the maximum of the Maxwell-Boltzmann energy distribution (kT) The Gamow window is shown by a red band. The figure is adopted from Ref. [3].

to the Gamow energy region around the Gamow peak.

Using the equations (2.36) and (2.38), we have for non-resonant reactions [3]

$$< \sigma v >= (\frac{8}{\pi\mu})^{\frac{1}{2}} \frac{1}{(kT)^{\frac{3}{2}}} S(E_0) \int_0^\infty \exp[-\frac{E}{kT} - \frac{b}{E^{\frac{1}{2}}}] dE \tag{2.39}$$

By finding the energy at which the integrand in equation (2.39) is a maximum, one finds E_0 to be [3]:

$$E_0 = (\frac{bkT}{2})^{\frac{2}{3}} = 1.22((Z_a Z_X)^2 \mu T_6^2)^{\frac{1}{3}} \quad \text{keV} \tag{2.40}$$

Referring to Fig. 2.2, the red band is the $1/e$ width of the peak, which is the effective width Δ, known as the Gamow window. For a given stellar temperature T, nuclear reactions take place in this relative narrow window around the effective

burning energy E_0 [3]. This width is calculated from finding the extremum of the second derivative of the integrand in equation (2.39) and is equal to [3]:

$$\Delta = \frac{4}{\sqrt{3}}(E_0 kT)^{\frac{1}{2}} = 0.749(Z_a^2 Z_X^2 \mu T_6^5)^{\frac{1}{6}} \quad \text{keV} \tag{2.41}$$

$E_0 \pm \Delta/2$ is the energy range where the nuclear reactions will most likely occur, and the nuclear structure information of the compound nuclei[2] formed by reactions at Gamow window energies plays a key role in calculating the stellar reaction rates [3].

An important non-resonant reaction process in nuclear astrophysics is the direct-capture process, for which the S-factor varies very smoothly with energy. In this mechanism, the projectile interacts with the target nucleus and as a consequence is directly captured into a bound state of the compound nucleus, so that the direct capture reaction represents a direct transition from the initial to the final state via interaction with the electromagnetic field. A γ-ray photon is then emitted with the energy of $E_\gamma = E_{c.m.} + Q - E_x$, where $E_{c.m.}$ is the center of mass energy, Q is the energy available for the reaction to happen and E_x is the excitation energy of a state in the compound nucleus from which the γ-ray is emitted. The direct-capture reaction can occur regardless of the energy of the projectile as long as it is non-zero [3].

In addition to non-resonant processes, the energy of the projectile nucleus can be such that it resonates a quasi-stationary state inside the compound nucleus. In this case, the reaction is called a resonant reaction and the calculation of its rate is significantly different from what was presented in this section. The next section is allocated to a discussion of resonant reaction rates.

2.4 Resonant Reaction Rates

In resonant reactions, an excited state with energy E of the compound nucleus is formed first, and then subsequently decays to lower energy states. In contrast to the direct capture mechanism which can occur for all energies of the projectile, the resonant reactions can only happen if the energy of the entrance channel $Q + E_R$

[2]Compound nucleus formation is a reaction mechanism in which two nuclei combine into a single excited nucleus, called the compound nucleus. The compound nucleus lives for a relatively long time and "forgets" how it was formed. It then transforms into lighter nuclei by a decay, or by fission.

matches the energy E_x of the excited state in the compound nucleus [3]. Thus

$$E_R = E_x - Q \tag{2.42}$$

where Q is the threshold energy required for the reaction to happen and E_R is the resonance energy. So, when the energy of the reduced mass system is such that it is equal or close to the energy of a resonance state in the compound system, the cross section of the reaction is significantly enhanced. This sudden increase in the cross section is due to the fact that at energies equal or close to the resonance energy, the amplitude of the wave function for the entrance channel matches that of the quasi-stationary state which is resonated [51]. Reactions occurring under such conditions are called resonant reactions. It should be noted that the Gamow energy and the Gamow window formalism is still applicable for resonant reactions. The cross section for resonant reactions is calculated using the Breit-Wigner formula [3]:

$$\sigma(E) = \pi\lambda^2 \frac{2J+1}{(2J_a+1)(2J_X+1)}(1+\delta_{aX}) \frac{\Gamma_a \Gamma_b}{(E-E_R)^2 + (\frac{\Gamma}{2})^2} \tag{2.43}$$

where $\lambda = \frac{h}{\sqrt{2\mu E}}$ is the center of mass de Broglie wavelength (μ is the reduced mass), J is the angular momentum of the excited state in the compound nucleus, J_a and J_X are the spins of the two reacting particles in the entrance channel, $(1+\delta_{aX})$ is a factor that ensures that identical reacting particles are not counted twice, E is the energy of the projectile, E_R is the resonance energy, and finally Γ, Γ_a and Γ_b are the total resonance width, and the partial widths of the entrance and the exit channels of the reaction, respectively ($\Gamma = \Gamma_a + \Gamma_b$). Equation (2.43) is only valid for isolated resonances for which the separation of the nuclear levels is large compared with their total widths [3].

By plugging equation (2.43) into equation (2.24), we obtain

$$\int_0^\infty \lambda^2 \frac{\Gamma_a \Gamma_b}{(E-E_R)^2 + (\frac{\Gamma}{2})^2} E \exp(-\frac{E}{kT})\, dE$$

$$= \frac{h^2}{2\mu} \int_0^\infty \frac{\Gamma_a \Gamma_b}{(E-E_R)^2 + (\frac{\Gamma}{2})^2} \exp(-\frac{E}{kT})\, dE \tag{2.44}$$

All the widths in equation (2.43) are energy dependent. In the case of narrow

resonances for which the total width Γ of the resonance is much smaller than the resonance energy (typically, if $\frac{\Gamma(E)}{E_R} < 0.1$ [3]), then the Maxwell-Boltzmann exponential factor and the partial widths in equation (2.44) can be evaluated at the resonance energy E_R, and we can then pull them out of the integral. This can be done since in the case of narrow resonances, all of these factors will be smooth functions of energy that vary very slowly over the widths of the resonances, which is narrow; therefore, we can ignore their energy dependence when evaluating the integral. So we are left with a remaining Lorentzian function which can be integrated analytically resulting in

$$< \sigma v >_R = (\frac{2\pi}{\mu kT})^{\frac{3}{2}} \hbar^2 (\omega\gamma)_R \exp(-\frac{E_R}{kT}) \tag{2.45}$$

where the index R stands for "resonance", and

$$\omega = \frac{2J+1}{(2J_a+1)(2J_b+1)} \tag{2.46}$$

and

$$\gamma = \frac{\Gamma_a \Gamma_b}{\Gamma} \tag{2.47}$$

The product $(\omega\gamma)_R$ is the so-called resonance strength and E_R is the resonance energy. These two terms are the nuclear physics dependent terms in the reaction rate.

One important note here is that according to equation (2.45), the stellar resonant reaction rates depend exponentially on the resonance energy. Thus it is very important to measure the resonance energies which lie in the Gamow window as precisely as possible, since the contribution of these resonances to the reaction rate is very significant [51].

If several narrow isolated resonances lie within the Gamow window, then the total resonant reaction rate per particle pair, $< \sigma v >$, will be the sum over the contributions from the resonances [51]:

$$< \sigma v > = (\frac{2\pi}{\mu kT})^{\frac{3}{2}} \hbar^2 \sum_i (\omega\gamma)_i \exp(-\frac{E_{R_i}}{kT}) \tag{2.48}$$

Substituting all the constants into the equation above leads to a simple equa-

tion, which is used to calculate the resonant reaction rate [51]:

$$N_A < \sigma v >_R = 1.54 \times 10^{11} \times (\mu T_9)^{\frac{3}{2}} \sum_i (\omega\gamma)_i \exp(-11.605 \times \frac{E_i}{T_9}) \tag{2.49}$$

where N_A is the Avogadro number, $N_A < \sigma v >_R$ is the resonant reaction rate in units of $\mathrm{cm^3 mole^{-1} s^{-1}}$, μ is the reduced mass, $(\omega\gamma)_i$ is the resonance strength in units of MeV for the state i, and E_i is the corresponding resonance energy in the center of mass system in units of MeV.

In the case of broad resonances for which $\frac{\Gamma}{E_R} \geq 0.1$ [3], the energy dependence of the partial widths must be retained and they cannot be pulled out of the integral [3]. In order to calculate the reaction rate per particle pair, one must then evaluate equation (2.24) taking into account the energy dependence of the cross section.

It is the role of nuclear astrophysicist to measure the resonance energies and the corresponding resonance strengths as accurately as possible. In this chapter the methods of the calculation of stellar reaction rates for different types of reactions, e.g. the non-resonant and resonant reactions, were presented. In the next chapter, we will discuss some important nuclear reactions whose rates are evaluated using the formalism of this chapter.

Chapter 3

The Impact of Reaction Rates on AGB Yields

In this chapter we will explore the AGB stellar yields and will briefly discuss the method from which the yields are calculated as well as the factors that contribute to the uncertainties in the yields. We follow our previous discussion by narrowing down our attention to three important reaction rates occurring in the NeNa and MgAl cycles in the AGB stars, e.g. the ^{23}Na(p,γ)^{24}Mg, ^{23}Na(p,α)^{20}Ne and ^{26}Al(p,γ)^{27}Si reactions, which previously carried large uncertainties in their rates. There has been recent experimental work on these reactions. We have used that information, and have reevaluated these reaction rates, the results of which have been presented in this chapter. Finally, we will study the impact of those improved reaction rates on the AGB stellar yields, and will present the yields in graphical and tabular forms in Appendix A.

3.1 Stellar Yield Calculation

Generally speaking, the stellar yields for intermediate-mass stars depend on a number of things: the time between thermal pulses; the efficiency of the third dredge-up, which determines how polluted the stellar surface will be; and the total number of thermal pulses that a star undergoes during the AGB phase of evolution [55]. These factors in turn depend on the initial mass and metallicity of the star as well as on the

values of the mixing length, dredge-up and mass loss parameters [55]. The stellar yields are also affected if the star is rotating and this fact has been receiving more attention lately [56, 57]. In this section, a method of calculating the appropriate stellar yields to be used in the GCE evolution models is presented.

We use the same definition of the stellar yield as presented in Ref. [58]. The stellar yield of a given chemical element k is the mass fraction of a star with initial mass M_i that is converted into the element k and returned to the ISM during its entire lifetime, $\tau(M_i)$ [58]. According to the definition of the stellar yield, we can write:

$$M_y(k) = \int_0^{\tau} (M_i)[X(k) - X_0(k)]\frac{dM}{dt}dt \tag{3.1}$$

where M_k is the yield of species k in solar masses; $\frac{dM}{dt}$ is the current mass-loss rate; and X_k and $X_0(k)$ refer to the current and initial mass fraction of species k, respectively [58]. If the element is destroyed by nucleosynthesis processes, its yield will be negative. This is due to the fact that in this case, the final surface abundance is lower than the initial. If the element is produced, its yield will be positive. In order to calculate the stellar yields, we have to perform stellar evolution and nucleosynthesis modeling.

Stellar evolution and nucleosynthesis is studied in two steps: calculating the stellar structure from the zero-age main sequence to near the end of the thermally-pulsing AGB; and performing the nucleosynthesis calculations afterwards. The stellar structure is studied by using the stellar evolution codes, e.g. the Monash version of the Mount Stromlo Stellar structure code [59, 60, 61] as was used to calculate the stellar yields presented in this thesis, which is based upon the Henyey-matrix method [62] to solve the equation of stellar structure [15]. This evolution code includes six species (H, ^{3}He, ^{4}He, ^{12}C, ^{14}N and ^{16}O) from which most of the energy is produced [15]. Such nuclei have the greatest impact on the structure of a model. However, in order to understand and explain the observations, e.g. the abundance anomalies observed in globular cluster stars; or the high precision pre-solar grain abundance measurements, e.g. the excess of ^{29}Si and ^{30}Si compared to ^{28}Si measured in silicon carbide grains from the Murchison meteorite [63], more chemical species must be added into stellar evolution models and nuclear networks [15]. These freshly

included species have a negligible effect on the energy production, and thus a negligible impact on the stellar structure [15]. That is why the evolution calculation is done first. The detailed nucleosynthesis calculations is performed afterwards via the "post-processing nucleosynthesis code". This code[1] currently follows 77 species (^{1}H to ^{62}Ni) interacting via 527 reactions. The nucleosynthesis code only calculates the abundance changes due to convective mixing and nuclear reactions [15]. The inputs to the nucleosynthesis code are time, temperature, density as well as the details of convection zones such as the mixing length and velocity as a function of mass [15].

Based on the results of these models, various sets of yields from low to intermediate mass stars have been presented in past [15, 25, 58, 67]. In the next section, we will investigate the factors that cause the stellar yields to carry uncertainties.

3.2 Stellar Yield Uncertainties

There are major uncertainties present in the computation of the stellar models, which are mainly due to [15]:

- Mass loss is one of the most distinct features of AGB stars. It affects their evolution and observable properties. It is caused by stellar pulsation, which sends out atmospheric shock waves that lift the gas above the stellar surface. Thus, a cool and dense layer of dust is produced. The radiation pressure causes these layers to be accelerated and to drag the gas along, driving the gas out to a considerable distance [68]. However, the dust formation scenarios, non-equilibrium dust condensation, and the potential driving forces and other details of how mass loss works on the AGB stars are still not well understood. This lack of knowledge is a major source of uncertainty in the calculation of the TP-AGB phase of evolution. The choice of mass loss law[2] and the mass loss rate to be used in modeling the TP-AGB phase of evolution is the most significant factor, which affects the stellar yields in a number of ways [15]:

  - ◇ The mass loss law determines the TP-AGB lifetime, which is terminated

[1] Details of the stellar evolution code and post-processing nucleosynthesis code used here can be found in Ref. [15, 25, 64, 65, 66].

[2] For details about different mass loss laws, see [15, 69].

when the envelope mass is reduced below about $10^{-2}\,M_{\odot}$ [15]. It also affects the structure at the tip of the AGB and the final H-exhausted core mass. Thus, it affects the evolution and nucleosynthesis of a star and hence leads to different yields.

- ◇ The number of thermal pulses that a model experiences is also influenced by the choice of mass loss rate used in that model. This in turn affects the maximum possible number of the third dredge-up episodes, and thus the total amount of inter-shell material dredged up to the surface lost to the ISM.
- ◇ Not only does mass loss determines the number of thermal pulses, but it can also determine if and when the TDU begins and ends [15]. Studies have suggested that TDU episodes should cease below envelope masses of around $0.5\,M_{\odot}$ [69]. Thus, mass loss has a direct influence on the enrichment of the ISM from thermal pulses and the stellar yields by affecting the efficiency of the TDU episodes.
- ◇ Finally, mass loss affects the occurrence of the HBB. This is due to the fact that mass loss determines the maximum temperature reached at the base of the convective envelope, as well as when that temperature is reached [15]. Thus, it affects the duration and the efficiency of the HBB. This in turn, determines the nucleosynthesis resulting from the HBB, which affects the stellar yields; particularly the yields of ^{23}Na, ^{24}Mg and ^{26}Al, since the abundances of these isotopes depend on the duration of the HBB.

- Uncertainties in the input physics of the stellar models will also affect the stellar yields in a number of ways [15]:
  - ◇ The difference in the treatment of convection and convective boundaries leads to different yields resulting from different models. This is due to the fact that convection affects the depth of TDU episodes; the temperature at the base of the convective envelope during thermal pulses (thus, the strength of the HBB, which is activated afterwards); and the stellar structure [25].

◇ Lack of information about the important resonances that contribute to the reaction rates at the temperature regime of low to intermediate mass stars cause the nuclear reaction rates to be highly uncertain in such temperatures [15]. The uncertainties in nuclear reaction rates lead to an uncertainty in the input of the nucleosynthesis codes, thus affecting the stellar yields.

Nuclear reactions have a profound influence on the structure and the evolution of the entire star. Thus, in what follows we will take a closer look at the nuclear reaction rates and their impact on the stellar yields.

3.3 Nuclear Reaction Rates

In order to perform the post-processing nucleosynthesis computations on the previously computed stellar structure models, it is an ongoing requirement to include the most recent reaction rates. When the nucleosynthesis code was originally written[3], all the included rates were from Caughlan and Fowler [71] (hereafter CF88). Since then, when appropriate more recent rates have replaced the CF88 rates. For generality and flexibility the nucleosynthesis code demands that all rates are converted to the following so-called REACLIB format:[4]

$$\log(\text{rate}) = a_1 + a_2 T_9^{-1} + a_3 T_9^{-\frac{1}{3}} + a_4 T_9^{\frac{1}{3}} + a_5 T_9 + a_6 T_9^{\frac{5}{3}} + a_7 \ln(T_9) \qquad (3.2)$$

where T_9 is the temperature in units of GK, and the a_i's are the fit parameters.

To run the post-processing nucleosynthesis code, we must use updates for some proton, alpha and neutron capture reaction rates to latest experimental results.

[3]It was originally developed to study Thorne-Zytkow objects by Cannon in 1993 [70].

[4]REACLIB [72] is a nuclear reaction rate library for astrophysics, which contains fits to experimental rates as well as theoretical rates to a 7-parameter format. Usually, fits are only valid in a specific temperature region. In REACLIB, this region is T_9 = 0.01 - 10. Nevertheless, it is extremely important that the fits behave well also outside this range. They must not diverge and must not show unphysical oscillation patterns. REACLIB includes approximately 8000 reactions, mostly from Hauser-Feshbach calculations, but including some rates derived from experimental measurements. In contrast to earlier rate libraries, REACLIB uses the same format to characterize each reaction rate as a function of temperature, and only the parameters are different for each reaction. This makes REACLIB well suited for rapid calculations, and it is becoming a standard library used by numerous research groups around the world.

Discussion here will be limited only to those reactions particularly concerned with the NeNa and MgAl chains, e.g. the ^{23}Na(p,α)^{20}Ne and ^{26}Al(p,γ)^{27}Si reactions, as well as the interaction between these two cycles via the ^{23}Na(p,γ)^{24}Mg reaction. This is because these rates have been improved with recent experiments, and thus we want to investigate the impact of such improved reaction rates on the AGB yields, particularly those of Ne, Na, Mg and Al isotopes. From a nuclear physics perspective, the yields of these isotopes are largely affected by the uncertainty ranges in those reactions we are interested in.

Recent studies [35] have revealed that the yield of ^{23}Na suffers from large uncertainties, up to two orders of magnitudes. While the upper range uncertainties are only due to the large uncertainty of the ^{22}Ne(p,γ)^{23}Na reaction rate, the lower uncertainties are determined by the effect of uncertainties in the ^{23}Na(p,α)^{20}Ne as well as the ^{23}Na(p,γ)^{24}Mg reaction rates [35]. It is also obvious that the yield of ^{24}Mg is also affected by the uncertainty in the ^{23}Na(p,γ)^{24}Mg reaction. It should be noted that the ^{23}Na(p,γ)^{24}Mg reaction is a bypass reaction from the NeNa chain to the MgAl chain, so this reaction rate determines the efficiency of the operation of these two cycles during the HBB in the intermediate mass AGB stars.

3.3.1 The ^{23}Na(p,α)^{20}Ne Reaction Rate

In 2004 at TUNL[5], Hale *et al.* [73] used the ^{23}Na(^{3}He,d)^{24}Mg reaction to populate states in the vicinity of the ^{23}Na + p threshold (11.6929 MeV [73]), and have extracted the spectroscopic factors[6] for resonances that contribute to both the ^{23}Na(p,γ)^{24}Mg and ^{23}Na(p,α)^{20}Ne reaction rates. Thus, they have calculated the proton widths for those states, from which they have calculated the resonance strengths for resonances that contribute to both the ^{23}Na(p,γ)^{24}Mg and ^{23}Na(p,α)^{20}Ne reaction rates. Furthermore, they have observed a low energy resonance at $E_{c.m.}$ = 138 keV, which makes a significant contribution to both rates at low energies. In addition, they have estimated a small contribution of a possible resonance at $E_{c.m.}$ = 37 keV to the ^{23}Na(p,α)^{20}Ne reaction rate [73].

[5]Triangle Universities Nuclear Laboratory

[6]Spectroscopic factor contains the nuclear structure information, and is a number between zero and one defined by: $(d\sigma/d\Omega)_{measured} = S\ (d\sigma/d\Omega)_{calculated}$ (S = 1 for a pure shell model) [74].

In this section, we present the calculation of the ^{23}Na(p,α)^{20}Ne reaction rate, which is mostly based upon the experimental information from Ref. [73] unless stated otherwise. There are a number of resonances with energies below $E_{c.m.} = 1$ MeV which contribute to this reaction rate. These resonances and their corresponding resonance strengths are listed in Table 3.1 along with the references from which they are adopted (note that all the resonance energies are in the center of mass system). The contribution of such resonances to the reaction rate can be calculated using equation (2.49). In addition, there is a contribution of the subthreshold resonances and the low-energy tails of higher-lying[7] resonances, which can be calculated using an analytical expression expressed in Ref. [73] as follows:

$$N_A < \sigma v >_{\text{subthreshold}} = 8.06 \times 10^{10} T_9^{-\frac{2}{3}} exp[-\frac{20.769}{T_9^{1/3}} - (\frac{T_9}{0.20})^2]$$

$$\times[1 - 4.52 T_9 - 256 T_9^2 + 7.36 \times 10^3 T_9^3 - 5.90 T_9^4 + 1.73 \times 10^5 T_9^5] \quad (3.3)$$

where T_9 is the temperature in units of GK.

Thus, the total recommended reaction rate is:

$$N_A < \sigma v >_{\text{tot}} = N_A < \sigma v >_{\text{subthreshold}} + N_A < \sigma v >_{\text{R}} \quad (3.4)$$

where $N_A < \sigma v >_{\text{R}}$ is the contribution of all other resonances to the reaction rate (equation (2.49)). It should be noted that for the calculation of the recommended rate (the average value of the rate), we have only considered the central values of the resonance energies and resonance strengths. For the cases where only the upper limit of the resonance strengths are known, we have followed NACRE's[8] [75] policy, and thus the recommended rate is calculated by multiplying the upper limit of those resonance strengths by 10%. To calculate the upper limit of the rate, we have used the upper limit of resonance strengths and the lower limit of resonance energies. For the lower limit of the rate we have considered the lower limit of resonance strengths and the upper limit of resonance energies.

[7]The resonances with energies more than 1 MeV.

[8]Nuclear Astrophysics Compilation of REactions library, which in recent years has become a standard library used in the stellar model calculations. Since it was published in 1999, it does not contain the latest experimental results.

Table 3.1: Resonances below 1 MeV which contribute to the ^{23}Na(p,α)^{20}Ne reaction rate, and their properties.

Resonance Energy[a]	Resonance Strength[b]	Reference 1[c]	Reference 2[d]
5.3	1.9×10^{-55}	Hale *et al.* (2004)[e]	Hale *et al.* (2004)
36.9	$\leq 3.3 \times 10^{-20}$	Hale *et al.* (2004)	Hale *et al.* (2004)
138.0 $\pm$ 2.9	$\leq 1.5 \times 10^{-8}$	NACRE[f]	Iliadis *et al.*[g](2005)
169.5	(2.3 0.5) $\times 10^{-5}$	Hale *et al.* (2004)	Hale *et al.* (2004)
217.5 $\pm$ 1.9	(5.4 $\pm$ 1.3) $\times 10^{-5}$	NACRE	Hale *et al.* (2004)
240.3 $\pm$ 0.2	≤ 0.1	NACRE	Hale *et al.* (2004)
273.9 $\pm$ 0.4	0.035 $\pm$ 0.004	NACRE	Hale *et al.* (2004)
324.4 $\pm$ 0.5	0.071 $\pm$ 0.002	NACRE	Hale *et al.* (2004)
358.6	(4.1 $\pm$ 1.0) $\times 10^{-3}$	Hale *et al.* (2004)	Hale *et al.* (2004)
426.3 $\pm$ 0.1	(5.7 $\pm$ 1.4) $\times 10^{-3}$	NACRE	Hale *et al.* (2004)
490.6	≤ 0.011	Hale *et al.* (2004)	Hale *et al.* (2004)
566.8 $\pm$ 0.4	38 $\pm$ 3	NACRE	Hale *et al.* (2004)
648.3 $\pm$ 0.4	≤ 0.041	NACRE	Hale *et al.* (2004)
692.6 $\pm$ 0.3	≤ 0.25	NACRE	Hale *et al.* (2004)
707.9 $\pm$ 0.3	≤ 0.12	NACRE	Hale *et al.* (2004)
712.6 $\pm$ 0.3	7.4 $\pm$ 1.3	NACRE	Hale *et al.* (2004)
761.6 $\pm$ 0.5	3.3 $\pm$ 0.5	NACRE	Hale *et al.* (2004)
778.9	1.8 $\pm$ 0.3	Hale *et al.* (2004)	Hale *et al.* (2004)
809.5	0.51 $\pm$ 0.1	Hale *et al.* (2004)	Hale *et al.* (2004)
880.4	63 $\pm$ 26	Hale *et al.* (2004)	Hale *et al.* (2004)
962.2	46 $\pm$ 14	Hale *et al.* (2004)	Hale *et al.* (2004)

[a] in units of keV
[b] in units of eV
[c] The references from which the resonance energies are adopted.
[d] The references from which the resonance strengths are adopted.
[e] Ref. [73]
[f] Ref. [75]
[g] Ref. [76]

The values of recommended, the lower and the upper ^{23}Na(p,α)^{20}Ne reaction rate as a function of temperature are listed in tabular form in Table 3.2, and these rates are shown in Fig. 3.1. Note that all the rates are in the units of cm^3/mole/s.

Fig. 3.2 shows the ratio of the upper and lower limits of the ^{23}Na(p,α)^{20}Ne rate to its recommended rate as a function of temperature, so it is a measure of the uncertainty range in this rate, which is about 20% of that of NACRE at $T_9 = 0.2$ GK.

Table 3.2: The lower, recommended and upper limits of the ^{23}Na(p,α)^{20}Ne reaction rate (in units of cm^3/mole/s) as a function of temperature.

T_9	Lower	Recommended	Upper
0.020	5.45e-22	6.40e-22	1.49e-21
0.030	5.97e-18	6.03e-18	6.62e-18
0.035	1.47e-16	1.47e-16	1.50e-16
0.04	2.05e-15	2.05e-15	2.07e-15
0.045	1.91e-14	1.92e-14	1.94e-14
0.05	1.33e-13	1.34e-13	1.40e-13
0.06	4.36e-12	4.72e-12	5.74e-12
0.07	1.41e-10	1.70e-10	2.24e-10
0.08	3.07e-09	3.89e-09	5.43e-09
0.09	3.72e-08	4.91e-08	8.05e-08
0.1	2.79e-07	3.94e-07	8.45e-07
0.11	1.46e-06	2.29e-06	6.71e-06
0.12	5.94e-06	1.07e-05	4.12e-05
0.13	2.01e-05	4.20e-05	2.00e-04
0.14	6.01e-05	1.44e-04	7.91e-04
0.16	4.20e-04	1.19e-03	7.51e-03
0.18	2.29e-03	6.68e-03	4.32e-02
0.200	9.91e-03	2.75e-02	1.74e-01
0.300	1.11e+00	2.15e+00	1.05e+01
0.350	4.48e+00	7.69e+00	3.28e+01
0.400	1.33e+01	2.07e+01	7.67e+01
0.450	3.33e+01	4.75e+01	1.50e+02
0.500	7.53e+01	1.00e+02	2.65e+02
0.600	3.14e+02	3.78e+02	7.14e+02
0.700	9.98e+02	1.15e+03	1.72e+03
0.800	2.47e+03	2.79e+03	3.69e+03
0.900	5.05e+03	5.67e+03	7.01e+03
1.00	8.93e+03	1.00e+04	1.20e+04

We have converted this reaction rate to the REACLIB format (equation (3.2)). This is done because we want to perform the post-processing nucleosynthesis code to be able to obtain the AGB yields, and as was mentioned before, this code takes the reaction rates in the REACLIB format as an input. The result is given in the following equation:

$$\text{rate} = exp(a_1 + a_2 T_9{}^{-1} + a_3 T_9{}^{-\frac{1}{3}} + a_4 T_9{}^{\frac{1}{3}} + a_5 T_9 + a_6 T_9{}^{\frac{5}{3}} + a_7 \ln(T_9)) +$$

$$exp(a_8 + a_9 T_9{}^{-1} + a_{10} T_9{}^{-\frac{1}{3}} + a_{11} T_9{}^{\frac{1}{3}} + a_{12} T_9 + a_{13} T_9{}^{\frac{5}{3}} + a_{14} \ln(T_9))$$

$$+exp(a_{15} + a_{16} T_9{}^{-1} + a_{17} T_9{}^{-\frac{1}{3}} + a_{18} T_9{}^{\frac{1}{3}} + a_{19} T_9 + a_{20} T_9{}^{\frac{5}{3}} + a_{21} \ln(T_9)) \quad (3.5)$$

where a_1 to a_{21} are the resultant REACLIB parameters and are displayed in Table 3.3. Note that here there are 21 fit parameters, whereas in equation (3.2) there were 7 of them. This is due to the fact that in order to convert the reaction rate to the REACLIB format, one needs to fit the rate first. The fitting procedure must be in a way to produce the best fit with as lowest χ^2 as possible[9]. The reaction rate is a function of temperature. Thus, one may need to divide the whole temperature region to as many smaller regions as possible, and fit the rate in those smaller regions so as to obtain the best fit. Equation (3.2) is a general equation that is achieved by fitting the rate in a temperature region. So, depending on how many temperature regions have been used, the total number of fit parameters are different. We have fitted the ^{23}Na(p,α)^{20}Ne reaction rate to a polynomial function in three different temperature regions. Thus, we have obtained 21 fit parameters. The temperature regions over which we fitted the rates were not fixed and depend on the behavior of the rates.

[9] χ^2 is a statistic that tests the fit between a theoretical and an observed frequency distribution. So, it characterizes the dispersion of the observed frequencies from the expected ones [77].

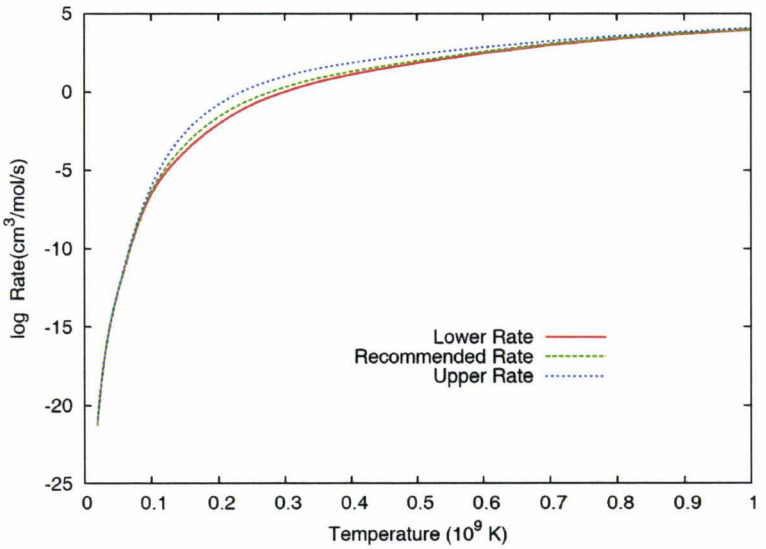

Figure 3.1: The reevaluated lower, recommended and upper limits of the ^{23}Na(p,α)^{20}Ne reaction rate as a function of temperature.

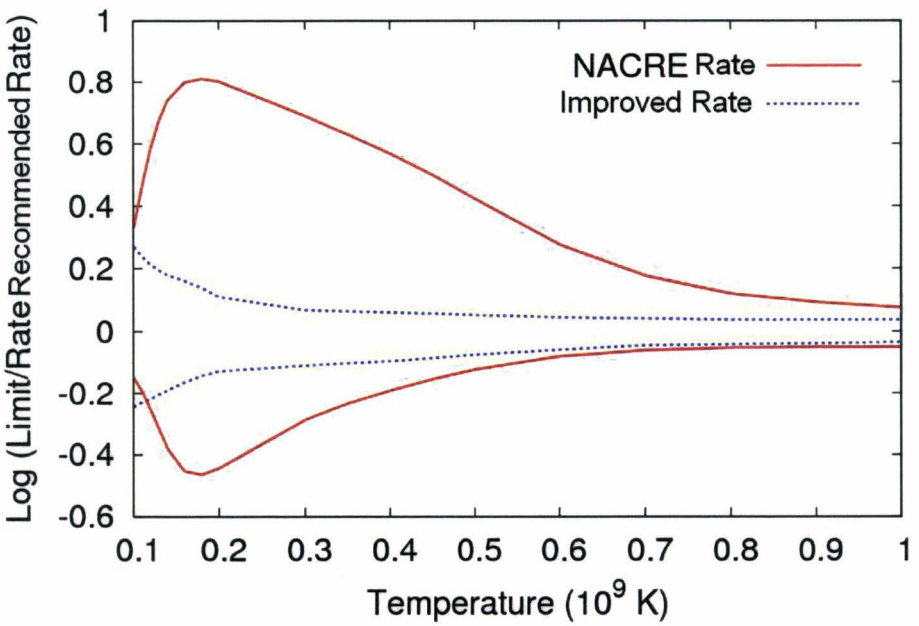

Figure 3.2: In this figure, we have plotted the ratio of the upper and lower limits to the recommended ^{23}Na(p,α)^{20}Ne reaction rate (in units of cm^3/mole/s) vs. temperature. It shows the uncertainty range as a function of temperature in the reevaluated rate compared to that calculated by NACRE. The uncertainty range in the reevaluated reaction rate is reduced to about 20% of that of NACRE at $T_9 = 0.2$.

Table 3.3: The REACLIB fit parameters for the ^{23}Na(p,α)^{20}Ne reaction rate.

Values of the REACLIB Parameters
a_1 = -0.4616e+01
a_2 = 0.5332e+00
a_3 = -0.5166e+04
a_4 = 0.5948e+04
a_5 = -0.7786e+03
a_6 = 0.8039e+00
a_7 = 0.2371e+02
a_8 = -0.4223e+03
a_9 = 0.1872e+01
a_{10} = -0.2293e+03
a_{11} = 0.7890e+03
a_{12} = -0.1840e+03
a_{13} = 0.5425e+02
a_{14} = -0.2317e+03
a_{15} = 0.8614e+02
a_{16} = -0.7385e-01
a_{17} = 0.2221e+02
a_{18} = -0.5386e+02
a_{19} = -0.1133e+03
a_{20} = 0.6638e+02
a_{21} = 0.4996e+02

3.3.2 The ^{23}Na(p,γ)^{24}Mg Reaction Rate

The rate of the ^{23}Na(p,γ)^{24}Mg reaction used to carry large uncertainty that amounted to a factor of 100 to 10^4 at certain temperature regions [78] due to an uncertain contributions of low energy resonances below $E_{c.m.} = 170$ keV. Since then, this reaction has been investigated more carefully [73, 76, 79].

In 2004 at TUNL, Hale *et al.* [73] have calculated this rate, and their result differs from that of NACRE for temperatures below $T_9 \sim 0.2$. This is due to the fact that the contribution of the direct capture to this rate was neglected by NACRE. But, Hale *et al.* have calculated the cross section for the direct capture and have found the contribution of the direct capture to the ^{23}Na(p,γ)^{24}Mg reaction rate.

In 2005 at TUNL, Iliadis *et al.* [76] have studied the ^{23}Na(p,γ)^{24}Mg reaction, and they have reduced the upper limit on the $E_{c.m} = 138$ keV resonance strength for the ^{23}Na(p,γ)^{24}Mg reaction by a factor of 33. Moreover, they have achieved an improvement on the estimation of the upper limit of the (p,α) resonance strength for the same resonance.

We have used this recent experimental information to calculate the ^{23}Na(p,γ)^{24}Mg reaction rate. For $T_9 \leq 0.03$, this rate is dominated by direct capture (see chapter 2), and by the contributions of individual resonances [73].

The contribution from the direct capture is described by the following analytical expression [73]:

$$N_A < \sigma v >_{\rm DC} = 4.26 \times 10^8 \, T_9^{-\frac{2}{3}} \, exp(-\frac{20.769}{T_9^{1/3}} - (\frac{T_9}{0.2})^2)$$

$$\times [1 - 0.26\,T_9 - 0.14\,T_9^2 + 0.038\,T_9^3] \qquad (3.6)$$

where T_9 is the temperature in units of GK.

The contributions of the individual resonances are given by the equation (2.49), where the resonance energies and their strengths are given in Table 3.4.

The total rate would then be:

$$N_A < \sigma v >_{\rm tot} = N_A < \sigma v >_{\rm DC} + N_A < \sigma v >_{\rm R} \qquad (3.7)$$

The recommended, upper and the lower limits of this rate are calculated the

Table 3.4: ^{24}Mg resonances below 1 MeV which contribute to the ^{23}Na(p,γ)^{24}Mg reaction rate, and their properties.

Resonance Energy[a]	Resonance Strength[b]	Reference 1[c]	Reference 2[d]
5.3	1.6×10^{-56}	Hale *et al.* (2004)[e]	Hale *et al.* (2004)
36.9	$\leq 1.3\times10^{-24}$	Hale *et al.* (2004)	Hale *et al.* (2004)
138.0 $\pm$ 2.9	$\leq 1.5\times 10^{-7}$	NACRE[f]	Iliadis *et al.* (2005)[g]
169.5	$(1.20 \pm 0.35)\times10^{-9}$	Hale *et al.* (2004)	Hale *et al.* (2004)
240	5.29×10^{-10}	Hale *et al.* (2004)	Hale *et al.* (2004)
295	1.05×10^{-7}	Hale *et al.* (2004)	Hale *et al.* (2004)
442	1.33×10^{-7}	Hale *et al.* (2004)	Hale *et al.* (2004)
533	2.75×10^{-7}	Hale *et al.* (2004)	Hale *et al.* (2004)

[a] in units of keV
[b] in units of eV
[c] The references from which the resonance energies are adopted.
[d] The references from which the resonance strengths are adopted.
[e] Ref. [73]
[f] Ref. [75]
[g] Ref. [76]

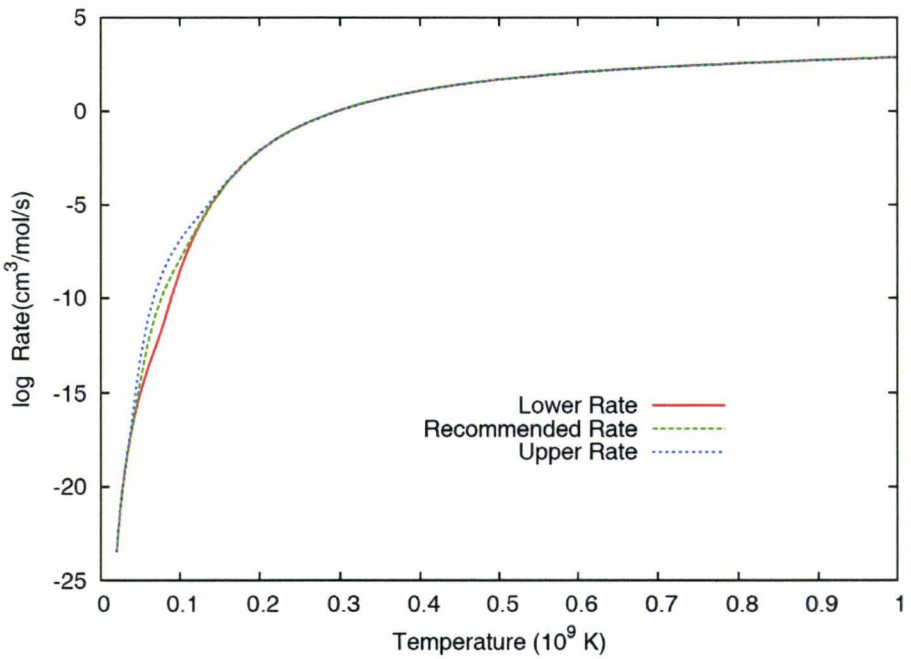

Figure 3.3: The reevaluated lower, recommended and upper limits of the ^{23}Na(p,γ)^{24}Mg reaction rate as a function of temperature.

same way as those of the ^{23}Na(p,α)^{20}Ne reaction rate. The values of the recommended, lower and upper limits of the rate are given in Table 3.5, and the rates are shown in Fig. 3.3. Fig. 3.4 shows the variation between the lower and the upper limits of this rate, so it is a measure of the uncertainty range in this rate. The reevaluated uncertainty range for the ^{23}Na(p,γ)^{24}Mg reaction rate is reduced to about 97% of that of NACRE over $T_9 \leq 0.1$. This rate can be converted to the REACLIB format, which is given by equation (3.5), where the parameters a_1 to a_{21} are displayed in Table 3.6.

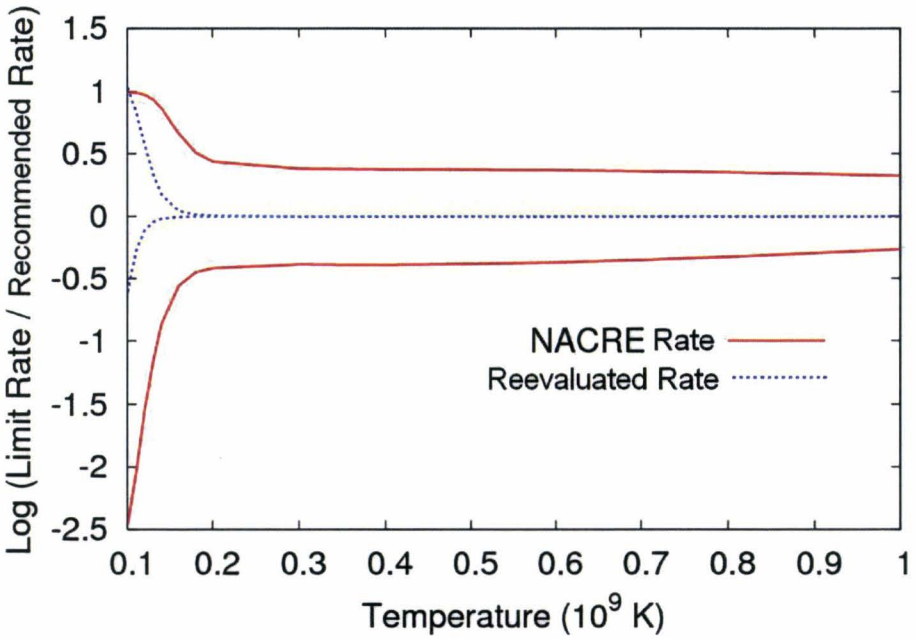

Figure 3.4: In this figure, we have plotted the ratio of the upper and lower limits to the recommended ^{23}Na(p,γ)^{24}Mg reaction rate (in units of cm^3/mole/s) vs. temperature. It shows the uncertainty range as a function of temperature in the reevaluated rate compared to that calculated by NACRE. The uncertainty range in the reevaluated reaction rate is reduced to about 97% of that of NACRE over $T_9 \leq 0.1$.

Table 3.5: The lower, recommended and upper limits of the $^{23}Na(p,\gamma)^{24}Mg$ reaction rate (in units of $cm^3/mole/s$) as a function of temperature.

T_9	Lower	Recommended	Upper
0.0200	3.47e-24	3.47e-24	3.51e-24
0.0300	4.17e-20	4.17e-20	4.18e-20
0.0350	1.07e-18	1.07e-18	1.20e-18
0.0400	1.54e-17	1.67e-17	4.41e-17
0.0450	1.48e-16	2.36e-16	2.02e-15
0.0500	1.03e-15	3.69e-15	5.31e-14
0.0600	2.53e-14	4.46e-13	7.40e-12
0.0700	3.50e-13	1.55e-11	2.45e-10
0.0800	5.54e-12	2.22e-10	3.30e-09
0.0900	1.40e-10	1.82e-09	2.45e-08
0.100	2.78e-09	1.13e-08	1.21e-07
0.110	3.59e-08	6.74e-08	4.64e-07
0.120	3.21e-07	4.14e-07	1.55e-06
0.130	2.13e-06	2.36e-06	5.12e-06
0.140	1.11e-05	1.16e-05	1.74e-05
0.160	1.67e-04	1.68e-04	1.88e-04
0.180	1.40e-03	1.40e-03	1.45e-03
0.200	7.66e-03	7.67e-03	7.77e-03
0.300	1.18e+00	1.18e+00	1.18e+00
0.350	4.73e+00	4.73e+00	4.73e+00
0.400	1.31e+01	1.31e+01	1.31e+01
0.450	2.85e+01	2.85e+01	2.85e+01
0.500	5.25e+01	5.25e+01	5.25e+01
0.600	1.28e+02	1.28e+02	1.28e+02
0.700	2.40e+02	2.40e+02	2.40e+02
0.800	3.86e+02	3.86e+02	3.86e+02
0.900	5.64e+02	5.64e+02	5.64e+02
1.00	7.76e+02	7.76e+02	7.76e+02

Table 3.6: The REACLIB fit parameters for the ^{23}Na(p,γ)^{24}Mg reaction rate.

Values of the REACLIB Parameters
a_1 = -0.5692e+03
a_2 = -0.1412e+00
a_3 = -0.2983e+01
a_4 = 0.1074e+04
a_5 = -0.1064e+04
a_6 = 0.5626e+03
a_7 = -0.6711e+02
a_8 = -0.1117e+06
a_9 = -0.6423e+04
a_{10} = -0.4823e+05
a_{11} = 0.7672e+04
a_{12} = -0.4563e+05
a_{13} = 0.1991e+06
a_{14} = -0.3651e+05
a_{15} = 0.1720e+03
a_{16} = -0.1803e+01
a_{17} = 0.2732e+02
a_{18} = -0.2020e+03
a_{19} = -0.9607e+00
a_{20} = 0.1221e+02
a_{21} = 0.6039e+02

3.3.3 The ^{26g}Al(p,γ)^{27}Si Reaction Rate

The knowledge of this reaction rate helps us understand the sources for production of 1.809 MeV γ-rays that are emitted by the decay of ^{26g}Al that have been observed by COMPTON Gamma Ray Observatory [80, 81, 82], the Gamma Ray Imaging Spectrometer (GRIS) [83], and more recently by INTEGRAL satellite [84, 85, 86]. With understanding of this rate, we can infer the less dominant contributions of the AGB stars to the Galactic ^{26}Al. The uncertainty in this rate is expected to have a large effect on the AGB yields of ^{26}Al and ^{27}Al [35]. So, in this subsection, we will use the latest experimental results [87], and will calculate this reaction rate. In the next section, we will determine its impact on the AGB yields.

One of the major uncertainties in reactions of the MgAl cycle corresponds to that of the ^{26g}Al(p,γ)^{27}Si reaction rate, whose uncertainty used to be as large as 10^3 at temperatures over 50 million K [78]. The uncertainty associated with this rate was due to unknown low energy resonance parameters [75]. But more importantly, this rate was known to be dominated by a single resonance with a center-of-mass energy of 188 keV, whose resonance strength was uncertain. This introduced a large uncertainty in the ^{26g}Al(p,γ)^{27}Si reaction rate. As a result, this reaction has been recently investigated [87] for the measurement of the resonance strength of that particular resonance.

In 2006, Ruiz *et al.* [87] studied the ^{26g}Al(p,γ)^{27}Si reaction rate in inverse kinematics with the help of DRAGON recoil separator in ISAC facility at TRIUMF. Surprisingly, they found that the energy of the single resonance that dominates the rate is 184 $\pm$ 1 keV in the center-of-mass system. Since the reaction rate depends exponentially on the resonance energy, a reduction in the resonance energy (with respect to NACRE's adopted resonance energy, which was 188 keV) results in an increase in the reaction rate. Moreover, their result for the measured resonance strength was 55% of that of NACRE. So, overall with the recent measurement, this rate should be reduced which means more ^{26}Al is survived.

In order to calculate this reaction rate, we have used the following information found in the literature:

- At any given temperature, the ^{26g}Al(p,γ)^{27}Si reaction may proceed via di-

rect capture (DC) and through the tails of high-energy or sub-threshold resonances [88]. In general, these non-resonant contributions are significant if there are individual resonances at the Gamow window, as is the case for ^{27}Si. The contribution of direct capture to this rate was calculated by Champagne *et al.* [88].

- There are a number of individual resonances that also contribute to this reaction rate. These resonances and their strengths are listed in Table 3.7, and their contributions to the reaction rate are calculated via equation (2.49). It should be noted that all the resonance energies and their corresponding strengths in Table 3.7 are adopted from Ref. [75], except for the resonance with the energy of 184 keV. This latter resonance energy and its corresponding resonance strength are adopted from Ref. [87].

So the total reaction rate is:

$$N_A < \sigma v >_{tot} = N_A < \sigma v >_{DC} + N_A < \sigma v >_R \tag{3.8}$$

where $N_A < \sigma v >_R$ is the resonant reaction rate. We evaluated the recommended rate and the limits using the same approach as for the ^{23}Na + p reaction rates.

Table 3.8 lists the values of the recommended rate as well as the limits as functions of temperature, and the rates are shown in Fig. 3.5. For comparison, we have plotted NACRE's recommended rate as well. The new recommended rate is higher than that of NACRE by up to 30%. This is due to the fact that we have added the contribution of the direct capture. Fig. 3.6 shows the uncertainty range was about four orders of magnitude in the temperature range of interest prior to recent measurement. However, the new uncertainty range is significantly reduced by about one order of magnitude. The REACLIB format of this rate is given by equation (3.5), where the 21 parameters are given in Table 3.9. In the following section, we will investigate the impact of these improved reaction rates on the AGB yields.

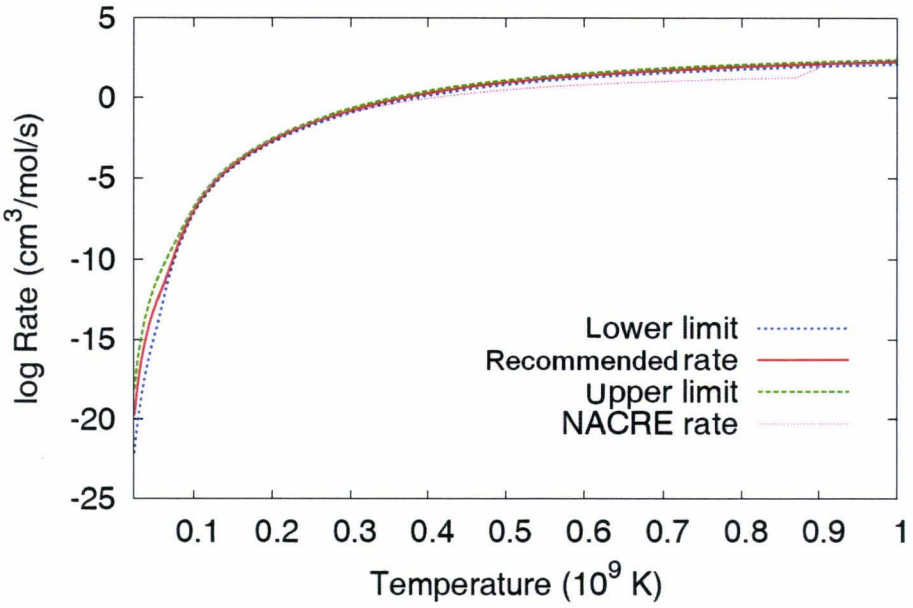

Figure 3.5: The reevaluated lower, recommended and upper limits of the ^{26g}Al(p,γ)^{27}Si reaction rate as a function of temperature, The purple curve is the NACRE's recommended rate. The new recommended rate is higher than that of NACRE by about 30%.

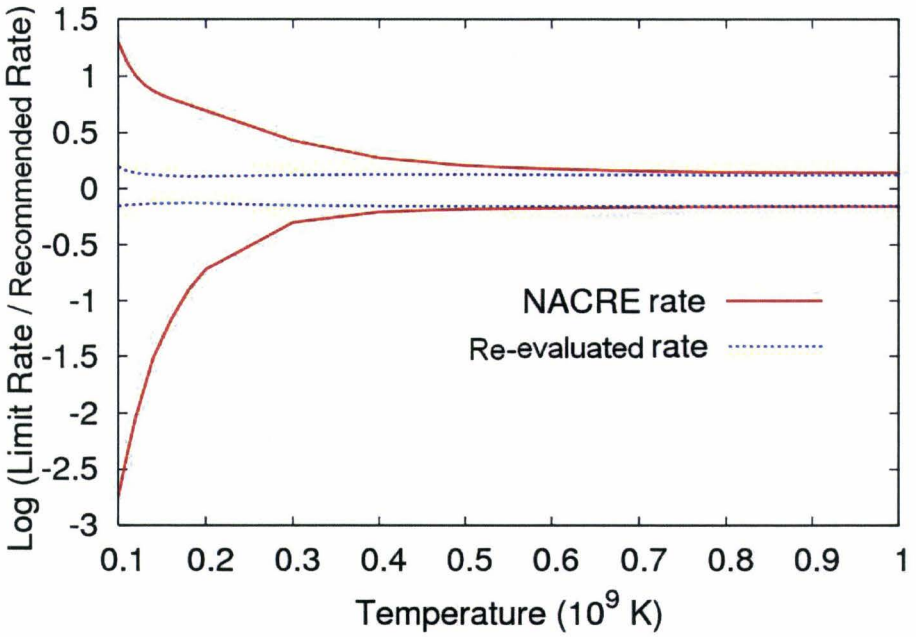

Figure 3.6: In this figure, we have plotted the ratio of the upper and lower limits to the recommended ^{26g}Al(p,γ)^{27}Si reaction rate (in units of cm^3/mole/s) vs. temperature. The uncertainty range was about four orders of magnitude in the temperature range of interest prior to the recent measurement; however, it is significantly reduced now ($\sim$ 1 order of magnitude).

Table 3.7: ^{27}Si resonances below 1 MeV, which contribute to the ^{26g}Al(p,γ)^{27}Si reaction rate, and their properties.

Resonance Energy[a]	Resonance Strength[b]		
	lower	recommended	upper
4 ± 3	2.9×10^{-76}	1.5×10^{-75}	2.7×10^{-75}
68 ± 3	2×10^{-13}	2.2×10^{-11}	2.2×10^{-10}
93 ± 3	2.3×10^{-10}	5.3×10^{-9}	5.3×10^{-8}
128 ± 3	0	5.9×10^{-7}	5.9×10^{-6}
184 ± 1	28×10^{-3}	35×10^{-3}	42×10^{-3}
226 ±3	0	0	0
238 ± 3	4.3×10^{-3}	4.7×10^{-3}	5.0×10^{-3}
275.6 ± 0.3	2.8	3.8	4.8
328 ± 4	0.19	0.2	0.22
363 ± 3	47	65	83
693 ± 2	24	51	78
701 ± 2	10	16	4
762 ± 2	22	35	48
825 ± 3	25	41	57
894 ± 2	39	67	95

[a] in units of keV
[b] in units of meV

Table 3.8: The lower, recommended and upper limits of the ^{26g}Al(p,γ)^{27}Si reaction rate as a function of temperature. The rates are in units of cm^3/mole/s.

T_9	Lower	Recommended	Upper
0.020	1.28e-25	9.28e-24	5.23e-22
0.030	1.06e-20	2.61e-18	8.33e-17
0.040	9.80e-18	1.41e-15	3.35e-14
0.050	1.12e-15	7.80e-14	1.56e-12
0.060	1.17e-13	1.62e-12	2.66e-11
0.070	1.20e-11	3.21e-11	2.69e-10
0.080	4.44e-10	7.35e-10	2.38e-09
0.090	7.31e-09	1.08e-08	2.09e-08
0.10	6.79e-08	9.70e-08	1.52e-07
0.11	4.16e-07	5.83e-07	8.38e-07
0.12	1.87e-06	2.59e-06	3.57e-06
0.13	6.68e-06	9.16e-06	1.23e-05
0.14	1.99e-05	2.71e-05	3.59e-05
0.16	1.20e-04	1.62e-04	2.11e-04
0.18	5.09e-04	6.87e-04	8.87e-04
0.20	1.72e-03	2.33e-03	3.00e-03
0.30	1.19e-01	1.67e-01	2.21e-01
0.40	1.42e+00	2.04e+00	2.73e+00
0.50	6.72e+00	9.67e+00	1.29e+01
0.55	1.18e+01	1.70e+01	2.27e+01
0.60	1.88e+01	2.70e+01	3.60e+01
0.65	2.78e+01	3.99e+01	5.30e+01
0.70	3.86e+01	5.54e+01	7.35e+01
0.75	5.12e+01	7.32e+01	9.70e+01
0.80	6.52e+01	9.32e+01	1.23e+02
0.85	8.04e+01	1.15e+02	1.52e+02
0.90	9.65e+01	1.38e+02	1.82e+02
0.95	1.13e+02	1.62e+02	2.14e+02
1.0	1.31e+02	1.87e+02	2.46e+02

Table 3.9: The REACLIB fit parameters for the ^{26g}Al(p,γ)^{27}Si reaction rate.

Values of the REACLIB Parameters
a_1 = -0.2959e+02
a_2 = -0.1761e+00
a_3 = 0.1384e+02
a_4 = 0.1474e+03
a_5 = -0.2840e+03
a_6 = -0.4323e+03
a_7 = 0.2458e+02
a_8 = 0.8644e+02
a_9 = -0.3795e+00
a_{10} = -0.1788e+02
a_{11} = -0.7382e+02
a_{12} = 0.1273e+02
a_{13} = -0.1761e+01
a_{14} = 0.1188e+02
a_{15} = 0.3920e+04
a_{16} = 0.3389e+02
a_{17} = -0.2877e+04
a_{18} = -0.2628e+04
a_{19} = -0.2682e+04
a_{20} = 0.1729e+04
a_{21} = -0.1425e+04

3.4 Summary of the Yield Results

In order to calculate the stellar yields presented in this chapter, Dr. Amanda Karakas[10] has used the Monash version of the Mount Stromlo Stellar Structure Code [15], and has calculated evolutionary sequences for a $6\,M_{\odot}$ AGB star[11] with three different metallicities, e.g. $Z = 0.02$ (solar); 0.008 (Large Magellanic Cloud); and 0.004 (Small Magellanic Cloud). Then, recently the post-processing nucleosynthesis computations on those three models were performed. Nucleosynthesis processes include proton captures in the H-shell, and at the base of the convective envelope; and alpha and neutron captures in the He-shell.

For each of the three stellar structure models, the nucleosynthesis code was computed four times: the first model is based on the standard set of the reaction rates[12] (hereafter, we call this model "standard model"); the second model is based on changing the ^{23}Na(p,γ)^{24}Mg, reaction rate in the standard set of rates to its updated value discussed in the previous section; the third model is based on changing the ^{23}Na(p,α)^{20}Ne reaction rate to its updated value; and the last model is based on changing the ^{26g}Al(p,γ)^{27}Si reaction rate to its updated value. Thus, for each metallicity, a standard set of yields for 77 species; and another three sets of yields that resulted from using one of the updated rates have been obtained. The percentage differences between the standard set of yields and the other sets of yields for 77 species for each metallicity were computed.

In this thesis, we only present the stellar yields in units of solar masses for 22 species with A = 20 - 30 in tabular forms in Appendix A. Because, in general the reaction rates associated with the NeNa and MgAl chain mostly affect ^{20}Ne to ^{30}Si isotopes. Figures 3.7 to 3.9 display the time variation of the surface abundances of

[10]Post doctoral researcher at the Research School of Astronomy & Astrophysics, Mt Stromlo Observatory, Australia.

[11]The $6\,M_{\odot}$ AGB star is selected, because generally any changes to the yields are most obvious in this mass range.

[12]The bulk of 527 reaction rates are from REACLIB data tables based on the 1991 updated version; however, some of the proton, alpha and neutron capture reaction rates have been updated to the latest experimental results. In particular, the proton capture rates for the NeNa and MgAl chains have been updated to those recommended by NACRE; and the ^{22}Ne(α,n) and ^{22}Ne(α,γ) rates have been updated to those calculated in Ref. [25]. To perform the models, these reaction rates are used as the standard set of reaction rates, and will lead to obtaining the standard set of yields.

selected species during the thermally-pulsing AGB phase of evolution for the $6\,M_{\odot}$, $Z = 0.004$ model. The y-axes in these plots are in log Y, where Y is the mole fraction and is equal to $Y = \frac{\text{mass fraction X}}{\text{Atomic mass}}$. In each diagram, $t = 0$ corresponds to the time from the beginning of the TP-AGB phase.

It should be noted that, the differences in yields on the order of 5% or less can be ignored. We have only listed those isotopes, for which the percentage differences (between the standard yields and the yields obtained by application of one of the improved reaction rates at a time) are higher than 5%. By comparing the standard yields to the yields computed utilizing the updated rates, we draw the following conclusions:

- Using the updated ^{23}Na(p,γ)^{24}Mg reaction rate in models with three different metallicities:
  - ◇ All three models show more production of ^{20}Ne and more destruction of ^{24}Mg. This is especially apparent for the $6\,M_{\odot}$, $Z = 0.02$ model, where the percentage difference between the new ^{20}Ne yield (using the new rate) and the ^{20}Ne standard yield is on the order of 10^2; and the highest percentage difference between the ^{24}Mg new yield and the ^{24}Mg standard yield is obtained by the $Z = 0.008$ and $Z = 0.02$ models and is on the order of 10^2. The percentage differences for these two isotopes obtained by the $Z = 0.004$ model are 44% and 51%, respectively.
  - ◇ All three models show an increase in the ^{23}Na yield. The highest percentage difference between the new ^{23}Na yield and the ^{23}Na standard yield is obtained for the $Z = 0.004$ and $Z = 0.008$ models, which is about 34%.
  - ◇ The yields of Mg and Al isotopes are less affected. All three models show small decreases in the yields of ^{25}Mg, ^{26}Mg and ^{26}Al (maximum of 15% for the yield of ^{25}Mg in the $Z = 0.004$ model). Thus, ^{27}Al is also less produced (maximum of 25% difference for the $Z = 0.008$ model).
  - ◇ Compared to the standard model, all three models that use the new ^{23}Na(p,γ)^{24}Mg reaction rate produce less ^{28}Si, ^{29}Si and ^{30}Si. This is because these Si isotopes are produced by proton capture on ^{27}Al, and all these models produce less ^{27}Al compared with the standard model. The

maximum percentage difference between the new ^{28}Si yield and the standard one is obtained by the $Z = 0.02$ model and is on the order of 10^2. The most apparent percentage differences between the new ^{29}Si and ^{30}Si yields and the standard ones are obtained by the $Z = 0.004$ model, which are on the order of 25% and 16%, respectively.

- Using the updated ^{23}Na(p,α)^{20}Ne reaction rate in all three models:

  - ◇ All three models show more production of ^{24}Mg and more destruction of ^{20}Ne. Note that the new yields of ^{20}Ne in all the three models are negative (i.e., ^{20}Ne is destroyed), compared to the positive ^{20}Ne standard yields. This is because the updated ^{23}Na(p,α)^{20}Ne reaction rate for all temperatures is lower than that used to calculate the standard set of yields. It should be noted that this reaction is the last reaction in the NeNa cycle, which feeds the cycle by production of ^{20}Ne. Thus, a smaller rate for this reaction leads to less efficient ^{20}Ne production, and overall this isotope will be destroyed by proton capture reactions. the maximum percentage difference between the new ^{20}Ne yield (using the new rate) and the ^{20}Ne standard yield is obtained by the $Z = 0.02$ and $Z = 0.008$ models, and is on the order of 10^2. ^{24}Mg is produced more due to the higher ^{23}Na(p,γ)^{24}Mg reaction rate. The maximum percentage difference between the standard yield of this isotope and its new yield is obtained by the $Z = 0.008$ model, and is 48%.

  - ◇ All three models show an increase in ^{23}Na yield. For the $Z = 0.004$ model, this increase is about 53%. This is due to the fact that: the temperature at the base of the envelope for this model is higher than in the other two models (i.e., 94 MK for $Z = 0.004$ model, 82 MK for $Z = 0.02$ model and 89 MK for $Z = 0.008$ model); and the duration of the HBB phase is also longer for this particular model.

  - ◇ The yields of Mg and Al isotopes are only slightly affected. All three models show small increases in the yields of ^{25}Mg, ^{26}Mg and ^{26}Al (maximum percentage difference is for ^{25}Mg in the $Z = 0.004$ model, which is on the order of 9%.). These increases are due to the existence of more ^{24}Mg.

Due to the increase in the yield of ^{26}Mg, ^{27}Al is also produced in small quantities (maximum of 26% difference for the $Z = 0.008$ model).

- ◇ Compared to the standard model, all three models that use the new ^{23}Na(p,α)^{20}Ne reaction rate produce more ^{28}Si, ^{29}Si and ^{30}Si. This is because these Si isotopes are produced by proton capture on ^{27}Al, and all these models produce more ^{27}Al compared with the model that results the standard set of yields. The maximum percentage difference between the new ^{28}Si yield and the standard one is obtained by the $Z = 0.02$ model and is about 95%. The most apparent percentage differences between the new ^{29}Si and ^{30}Si yields and the standard ones are obtained by the $Z = 0.004$ model, which are on the order of 27% and 17%, respectively.

- Using the updated ^{26g}Al(p,γ)^{27}Si reaction rate in all three models, led to no significant effect on the stellar yields except for the yield of ^{28}Si obtained by the $Z = 0.02$ model, where the percentage difference between this new yield and the standard one is on the order of 27%. The fact that the ^{26g}Al(p,γ)^{27}Si reaction rate had no significant effect on the yields (except for the yield of ^{28}Si) is that in the AGB temperature range of interest (60 to 100 MK), the ^{26g}Al(p,γ)^{27}Si recommended reaction rate that we used was almost identical to that of NACRE, which is used in the standard model.

To summarize, we have explored the changes to the yields, where we have only changed one reaction rate to its updated value at a time to see the effect of each rate on the yields, and we have seen noticeable effects for some isotopes: the percentage differences between the new yields and the standard ones differ from a few percent to differences on the order of 10^2 for some isotopes in the mass range of $20 < A < 30$.

By coincidence, for most of the isotopes, the yield results were exactly opposite for the cases of using the ^{23}Na(p,γ)^{24}Mg and the ^{23}Na(p,α)^{20}Ne reaction rates: while using one of these reaction rates leads to destruction of some isotopes, the effect of using the other reaction rate is production of those isotopes; hence, for most of the isotopes, their effects cancel out. The ^{26g}Al(p,γ)^{27}Si reaction rate had no noticeable effect on any of the yields except for the yield of ^{28}Si obtained by the $Z = 0.02$

model.

To find out the impact of the improved reaction rates on the AGB yields, the total yields (resulting by the application of these three improved reaction rates altogether and simultaneously in the nucleosynthesis network) are simply computed by adding the yields resulting from using one reaction rate at a time, and calculating the percentage differences between the total yields and the standard ones. Doing so results in:

- Destruction of ^{20}Ne with the maximum percentage difference obtained by the $Z = 0.02$ model, which is on the order of 10^2.
- Production of ^{24}Mg with the maximum percentage difference obtained by the $Z = 0.008$ model, which is on the order of 10^2.
- Production of ^{23}Na with the maximum percentage difference of 87% obtained by the $Z = 0.004$ model.
- Production of ^{28}Si with the maximum percentage difference of 40% obtained by the $Z = 0.02$ model.

From the next chapter, we begin part II of this thesis, in which we try to determine the feasibility of studying the structures of ^{26}Si and ^{30}S experimentally via the ^{20}Ne(^{12}C,^{6}He)^{26}Si and ^{12}C(^{24}Mg,^{6}He)^{30}S reactions.

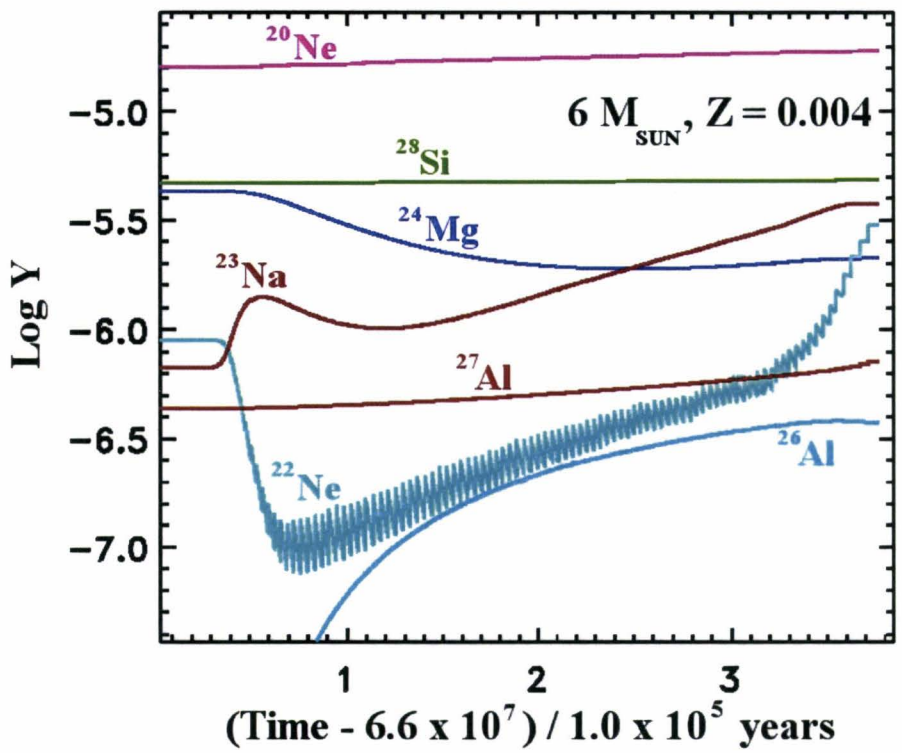

Figure 3.7: The time variation of selected surface abundances for the $6\,M_{\odot}$, $Z = 0.004$ model. The abundances of all species are given as the logarithm of the mole fraction, $\log Y$. Note that in this plot the standard set of reaction rates was used.

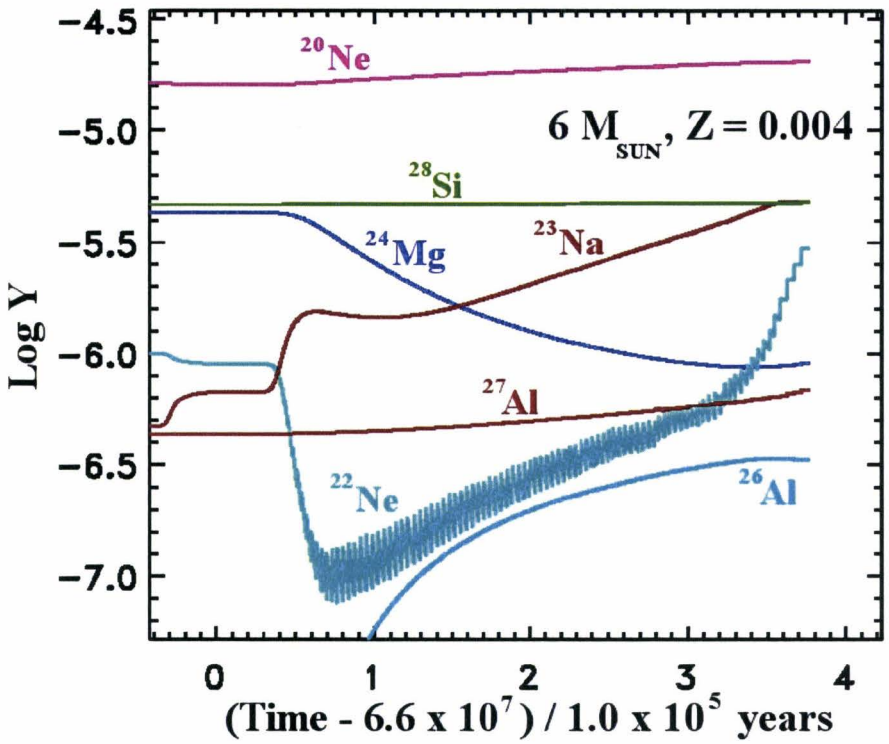

Figure 3.8: The time variation of selected surface abundances for the $6\,M_{\odot}$, $Z = 0.004$ model. The abundances of all species are given as the logarithm of the mole fraction, $\log Y$. Note that in this plot the updated ^{23}Na(p,γ)^{24}Mg reaction rate was used. The surface abundance of ^{22}Ne oscillates, because the third dredge-up processes, that occur after each thermal pulse, bring ^{22}Ne from the He-shell into the inter-shell region, and thus the surface abundance of ^{22}Ne is enhanced by the third dredge-up process. When the pulse dies down and the interpulse phase begins, the ^{22}Ne is destroyed by the HBB and the α-capture reactions. The third dredge-up processes take place relatively quickly (on the order of a few hundred years) compared to the longer interpulse periods, which last over a few thousand years [89]. Thus, the surface abundance of ^{22}Ne increases very sharply and quickly with the third dredge-up processes, and decreases more slowly during the interpulse periods.

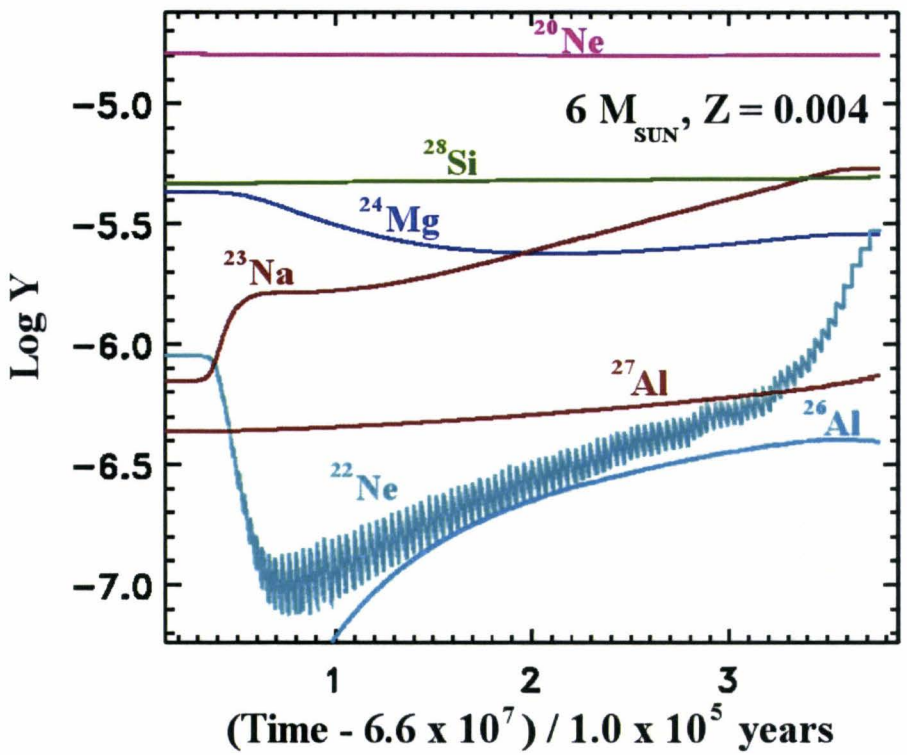

Figure 3.9: The time variation of selected surface abundances for the $6\,M_{\odot}$, $Z = 0.004$ model. The abundances of all species are given as the logarithm of the mole fraction, $\log Y$. Note that to obtain this plot, the updated ^{23}Na(p,α)^{20}Ne reaction rate was used.

3.5 Future Work

Broad variation in the abundances of some lighter elements in globular clusters has been one open question [90]. It has been thought that these variations are potentially related to AGB nucleosynthesis [90]. There is a growing list of globular cluster stars known to have large star-to-star abundance anomalies, mainly O-Na and Mg-Al anti-correlations, at different stages of evolution. One of the main hypotheses to explain the strange chemical properties observed in globular cluster stars is chemical pollution from previous stellar generations [91]. The detection of O-Na and Mg-Al anti-correlations in less evolved stars [44] suggests that these chemical patterns were already present in the gas from which these stars formed. The most popular candidates for introducing Na- and Al-rich, O- and Mg-poor gas into the cluster are 4 - 7 $M_{\odot}$ AGB stars. In order to confirm this, one needs to obtain more reliable O, Ne, Na, Mg and Al yields from the intermediate-mass AGB stars. Thus, the uncertainty ranges in the yields of such isotopes need to be reduced. Recently, Izzard *et al.* [35] have investigated the impact of the uncertainty ranges in the reaction rates on the AGB yields; however, the reaction rates they have used are yet not the most updated ones as were calculated in this thesis.

In this project, we presented the yields, but it is worthwhile to try to calculate the AGB yields using the most updated ^{23}Na(p,γ)^{24}Mg, ^{23}Na(p,α)^{20}Ne, and ^{26g}Al(p,γ)^{27}Si lower and upper limit reaction rates discussed in this chapter so as to find the uncertainty ranges in the yields. This will help us explain the observed abundances and determine whether or not the AGB stars are candidates for introducing the Na- and Al-rich, O- and Mg-poor gas into the globular cluster stars. The yields and their uncertainties can also be used as an input to the galactic chemical evolution (GCE) models to investigate if the yields are able to reproduce the abundance patterns observed in the stars, interstellar medium and the galactic halos and disks[13].

[13]For more information, see Ref.[25, 35, 92]

Part II

Nuclear Level Structure and its Impact on Novae Nucleosynthesis

Chapter 4

The Nuclear Structure of ^{26}Si and ^{30}S and Nova Nucleosynthesis

The primary goal of this part of the thesis is to test whether or not one can pursue the studies of the nuclear level structure of ^{26}Si and ^{30}S via the (^{12}C,^{6}He) reaction mechanism. In this chapter, we review classical novae and their properties. We discuss their resulting nucleosynthesis. Finally, we narrow down our attention to ^{26}Si and ^{30}S and explore their influences on understanding nova nucleosynthesis.

4.1 Classical Novae

Classical novae are dramatic stellar explosions that are powered by thermonuclear runaway. They occur in interacting binary systems consisting of a compact white dwarf[1] and a low-mass Main Sequence companion. In such binary systems, the system is close enough (orbital periods < 10 - 12 hours [94]) to allow repetitive mass transfer from the companion main sequence star, which is caused by Roche Lobe overflow[2] through the inner Lagrangian point of the system [93]. Thus, an accretion disk is formed around the white dwarf. This disk contains H-rich material, a fraction of which is accumulated on the top of the white dwarf (at a rate of M $\sim 10^{-10}$ - 10^{-9}

[1]The stellar remnant of a main sequence star with a mass below $\sim 11\,M_{\odot}$, white dwarfs have planetary dimensions and masses typically in the range 0.6 - 1.4 $M_{\odot}$ [93].

[2]The first Roche Lobe overflow from the primary component occurs when hydrogen burning has begun in a shell and a deep convective envelope forms around the helium core [95]. This is when the companion star ascends through the Red Giant branch.

$M_{\odot}$ yr^{-1} [94]) as a result of angular momentum losses driven by dissipative forces in the disk [93]. This accreted material is gradually squeezed, and forms an envelope in a semi-degenerate condition until a violent thermonuclear runaway follows (see Fig. 4.1).

The thermonuclear runaway follows as a consequence the ignition of hydrogen. This is because: the degenerate matter cannot be expanded by the energy released by H-ignition, and thus radiation is not enough to transport the energy.

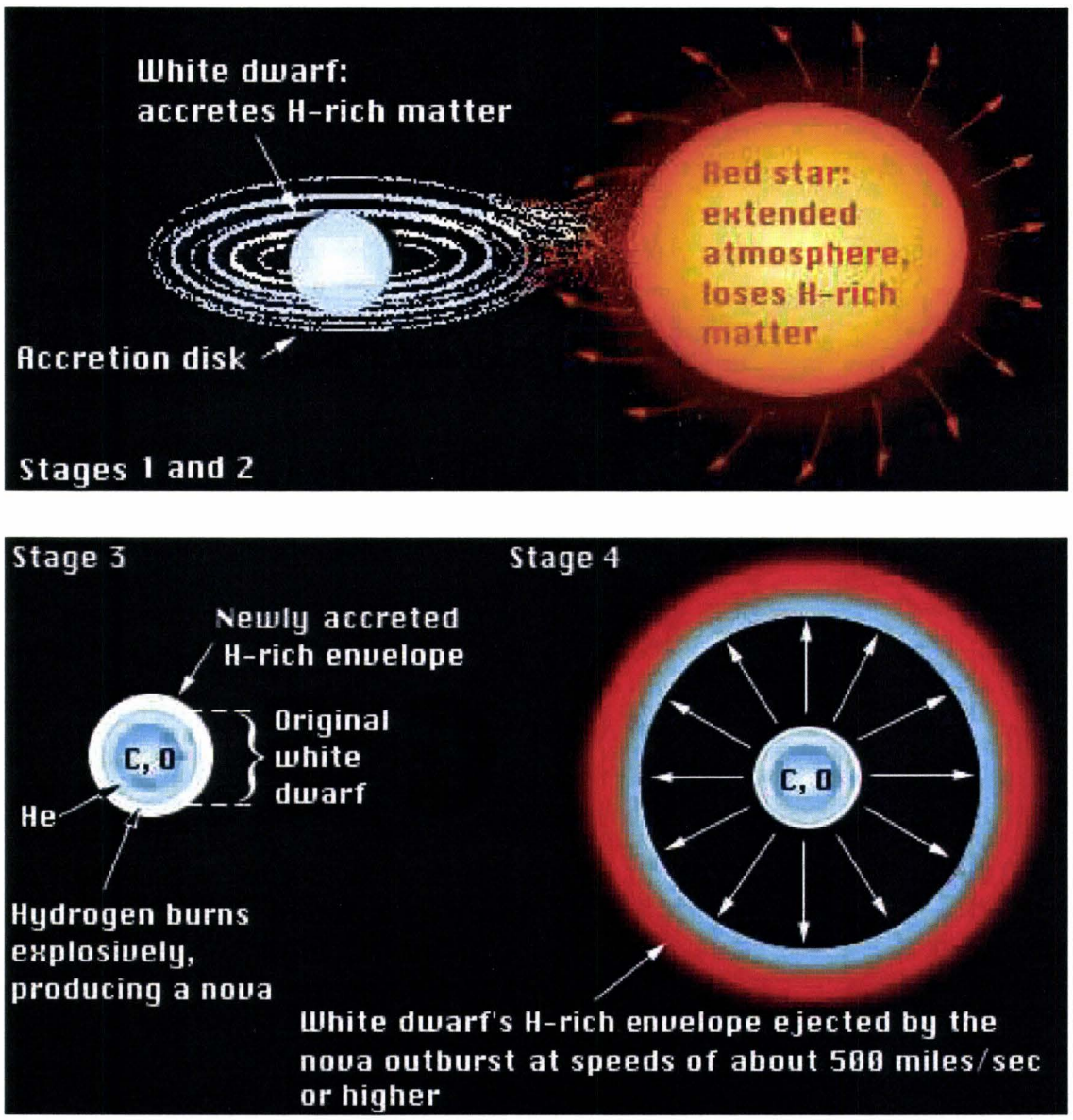

Figure 4.1: Anatomy of the classical nova outburst. Picture adopted from Ref. [96].

Thus, convection also sets in, and transports the β^+-unstable nuclei, e.g. ^{13}N, ^{14}O, ^{15}O, ^{17}F and ^{18}F (such nuclei are produced during hydrogen burning through the CNO cycle), to the outer cooler regions where they decay. The sudden release of energy as a result of β-decays raises the temperature, which in turn increases the entropy of the material. This reduces the pressure, and thus the degeneracy is lifted. Once the matter becomes non-degenerate, it will expand and expansion causes the thermonuclear runaway to be stopped temporarily [93]. However, unburned material from the lower-lying shells is transported into the H-burning shell by convection. Thus, non-equilibrium burning occurs, which leads to nucleosynthesis far from the hydrostatic hydrogen burning. As a result, thermonuclear runaway sets in again, but this time, the matter is non-degenerate and will expand to the point where the ejection of mass, and thus the outburst take place.

4.2 Properties of Classical Novae

There are two types of white dwarfs, which can proceed to the classical nova outbursts if they are in binary systems: carbon-oxygen (CO) and oxygen-neon (ONe) white dwarfs. The CO white dwarfs are remnants of low-mass AGB stars. In such stars, the carbon cannot be burned inside the core, and thus after the star finishes its evolution along the AGB phase, a white dwarf with a carbon- and oxygen-rich core will form that can stabilize itself by electron degeneracy pressure. In contrast, the ONe white dwarfs are remnants of more massive progenitors, whose cores were able to undergo non-degenerate carbon-burning when the progenitor was evolving through AGB phase of evolution. As stated in Ref. [93] and Ref. [94], misclassification is possible! This is due to the fact that in the process of the formation of ONe white dwarfs, carbon has to be ignited first. But, carbon ignition does not necessarily imply that burning is going to be extended enough in the CO core to change its composition drastically [95]. According to Ref. [95], carbon burning never proceeds at a significant rate when the progenitor's mass is below 9.0 - 9.3 $M_{\odot}$. Thus, when such progenitors are transformed into white dwarfs, the ONe cores are surrounded by a thick CO buffer [95]. If in such cases, the nova outburst occurs on top of such objects, there will not be evidence for strong neon lines in their spectra. Thus, such

outbursts may be misclassified as non-neon (CO) novae.

Classical novae are characterized by a sudden rise in optical brightness from 8 to 18 magnitudes in one to two days, with peak luminosities reaching $10^4 - 10^5$ $L_\odot$ [94]. The temperature that can be reached during the outburst is of order of 0.1 to 0.4 GK. Such stellar explosions can release energies of the order of 10^{45} ergs, and can eject 10^{-5} - 10^{-4} $M_\odot$ of material into the interstellar medium at typical velocities ranging from 10^2 - 10^3 km/s [94]. In contrast to the supernovae, where the whole star is fully disrupted, classical novae are expected to recur within a timescale of the order of 10^4 - 10^5 years [93]. The estimated number of nova events in our Galaxy is about ~ 35 yr^{-1} [40].

4.3 Nucleosynthesis in Classical Novae and Their Role in the Galactic Alchemy

Despite the fact that novae are common phenomena ($\sim$ 35 events per year), they are not main contributors to the interstellar matter enrichment. This is due to the low amount of ejected matter per outburst ($\sim 10^{-5}$ - 10^{-4} $M_\odot$).

The thermonuclear runaway in novae is triggered by the ^{12}C(p,γ)^{13}N reaction. Hydrogen then burns explosively via the hot CNO cycle[3]. The dominant nuclear reaction flow proceeds close to the valley of stability and is dominated by a series of (p,γ) and (p,α) reactions and β^+-decays [94]. Neutron- and α-capture reactions are completely negligible in classical novae [94].

The nucleosynthetic endpoint of classical novae is around Ca [94]; however, recent studies [97] show that the nucleosynthesis pattern and also the strength of the outburst in classical novae depend on the initial composition of the accreted material. Nova explosions in the most primitive low metallicity binaries (primordial novae), where the companion star is a metal-poor red giant star[4], are shown to be more energetic [97]. As a result, primordial novae eject a more massive envelope and display a larger nuclear activity than classical novae, where the companion star

[3]The sequence is: ^{12}C(p,γ)^{13}N(p,γ)^{14}O(β^+)^{14}N(p,γ)^{15}O(β^+)^{15}N(p,α)^{12}C.

[4]Intermediate-mass primordial stars climb the red giant branch for the first time when a He-burning shell is established [97]. Thus, the matter to be accreted from such red giants is less processed.

is a red giant star with solar metallicity[5] [97]. The massive ejected shells from the most violent primordial novae yield large excesses of Ti and a likely nucleosynthetic endpoint around Cu-Zn [97].

The composition of the underlying white dwarf determines the types and the amount of radioactive material synthesized during nova outbursts[6]. Because of the lower peak temperature achieved in CO novae, their main nuclear activity does not extend much beyond oxygen. In contrast, ONe novae show a much larger nuclear activity, extending up to silicon (for $1.15\,M_{\odot}$ ONe white dwarf) or argon (for $1.35\,M_{\odot}$ ONe white dwarf) [93]. However in general, classical novae play an important role on the Galactic content of ^{13}C, ^{15}N, and ^{17}O. Moreover, they have a lower contribution in a number of other species, e.g. ^{17}F, ^{18}F, ^{19}F, ^{20}Ne, ^{22}Na [100] and ^{28}Si [101]. They also contribute to $\sim$ 10% of the Galactic ^{7}Li content [99]. Classical novae are also responsible for the production of ~ 0.1 to $0.4\ M_{\odot}$ of galactic ^{26g}Al.

In the next section, we will focus our attention on ^{26}Si and ^{30}S and will discuss why it is crucial to explore their nuclear level structure.

4.4 Motivations behind Studying the Nuclear Structure of ^{26}Si and ^{30}S

The rate of production of galactic ^{26}Al is still an open question in the field of nuclear astrophysics. Novae may be an important source, but it is difficult to estimate their contribution because of uncertainties in the nova nucleosynthesis of ^{26}Al [102]. José *et al.* [103] investigated the effects of uncertainties in reaction rates on the production of ^{26}Al, and concluded that the dominant source of uncertainty in the yield from novae comes from the uncertainty in the ^{25}Al(p,γ)^{26}Si reaction rate.

[5]Solar-metallicity stars ascend through the red giant branch when H-burning sets in a shell [98]. Thus, the matter to be accreted from these red giants is more processed by subsequent burning and is mixed with metal-rich core-material due to convection and dredge-up processes.

[6]The material from the envelope should be mixed with that of the core of the underlying white dwarf for the explosion to occur and to explain the observed abundances. The CO novae mainly produce ^{7}Be , and the ONe novae are responsible for production of ^{22}Na and ^{26}Al. In the case where the explosion takes place on the top of the ONe white dwarf but in the overlying thick CO buffer, we would see ^{7}Be and ^{26}Al (from a non-negligible amount of ^{25}Mg in the CO buffer) but not ^{22}Na and ^{20}Ne [99].

This reaction rate still carries very large uncertainties in its rate which is related to the lack of nuclear structure information just above the proton threshold in the compound nucleus (i.e., ^{26}Si).

On another front, to better understand the nova nucleosynthetic paths, it is very important to gain information on the details of the explosions, which can be inferred by studying the Si isotopic ratios in presolar grains of nova origins. This is due to the fact that such ratios provide us with information about the nature of the underlying white dwarf and the peak temperatures achieved during the outburst [101]. In order to measure the Si isotopic abundances in presolar grains with high precision, it is crucial to know the rates of the thermonuclear reactions which affect the Si production and destruction in novae. One such reaction is the ^{29}P(p,γ)^{30}S, whose rate is still quite uncertain, and depends significantly on the level structure of the compound nucleus (i.e., ^{30}S), which is also not well understood. If the rate of this reaction is higher than that of the β^+-decay of ^{29}P, it directly affects the production of ^{30}Si via the ^{29}P(p,γ)^{30}S(β^+)^{30}P(β^+)^{30}Si reaction sequence, and it also changes the nucleosynthetic path away from ^{29}Si, which is the product of the β^+-decay of ^{29}P [7] [104]. According to Ref. [105], variation in the ^{29}P(p,γ)^{30}S rate has the effect of changing ^{30}Si abundance by a factor of $\leq$ 100. The ^{29}P(p,γ)^{30}S reaction rate also affects the subsequent production of ^{31}P, ^{33}S, ^{34}S, ^{35}Cl, ^{36}Ar, ^{37}Ar, ^{37}Cl, ^{38}Ar, ^{39}Kr and ^{40}Ca nuclei significantly [104]. So it has a profound influence not only on the silicon isotopic abundances, but also on the abundances of the heavier isotopes beyond silicon. This reaction rate also becomes important in X-ray bursts [106].

Thus, studying the ^{25}Al(p,γ)^{26}Si and ^{29}P(p,γ)^{30}S reaction rates to be able to reduce their uncertainty ranges in explosive hydrogen burning, is among the current important tasks for nuclear astrophysicists.

The ^{25}Al(p,γ)^{26}Si and ^{29}P(p,γ)^{30}S reactions have been investigated by many groups ([102, 107, 108] and [104, 109, 110], respectively) and are still under study. To better understand these two reaction rates, we need to study the structure of ^{26}Si and ^{30}S experimentally to try to find the important missing resonances that contribute to these reaction rates and investigate their properties.

[7] ^{29}Si and ^{30}Si are indicators of the peak temperatures achieved in the explosions [101]. Thus, they help us determine the dominant nuclear paths followed in the course of the thermonuclear runaway, and the overall composition of the ejecta.

4.4.1 Recent Measurements of the ^{26}Si Level Structure

^{26}Si is an unstable isotope of silicon with a half-life of 2.234 s for its ground state [111]. It decays to the metastable state of ^{26}Al through electron capture with the probability of 100%.

From comparison with the level structure of the very well studied stable nucleus ^{26}Mg, which is the mirror nucleus for ^{26}Si[8], Iliadis *et al.* [108] predicted several levels in ^{26}Si within the energy range of interest for novae that had not been observed [112]. In addition, of those states that had been observed, many had unknown spin-parity assignments or large ($\sim$ 30 keV) uncertainties in their excitation energies [112]. Thus, several groups have made measurements of ^{26}Si above the proton threshold since then.

For example, the structure of ^{26}Si has been studied by Caggiano *et al.* [113] via the ^{29}Si(^{3}He,^{6}He)^{26}Si reaction; Bardayan *et al.* [102, 114, 115] via the ^{28}Si(p,t)^{26}Si reaction[9]; Thomas *et al.* [116] via beta-decay; Parpottas *et al.* [117, 118] via the ^{24}Mg(^{3}He,n)^{26}Si reaction; Chen *et al.* [119, 120] via measurement of the ^{25}Al + p resonances with the p(^{27}Si,^{26}Si*)d reaction and the measurement of the ^{25}Al(p,p)^{25}Al reaction, respectively; and Seweryniak *et al.* [121] via γ-ray spectroscopy with the ^{16}O(^{12}C,2n)^{26}Si reaction. As a result of these studies, new excited states (up to $E_x(^{26}\text{Si}) \sim 8$ MeV) have been observed and spins and parities have been assigned to a few of those observed states through DWBA (Distorted Wave Born Approximation) angular distribution calculations; or by comparing measured differential cross sections with Hauser-Feshbach calculations. Tables 4.1 and 4.2 show the summary of these results, and Fig. 4.2 shows a schematic diagram of the level scheme of ^{26}Si.

[8]Mirror nuclei have the same number of total nucleons, but interchanged proton and neutron numbers.

[9]This reaction has been studied in different forward angles in an attempt to distinguish among different spin assignment possibilities for important states.

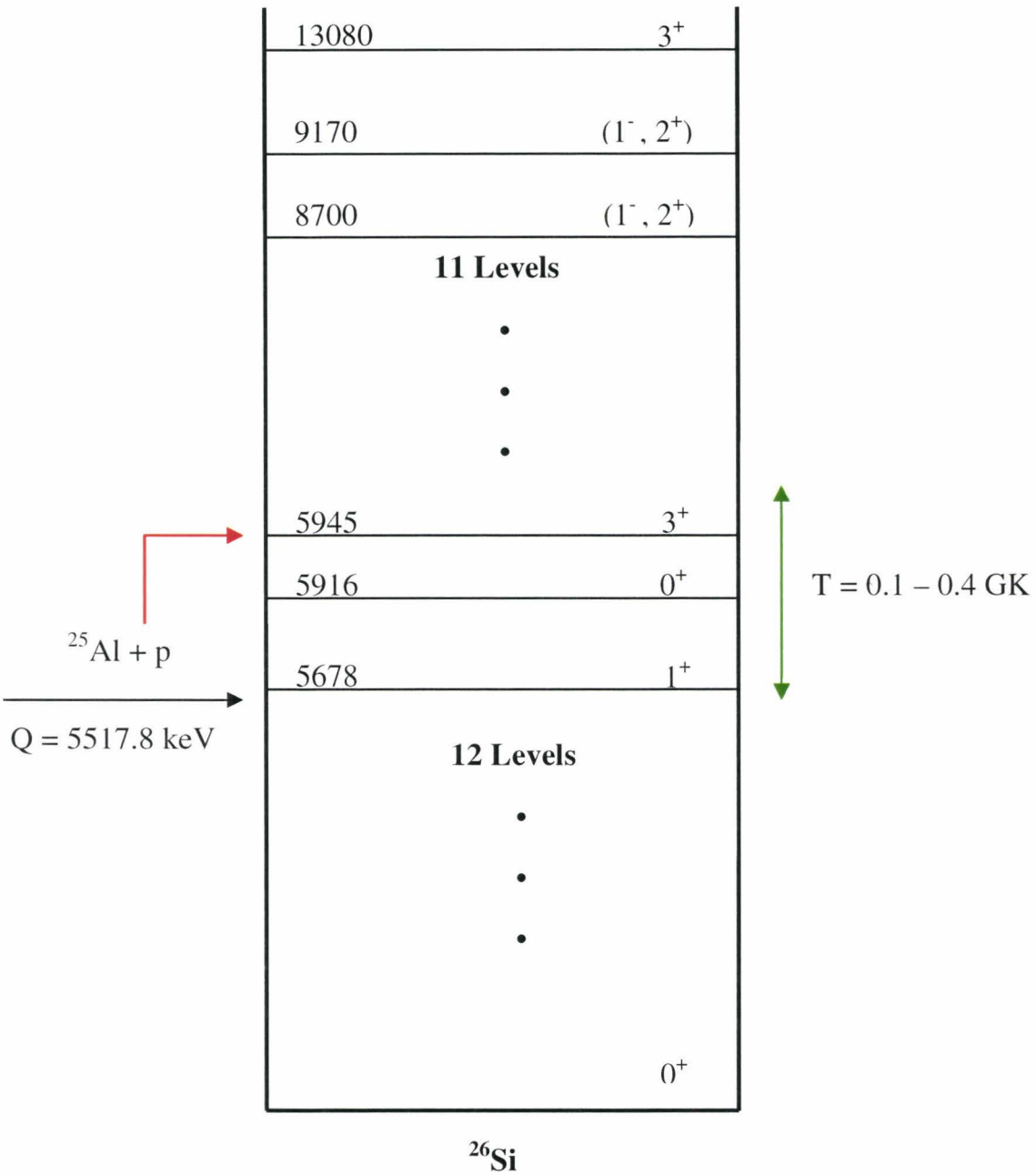

Figure 4.2: The level scheme of ^{26}Si. The energy region of importance at nova temperatures is indicated. For simplicity not all the levels are shown. The proton threshold is from Ref. [121]. The energy levels and spin and parities are based on Ref. [113]. The higher energy levels (from 8 MeV up to 13 MeV) and their properties are from the National Nuclear Data Center (Ref. [123]).

Table 4.1: A comparison of the excitation energies (in MeV) and J^π values of ^{26}Si states from different tabulated values in the literature.

^{29}Si(^{3}He,^{6}He)^{26}Si [a]		^{28}Si(p,t)^{26}Si [b]		^{24}Mg(^{3}He,n)^{26}Si [c]		^{16}O(^{12}C,2n)^{26}Si [d]	
E_x	J^π	E_x	J^π	E_x	J^π	E_x	J^π
0.0	0^+	0.0	0^+	0.0	0^+	-	-
1.7959	2^+	1.7959(11)[e]	2^+	1.7959	2^+	1.7973(1)	2^+
2.7835	2^+	2.790(12)	2^+	2.7835	2^+	2.7864(2)	2^+
3.3325	0^+	3.3339(19)	0^+	3.332	0^+	3.3364(6)	0^+
3.756	3^+	3.760(30)	3^+	3.756	-	3.7569(2)	3^+
4.138	2^+	4.155(2)	$2^+ + 3^+$	4.138(4)	2^+	4.1393(7)	2^+
4.183	3^+	-	-	4.183(4)	3^+	4.1871(3)	3^+
4.446	$2^+ + 4^+$	4.457(13)	$2^+ + 4^+$	4.446	2^+	4.4462(4)	4^+
4.806	$0^+ + 2^+ + 4^+$	4.821(13)	$0^+ + 2^+ + 4^+$	4.806	2^+	4.7985(5)	4^+
-	-	-	-	-	-	48107(6)	2^+
-	-	-	-	-	-	4.8314(10)	0^+
5.145	2^+	5.145(2)	2^+	5.145	2^+	5.1467(9)	2^+

[a]Ref. [113]
[b]Ref. [122]
[c]Ref. [117]
[d]Ref. [121]
[e]The numbers in parenthesis show the uncertainty range in the last digits.

Table 4.2: Continuation of Table 4.1

^{29}Si(^{3}He,^{6}He)^{26}Si [a]		^{28}Si(p,t)^{26}Si [b]		^{24}Mg(^{3}He,n)^{26}Si [c]		^{28}Si(p,t)^{26}Si [d]		^{16}O(^{12}C,2n)^{26}Si [e]	
E_x	J^π	E_x	J^π	E_x	J^π	E_x	J^π	E_x	J^π
5.291	4^+	5.291(3)	4^+	5.291(4)	4^+	-	-	5.2882(5)	4^+
5.518	4^+	5.515(5)	4^+	5.515(4)	4^+	-	-	5.5172(5)	4^+
5.678	1^+	-	-	5.670(4)	1^+	5.673(4)	-	5.6770(17)	1^+
5.916	0^+	5.916(2)	0^+	5.912(4)	3^+	5.914(2)	-	-	-
5.945	3^+	-	-	5.946(4)	0^+	5.946(4)	-	-	-
-	-	6.300(4)	-	6.312(4)	2^+	-	-	-	-
-	-	6.380(4)	-	6.388(4)	2^+	-	-	-	-
-	-	-	-	6.471(4)	0^+	-	-	-	-
-	-	6.787(4)	3^-	6.788(4)	3^-	-	-	-	-
-	-	7.019(10)	-	-	-	-	-	-	-
-	-	7.160(5)	2^+	7.152(4)	2^+	-	-	-	-
-	-	7.425(7)	-	7.425(4)	0^+	-	-	-	-
-	-	7.498(4)	2^+	7.493(4)	2^+	-	-	-	-
-	-	7.678(22)	3^-	7.694(4)	3^-	-	-	-	-
-	-	7.900(22)	1^-	7.899(4)	1^-	-	-	-	-

[a]Ref. [113]
[b]Ref. [122]
[c]Ref. [117]
[d]Ref. [114]
[e]Ref. [121]

As can be seen from Table 4.1, two new states were found by Caggiano *et al.* [113] at $E_x = 5.678(8)$ MeV and $E_x = 5.945(8)$ MeV and a tentative assignment of the 3^+ state was made to $E_x(^{26}\text{Si}) = 5.945$ MeV, $E_r = 427$ keV [119]. This 3^+ state is expected to be the dominant resonance for the $^{25}\text{Al}(\text{p},\gamma)^{26}\text{Si}$ reaction rate, and its corresponding resonance energy is a source of controversy. Parpottas *et al.* [117] confirmed the excitation energies measured by Caggiano *et al.* but disagreed with their spin-parity assignments. They suggested that the 3^+ state is located at $E_x = 5.916$ MeV instead. A very recent study [114] via the (p,t) transfer mechanism has supported that the 3^+ state is located at $E_x = 5.914(2)$ MeV, which is in favor of the measurement by Parpottas *et al.* However, this puzzle has yet to be resolved. Therefore, further study of the structure of ^{26}Si by alternate reaction mechanism is warranted.

4.4.2 Recent Measurements of the ^{30}S Level Structure

^{30}S is unstable and its ground state β^+-decays in 1.178 s to ^{30}P [124]. In previous years, many groups have studied the level structure of ^{30}S via different methods. For example, Paddock *et al.* [125] via the $^{32}\text{S}(\text{p,t})^{30}\text{S}$ reaction; Caraça *et al.* [126] via the $^{28}\text{S}(^3\text{He},\text{n}\gamma)^{30}\text{S}$ reaction; Kuhlmann *et al.* [127] via the $^{28}\text{S}(^3\text{He},\text{n}\gamma)^{30}\text{S}$ reaction; Yokata *et al.* [128] via the $^{28}\text{Si}(^3\text{He},\text{n})^{30}\text{S}(\text{p})$ reaction sequence; and Fynbo *et al.* [129] via the $^{31}\text{Ar}(\beta^+)^{31}\text{Cl}(\text{p})^{30}\text{S}(\text{p})$ decay sequence. As a result of all these measurements, many states have been found and spins and parities have been assigned to them (for more information, see Table I in Ref. [104]). But in general, there are many states whose properties are still unknown.

Fig. 4.3 shows the level scheme of ^{30}S based on the most recent measurement by Bardayan *et al.* [104]. By inspecting the structure of ^{30}Si which is the mirror nucleus for ^{30}S, Iliadis *et al.* [130] concluded that at nova temperatures, the $^{29}\text{P}(\text{p},\gamma)^{30}\text{S}$ reaction rate is dominated by low-energy 3^+ and 2^+ resonances in ^{30}S above the proton threshold at $E_x = 4400$ keV [104]. From the isobaric multiplet mass equation [130], the resonance energies corresponding to the 3^+ and 2^+ states were estimated to be 4733±40 and 4888±40 keV, respectively. Although many people have tried, these two states have never been observed until recently [104]. Bardayan *et al.* [104] have studied the structure of ^{30}S via the $^{32}\text{S}(\text{p,t})^{30}\text{S}$ reaction at the ORNL

Holifield Radioactive Ion Beam Facility[10], and have observed 13 levels, 9 of which are above the proton threshold. One of such states is a new level at 4704±5 keV. They have concluded that this state is more likely the previously unobserved 3^+ state. The ^{29}P(p,γ)^{30}S reaction rate has also been reevaluated using the updated resonance energy (4704±5 keV instead of 4733±40 keV) and an updated proton width (2.8×10^{-5} eV instead of 9.1×10^{-5} eV [130]) for the 3^+ state, and thus the new rate is larger than that calculated by Iliadis *et al.* by as much as a factor of 6 at 0.1 GK [104].

Another group (Galaviz *et al.* [109]) at the NSCL[11] has recently studied the level structure of ^{30}S via neutron removal from a radioactive ^{31}S beam using a polypropylene target[12]. Thus, they have populated the excited states of ^{30}S, which will then γ-decay to the ground state. By studying the Doppler-corrected γ-rays, measured in coincidence with the identified ^{30}S nuclei, they are able to study the level structure of ^{30}S. Further analysis of all the γ-rays by this group is still ongoing. It is crucial to confirm whether the new level observed by Bardayan *et al.* is indeed the missing 3^+ state.

In 1993 and 1999, Hahn *et al.* [131, 132] and Chen *et al.* [5] at Yale University successfully determined the nuclear structure of ^{18}Ne and ^{22}Mg via the (^{12}C,^{6}He) reaction mechanism, respectively. In this thesis, we aim to investigate whether it is possible to study the structure of ^{26}Si and ^{30}S by the same mechanism. Most of the previous experimental studies of ^{26}Si and ^{30}S were done using the (^{3}He,n) or (p,t) reaction mechanism, both of which are dominated by the nucleon transfer mechanism. These latter reaction mechanisms preferentially only populate natural-parity states in ^{26}Si and ^{30}S. However, the (^{12}C,^{6}He) reaction mechanism proceeds by a compound nuclear mechanism [132], and can populate all the states but the $J^\pi = 0^-$ states in ^{26}Si and ^{30}S. If it turns out that the (^{12}C,^{6}He) reaction mechanism for studying the ^{30}S structure is promising, then it can be tried later on to confirm the properties of the 3^+ state obtained by Bardayan *et al.*, and to search for new states.

In the next chapter, we will discuss the apparatus used to carry out our

[10]Oak Ridge National Laboratory, Tennessee.

[11]National Superconducting Cyclotron Laboratory at Michigan State University.

[12]Neutron-knockout on ^{12}C: ^{31}S(^{12}C,^{12}Cn)^{30}S; and on ^{1}H: ^{31}S(p,d)^{30}S in the polypropylene target. Note that both these reactions populate excited states of ^{30}S, which will then γ-decay to the ground state.

experiments at Yale University.

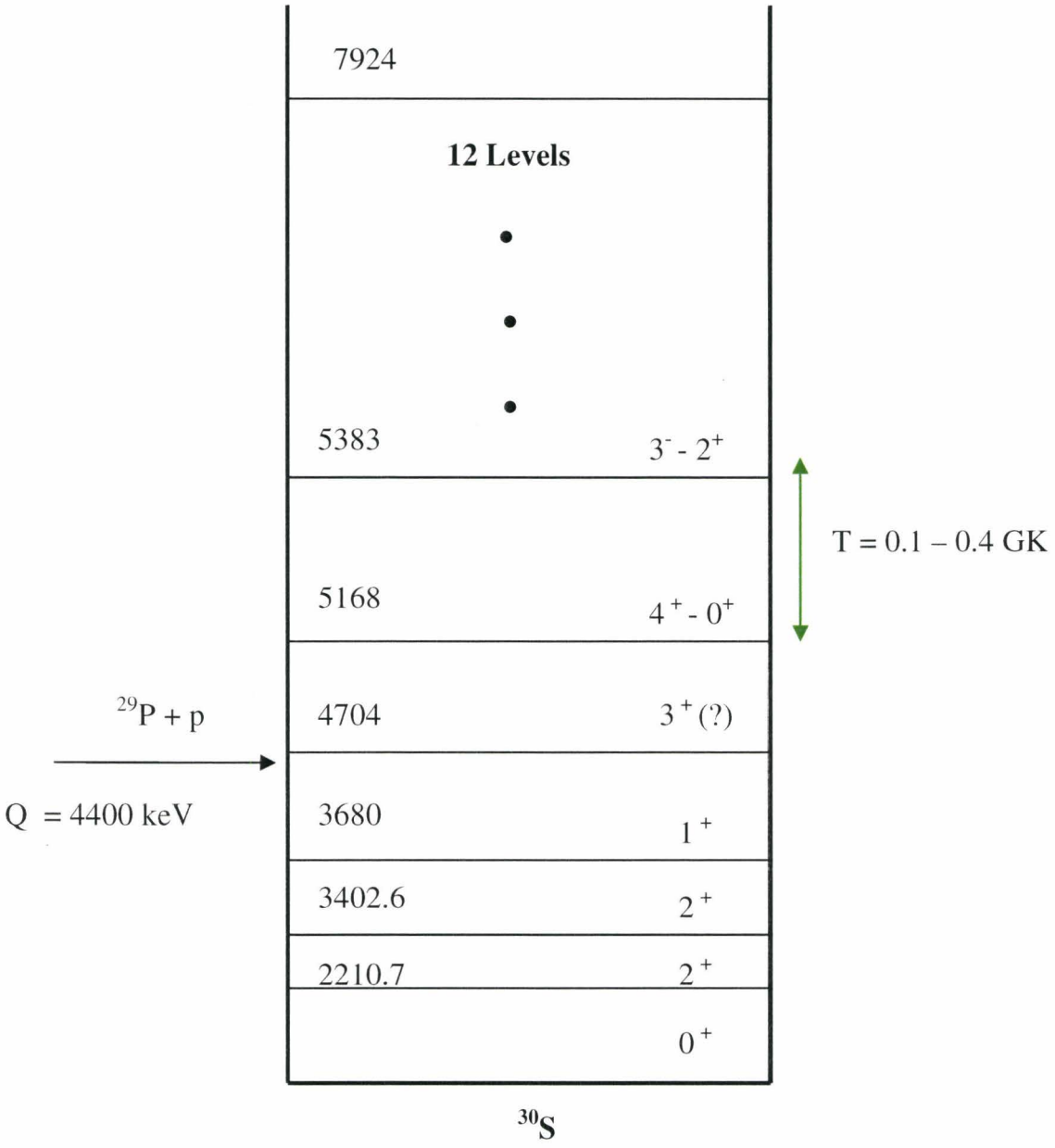

Figure 4.3: The level scheme of ^{30}S. The energy region of importance at nova temperatures is indicated. For simplicity not all the levels are shown. The proton threshold is from Ref. [104]. The energy levels and spin and parities are from Ref. [104]. The energy levels higher than 7100 keV are from Ref. [129]).

Chapter 5

Experimental Details

We have carried out test experiments to investigate the ^{20}Ne(^{12}C,^{6}He)^{26}Si and the ^{24}Mg(^{12}C,^{6}He)^{30}S reactions at Yale University. For these "heavy ion reactions", which proceed by a compound nuclear mechanism, we have employed stable carbon and magnesium beams, impinging on neon and carbon targets, respectively; and have studied the nuclei that are produced in the reactions. In the following sections, we describe the experimental apparatus used for our experiment.

5.1 The Yale ESTU Tandem Van de Graaff Accelerator

The Wright Nuclear Structure Laboratory (WNSL) at Yale University (Fig. 5.1), where we did our experiment, operates the largest electrostatic Tandem accelerator in the world. The Extended Stretched TransUranium (ESTU) Tandem Van de Graaff accelerator at Yale is 98 feet long and 25 feet in diameter, that consists of a large central terminal, which has five high voltage modules on each side. Each of those high voltage modules is 8 feet long. It utilizes pure SF_6 as an insulating gas, and operates at voltages up to 22 MV [133].

This accelerator uses a sputter ion source to produce negative ions to be injected in to the accelerator. In 1993, a new 300 kV negative ion injector was mounted [134] on a pre-accelerating platform, which can accelerate the beam to energies up to 200 keV [135]. This injector contains a double focusing, multi-pole

corrected 90-degree bending magnet [134], and is able to inject beams with all masses from 1 to 250 with a mass resolution of 1/200 and intensities up to 20 microamps [135] from the pre-accelerating platform to the Tandem accelerator. The negative ions are then sent through a stripper foil (located before the analyzing magnet, see Fig 5.1), where some electrons are knocked off from the ions, thus producing a positively charged ion.

After the beam traverses the accelerator, it enters an analyzing magnet, which determines the purity and energy of the beam. The analyzing magnet bends the beam of charge q, mass m and energy E through a ± 0.5 mm aperture and through a central bending radius $\rho = 1.79$ m according to [112]:

$$\rho = \frac{P}{qB} = \frac{\sqrt{2mE}}{qB} \tag{5.1}$$

where P is the momentum of the particles, and B is the magnetic field of the analyzing magnet. Only those particles can pass the analyzing magnet that have the correct ρ; and thus, the selected beam will be monoenergetic. The analyzing magnet have been calibrated by a well-known ^{12}C + p elastic scattering resonance at $E_p = 14.231$ MeV [112, 136] at the level of accuracy of $\sim 1/10^4$ [112]. The beam is then directed to the target room by using magnets in the accelerator vault.

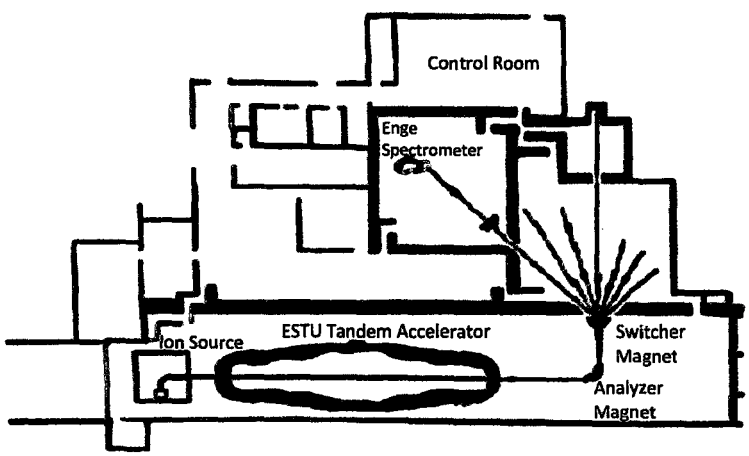

Figure 5.1: Schematic diagram of the top view of the WNSL layout. Figure is adopted from Ref. [137].

5.2 Beams and Targets

For the ^{20}Ne(^{12}C,^{6}He)^{26}Si experiment, we used a ^{12}C beam, which was produced by sputtering a graphite sample packed in a copper cone with energetic Cs ions in the ion-source to produce $^{12}C^{-}$ ions. These negatively charged ions were then injected and accelerated to the tandem terminal held at $\sim$ 13.33 MV. Then, they were stripped of electrons by a carbon foil to become positive ions. The charge state of the ^{12}C beam used in the ^{20}Ne(^{12}C,^{6}He)^{26}Si experiment was 5^{+}. These positive ions were further accelerated back to the ground potential, obtaining the final energy of 80 MeV. The ^{12}C beam energy was decided upon considering that it must be high enough to overcome the Q-value and the Coulomb barrier of the ^{20}Ne(^{12}C,^{6}He)^{26}Si reaction, which are -17.49 MeV and 13.81 MeV, respectively, as well as to populate the states in ^{26}Si up to excitation energies of 12 MeV. We ran our experiments with ^{12}C beam currents of about 100 - 200 enA.

The ^{12}C beam was finally directed to the target room, where it bombarded one of a natural carbon of thicknesses 91.8 μg/cm^2, a ^{13}C target of thicknesses 103.8 μg/cm^2 or an implanted ^{20}Ne target with the thickness of 7$\pm$1 μg/cm^2 of ^{20}Ne implanted in 40 μg/cm^2 of carbon at a time. The natural carbon target was used to check whether the experimental setup was such that we could detect ^{6}He particles. Using the ^{12}C(^{12}C,^{6}He)^{18}Ne reaction, the Coulomb barrier for this reaction is much lower (9.06 MeV), and thus it has a higher yield. The ^{13}C target was used to check for contaminant ^{6}He ions from the ^{13}C(^{12}C,^{6}He)^{19}Ne reaction.

For the ^{12}C(^{24}Mg,^{6}He)^{30}S experiment, we first tried using a ^{12}C beam[1]; however, our first measurement (see Chapter 6) showed that the ^{24}Mg target was significantly oxidized, and thus we changed the beam to ^{24}Mg and the target to natural carbon to avoid the contaminants coming from the ^{16}O(^{12}C,^{6}He)^{22}Mg reaction. With the natural carbon target and ^{24}Mg beam, the ^{12}C(^{24}Mg,^{6}He)^{30}S reaction resulted to obtain a cleaner spectrum (see Chapter 6).

To produce the ^{24}Mg beam, we used a sample of magnesium ammonium packed in a copper cone. Thus, $^{24}MgH^{-}$ ions were produced[2]. The source should

[1]The ^{12}C beam bombarded a ^{24}Mg target of thickness of 319.5 μg/cm^2 on 11.1 μg/cm^2 of carbon backing, but due to the contaminants, we decided to interchange the target and the beam

[2]Magnesium has a negative electron affinity, and thus it will not form a metastable negative ion with a significant lifetime. So, it is necessary to accelerate a molecule, instead.

be well cooled to avoid the decomposition of magnesium hydride. These negatively charged ions were accelerated with the tandem accelerator (11.25 MV terminal voltage). The magnesium hydride molecules are then broken off by a carbon foil; moreover, they were stripped of electrons by the foil to become positive ions. Thus, we acquired a pure ^{24}Mg beam with a charge state of 7^+, which was further accelerated back to the ground potential, to obtain the final energy of 90 MeV. The ^{24}Mg beam energy was decided upon considering that it must be high enough to overcome the Q-value and the Coulomb barrier of the ^{12}C(^{24}Mg,^{6}He)^{30}S reaction, which are -17.47 MeV and 16.03 MeV, respectively, and to populate the states in ^{30}S up to excitation energies of 8 MeV. The ^{24}Mg beam current was between 70 - 200 enA.

In the target room, the ^{24}Mg beam impinged on the 91.8 μg/cm^2 natural carbon and 103.8 μg/cm^2 ^{13}C targets. The ^{13}C target was used to find the ^{6}He particle group. The Q-value of the ^{13}C(^{24}Mg,^{6}He)^{31}S reaction is -9.36 MeV and the Coulomb barrier is 15.8 MeV. Thus, the latter reaction has higher cross section; and as a result, the ^{6}He particle groups were more easily identified, and we could set the gates around them (see Chapter 6). Thus, when we switched back to the natural carbon target, the gates were already set.

The target thicknesses were found by measuring the energy loss of 5.4854 MeV α-particles from a ^{241}Am source in the target using a silicon surface barrier detector. In the next chapter, we will discuss more about the analysis and the results of our experiments.

5.3 The Yale Split-Pole Magnetic Spectrograph

The Enge spectrograph was originally designed by Enge [138] in 1967 to maximize the ion collecting power without sacrificing the energy resolution. As its name ("split-pole") indicates, the spectrograph consists of two pole pieces (see Fig. 5.2) surround by a single coil [138]. The precise measurement of the momenta of charged particles and the population of excited states of nuclei in the beam induced nuclear reactions is determined by Enge spectrograph [138]. The Enge spectrograph also focuses the particles emerging from the target vertically and horizontally to a position along the focal plane, which is determined by the particle's momentum, charge and the

spectrograph's magnetic field. Due to the shapes of the edges of its poles and the locations of the pieces within the coil, the vertical and the horizontal focusing up to the second order is achieved for particles from the same reaction channel that have slightly different momenta and are emitted in slightly different directions from the target.

The Enge spectrograph can accept all reaction products, whose radii of curvature, ρ, lie between 51.1 cm to 92.0 cm (see equation (5.1)) as they are traversing the magnetic field of the spectrograph. Its maximum angular acceptance is $\Delta\Theta$ (horizontal)= $\pm$ 80 mrad and $\Delta\Phi$ (vertical)= $\pm$ 40 mrad[3], for a total solid angle of 12.8 msr at its entrance [137]. Such angular acceptances are provided by a set of slits located at the entrance of the magnet. In our experiment, the reaction products were measured at lab angle of 5 degrees. For the ^{20}Ne(^{12}C,^{6}He)^{26}Si experiment, the horizontal and vertical slits were set at $\pm$10 and $\pm$40 mrad, respectively. Thus, the resultant solid angles was 1.6 msr. For the ^{24}Mg(^{12}C,^{6}He)^{30}S experiment, they were each set at $\pm$40 mrad resulting in a solid angle of 6.4 msr.

The target spot is determined by tuning the beam through a 2 mm diameter collimator placed at the target position into a Faraday cup [112].

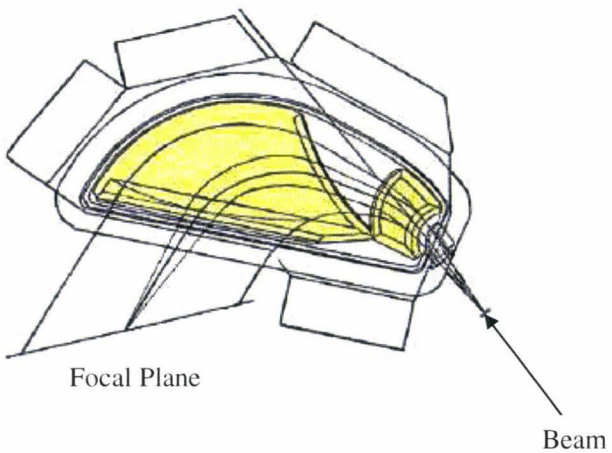

Figure 5.2: Schematic diagram of the Enge split-pole spectrograph adopted from Ref. [112]. The angles through which the particles enter the spectrograph and the energies of the particles determine their trajectories. The yellow regions are the pole pieces.

[3] θ and ϕ refer to angles in the plane of and normal to the plane of the particle trajectory in the spectrograph, respectively [112].

5.4 The Focal Plane Detector

The focal plane detector as shown in Fig. 5.3 is a position-sensitive ionization drift chamber (hereafter PIDC), the volume of which is filled with isobutane gas (C_4H_{10}) through gas ports installed in the sides of the chamber. The chamber is a milled-out block of aluminium, $26 \times 8.5 \times 3$ inches in length, height and depth [5]. Reaction products bent by the spectrograph enter and exit the detector through 0.25 mil[4] aluminized mylar windows attached to the window plates [5]. This detector is set at the focal plane of the spectrograph, and all particles, whose radii of curvature lie between 70 cm and 86 cm reach the focal plane.

As different species drift across a cathode, depending on their mass, they lose different amount of energy. Moreover, based on their momentum, their position along the focal plane will be different. These two characteristics (energy loss (ΔE) and momentum) are measured by the focal plane detector. The entire active region of the detector is covered by the cathode, which is held at large negative potential [5]. At the top of the detector there are a set of Frisch grid which is grounded; and the three high-voltage wires of each position sensitive assembly (PSA), which are held at large positive potential [5]. A plastic scintillator is put at the end window of the focal plane detector to measure the residual energy (E) of particles that exit the PIDC.

When the charged particles traverse the isobutane gas inside the chamber between the Frisch grid and the cathode, they ionize the gas. Thus, the electron-ion pairs will be created. In that region, there are 10 equally spaced wires, which are biased and are connected to the cathode and the Frisch grid through a resistor chain (each of 10 MΩ) [5]. These wires produce and shape a uniform electric field, which drifts the electrons toward the positively biased high-voltage wires through the Frisch grid, where they cause an electron avalanche.

The delay line method is used to find the position of particle groups along the length of the PIDC. The two PSAs at the top of the detector are identical and they each consists of a circuit board. The board in the plane of the cathode plate has 220 lead-coated copper pick-up pads tilted at 45 °on its underside, so that the pads lie

[4]mil also known as thou is a unit length equal to 0.001 inches.

along the direction of reaction products [112]. The pick-up pads pick up the image charge of the avalanche of the electrons. The other board, which is in the plane parallel to the windows, holds the delay chips. Each assembly has twenty-two 50 ns delay chips that are connected to the pick-up pads [112]. The true delays of these chips have been measured to lie between 63 - 65 ns for the chips in the upstream (or "front") PSA, and 60 - 62 ns for the downstream (or "rear") PSA [112].

The current pulse from the pick-up pads travels through this delay line to both ends of the PSAs. The time differences between a particles' signals at each end of a delay line is sent to a time-to-amplitude converter (TAC) to determine the "front" and "rear" positions of the particle passing through the detector [112].

Downstream of the exit window of the PIDC, light is collected by two photo-multiplier tubes (PMTs) at each end of the scintillator. Thus, there are two signals E_1 and E_2 produced. The software then combines these signals according to the following equation to produce an energy signal [112, 139]:

$$E = \sqrt{E_1 E_2} \tag{5.2}$$

With measurements of ρ, E and ΔE, this detector can identify the reaction products quite effectively.

To obtain a better energy resolution, the position of the focal plane detector should be adjusted for each reaction. This position is related to a factor called the kinematic parameter given by [112]:

$$k \equiv \frac{-1}{p}\frac{dp}{d\theta} = \frac{\partial(\ln p)}{\partial\theta} \tag{5.3}$$

where p is the particle momentum, and θ is the lab angle in radians. This factor can be calculated by a kinematics computation program called JRelKin. Once we obtain the kinematic parameter for our specific reaction, the detector position is a dimensionless number that can be calculated by [112]:

$$Z = 56.7k + 55.5 \tag{5.4}$$

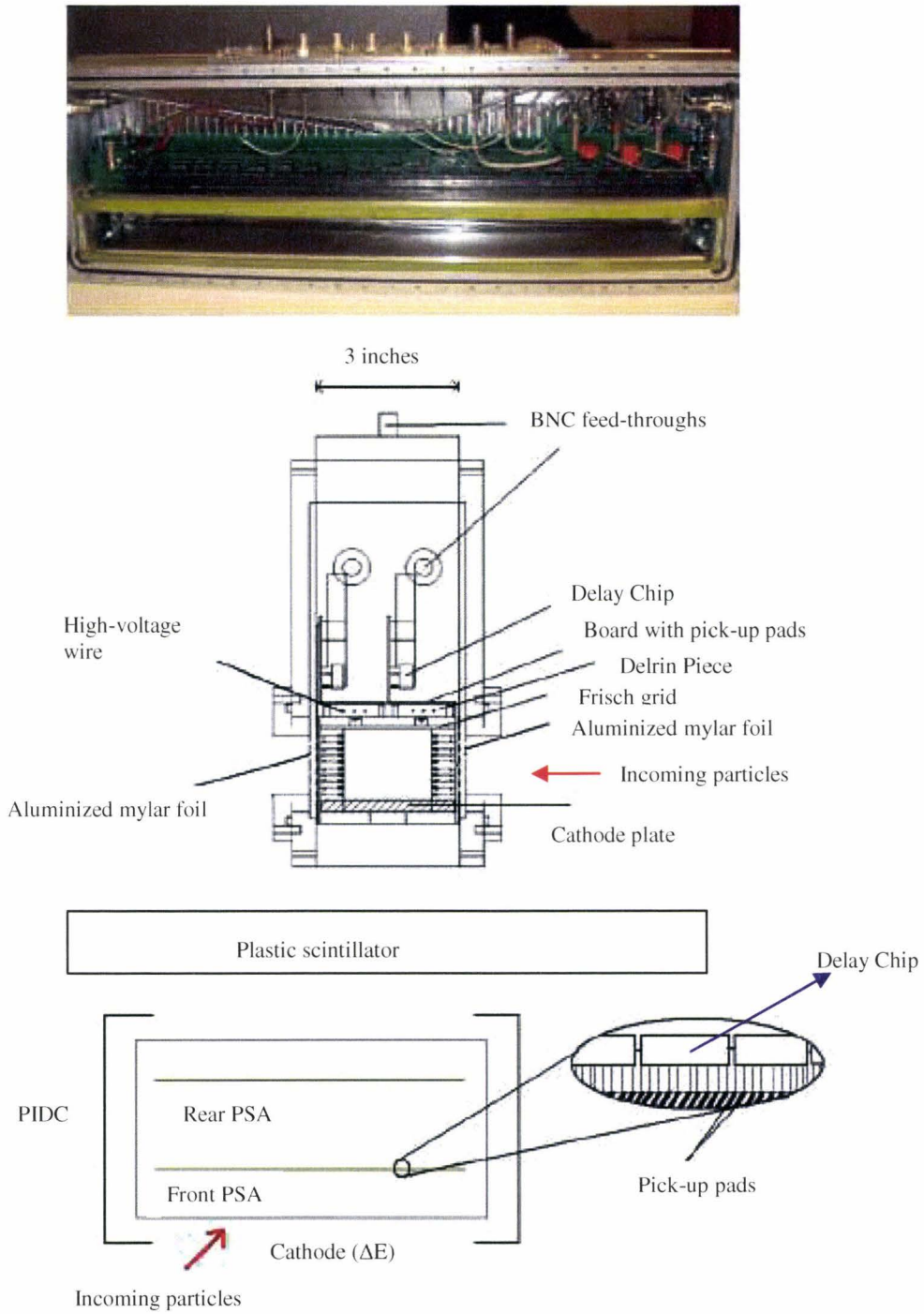

Figure 5.3: (top) A picture of the interior of the position-sensitive ionization drift chamber, looking from the front. (middle) Schematic side-view of the PIDC, to scale. For simplicity, the field-shaping wires are not shown. (bottom) Simplified schematic top-view of the focal plane detection system (not to scale). The diagram is adopted from Ref. [5].

5.5 Electronics

There are signals produced by the two ends of the front and rear wires, which construct the delay-line signals from the cathode. Another set of signals are produced by the two photomultiplier tubes at either end of the scintillator. This latter set of signals from the scintillator signal. Both sets of signals are then processed by the (NIM-standard) electronics shown schematically in Fig. 5.4 [112]. The delay-line signals are amplified by fast preamplifiers and are further amplified and shaped to optimize timing resolution by timing filter amplifiers. A constant fraction discriminator is used to eliminate noise from the wire signals and to produce a logic pulse [5]. The scintillator signals are also amplified and then summed. The trigger for our events was determined by the cathode. The various signals reach the ADC (32-channel VME-6U module CAEN V785), where they get delayed such that they fall within the gate determined by the cathode signal [5].

5.6 The Data Acquisition System

The data acquisition software that was used for the data analysis is a java-based software called Jam which is run on a PC. This PC is connected to another computer which runs the Vx-Works operating system by a private Ethernet. The data from the ADC and TDC is transferred to the latter computer and is saved in an 8 kB memory buffer.

Jam is a simple graphical user interface that takes a program called the sort routine as an input, which can be written by the experimenter. Jam can save the online data[5] into the event files[6] that can be later used again for offline analysis; with the help of the sort routine, it can sort those event files into 1-D and 2-D histograms [112]; it provides us with the information about the peaks that corresponds to the excited states of nuclei, e.g. the centroid of the peak, the area under the peak, the channel number, etc.; Jam also provides a fitting program with which one can fit the peaks with a gaussian function to find its energy; moreover, it can interact

[5]Online is when the data is collected during the experiment and offline is after the experiment is done.

[6]The data are saved in a binary file with the .evn extension. These files are called event files.

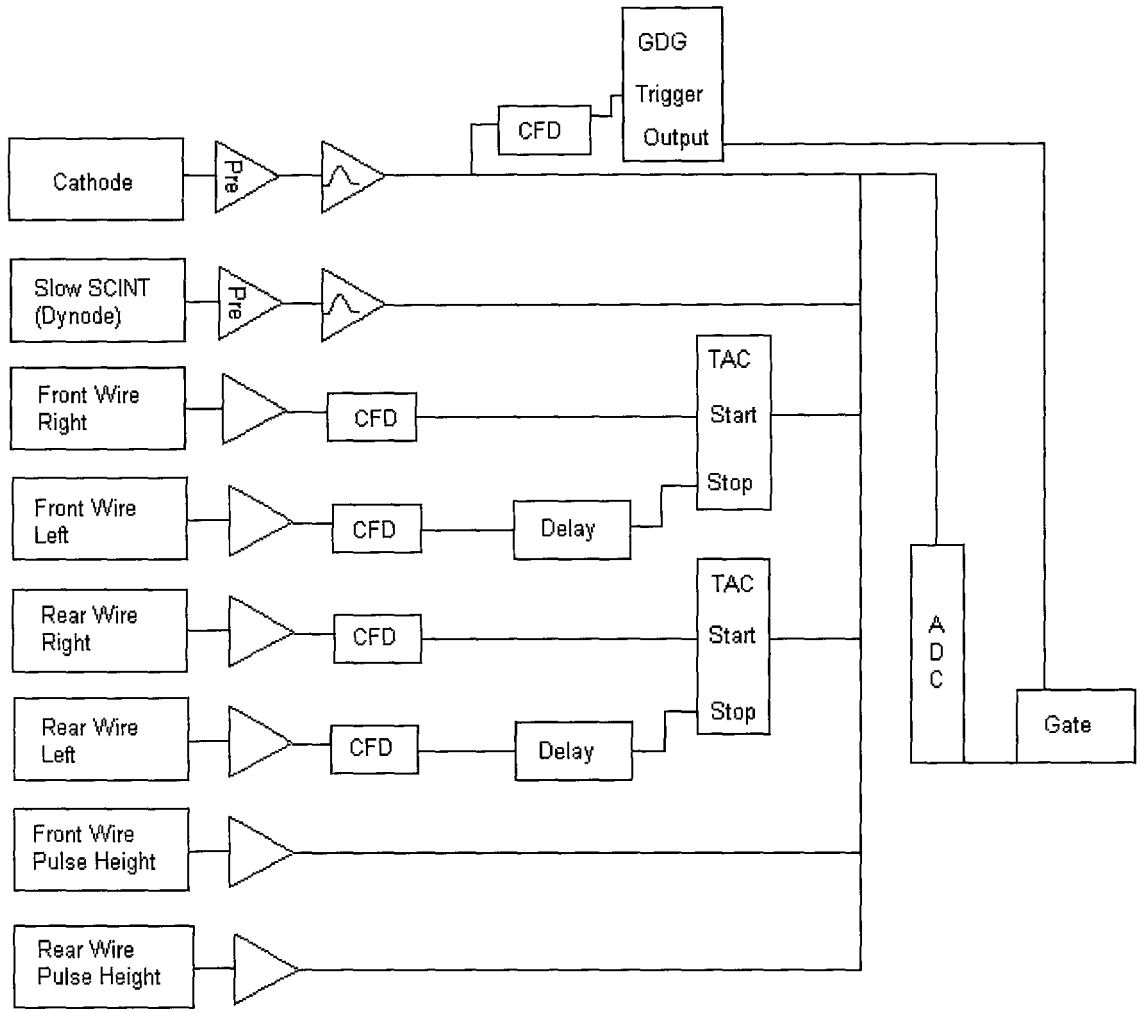

Figure 5.4: The schematic diagram of the electronics used in our experiment. Abbreviation: SCINT: scintillator, CFD: constant-fraction discriminator, ADC: analog-to-digital converter, TAC: time-to-amplitude convertor, and GDG: gate-and-delay generator. The triangular shapes are the amplifiers, two of which that contain the prefix "pre" are preamplifier, and those that have a wave inside are the shaping amplifiers.

with the VME computer to retrieve scaler information during runs, from which the experimenter can be informed of the beam current and the cathode and scintillator rates, etc., and this data can also be saved [137].

The sorting procedure depend on the gates that can be drawn by the experimenter to select particle groups of interest; based on these gates, other histograms can then be generated [112]. The gates can be redrawn as many times as one wants, and each time, Jam sorts the data with the new gates. All histograms and gates information for a particular run can be saved to a file separate from that containing

the raw data[7] [112]. In the next chapter, we will present the analysis and the results of our experiments.

[7]The files that contain the gate information are saved with .hdf extension

Chapter 6

Analysis and Results

In this chapter, we will discuss a number of different experiments that were performed in the Wright Nuclear Structure Laboratory of Yale University, and will present the experimental results. The aim of these experiments was to test whether it is feasible to study the nuclear structure of ^{26}Si and ^{30}S via the ^{20}Ne(^{12}C,^{6}He)^{26}Si and ^{12}C(^{24}Mg,^{6}He)^{30}S reactions, respectively. Before we consider the results, we will discuss the techniques used to identify the various particles, which were present in the raw data of both experiments. We will focus on the ^{12}C(^{12}C,^{6}He)^{18}Ne reaction to explain the general particle identification technique used in all subsequent experiments.

6.1 Particle Identification

Our raw data included different particle groups, e.g. protons, deuterons, tritons, α-particles, ^{6}He, ^{6}Li and ^{7}Li. Each particle produces a characteristic signal in the electronics, e.g. cathode, scintillator, front- and rear-position signals, which correspond to the energy loss of the particles, since they deposit energy in the cathode as they traverse it; the remaining energy of the particles, which is fully deposited in the scintillator where the particles stop; and the position of the particles, respectively.

The particle identification was done by comparing experimental data with a simulation program, called TAJ Simulation, which simulates the location of particles on the focal plane detector. Fig. 6.1 shows an example of the simulations for the

^{12}C(^{12}C,^{6}He)^{18}Ne experiment.

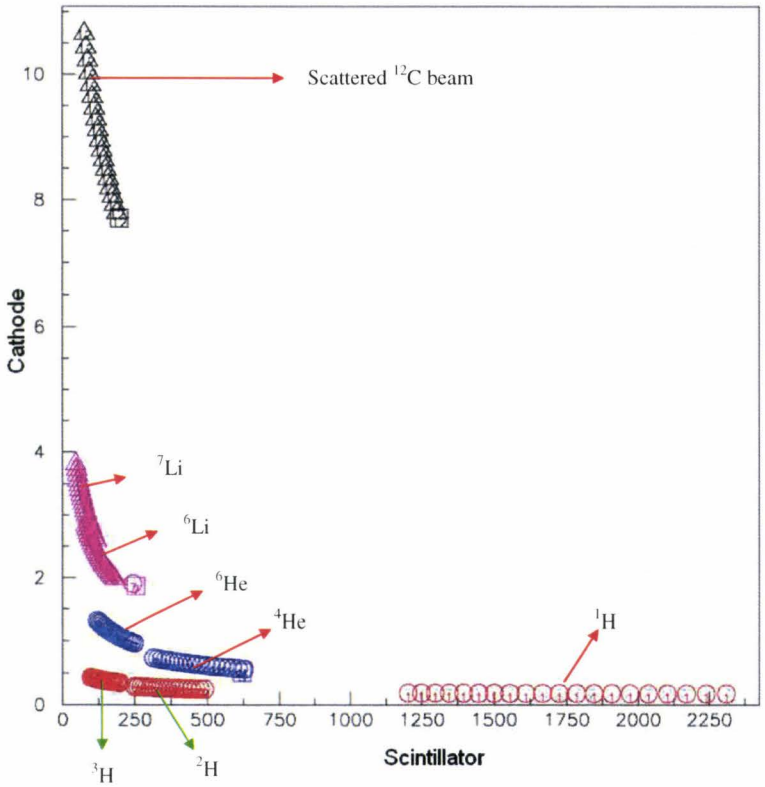

Figure 6.1: Particle simulations for the Cathode vs. Scintillator plot in the ^{12}C(^{12}C,^{6}He)^{18}Ne experiment at $E_{\text{beam}} = 80$ MeV. Different shapes and colors indicate different particle groups. The Cathode vs. Scintillator plot shows different particle groups on a ΔE vs. E graph, where ΔE is the energy loss and E is the residual energy. The lower the particle's mass, the less energy it loses traversing the focal plane detector. In this way, the lighter particles deposit less energy in the cathode and have more residual energy to be deposited in the scintillator. As such, they are seen in the bottom right side of the figure. For the more massive particles, the scenario is reversed. The units on the axes are arbitrary.

By comparing these simulations with the raw data in Cathode vs. Scintillator, Cathode vs. Front Position and Scintillator vs. Front Position 2D-histograms[1] in Jam

[1]The Cathode vs. Scintillator histogram is explained in the caption of Fig. 6.1. The Cathode vs. Front Position histogram is a ΔE vs. P graph, where ΔE is the energy loss and P is the momentum. On this histogram, we will see the lighter particles in the bottom side of the figure. This is because the lighter particles lose less energy, and thus deposit less energy in the cathode. For the heavier particles, the scenario is reversed. The Scintillator vs. Front Position histogram shows different particle groups on a E vs. P graph, where E is the residual energy and P is the momentum. Note that the particles reach the front wire earlier than the rear wire, and due to multiple scattering of the ions in the gas, the resolution of the rear wire is worse. Thus, we consider the histograms that contain the front position signals.

(see Fig. 6.3), the various particle groups are identified. After successful identification of the particle groups of interest, we set a 2D gate around them (see Fig. 6.3) on the Cathode vs. Scintillator, Cathode vs. Front Position and Scintillator vs. Front Position 2D-histograms. These gates separate different particle groups from each other, and they are double-checked by considering the effect of each gate on the other two histograms[2] (see Fig. 6.4) to make sure that the gates include all the events of interest.

Some particles may have scattered from the acceptance slits of the spectrometer or within the spectrometer itself. They are eliminated by drawing a gate around the correlated events on the Rear Position vs. Front Position histogram (see Fig. 6.2), because these particles appear in the Rear vs. Front position histogram as events with no correlation between front and rear positions and as structureless bands to either side of the real events (see Fig. 6.2).

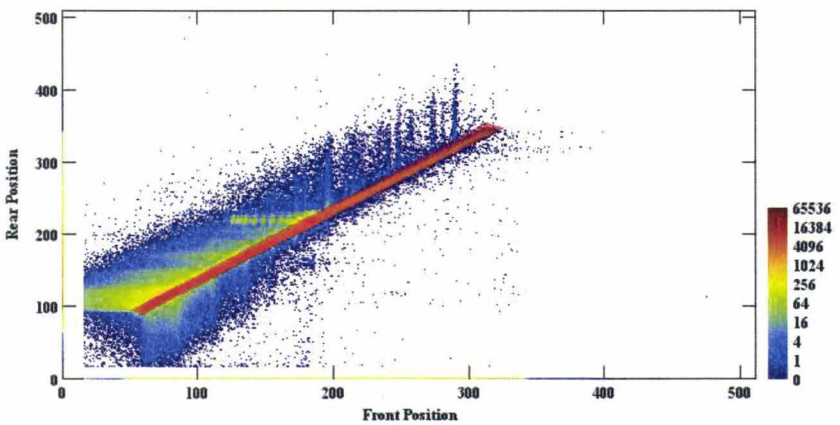

Figure 6.2: The Rear Position vs. Front Position histogram for the ^{12}C(^{12}C,^{6}He)^{18}Ne reaction at beam energy of 80 MeV and $\theta^{\text{lab}} = 5^{\circ}$. This plot shows the positions of all particles along the rear wire with respect to the front wire. The scattered particles are those events for which there is no correlation between the front and rear positions. These events can be disregarded with the application of a gate (the red band) around those events for which the positions along the front and rear wires are correlated. The color code to the right of figure indicates intensity (red is high and blue is low intensity).

[2]The sort routine with which we sorted our data provided us with total of 6 histograms that show the effect of one gate on the other two histograms.

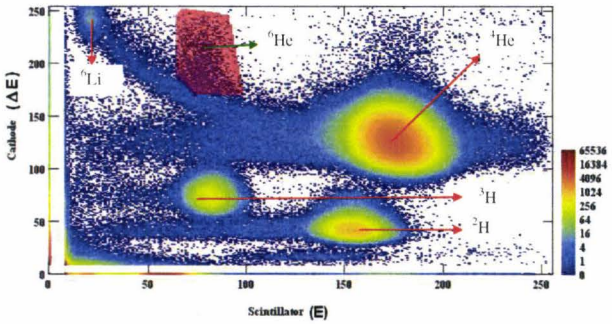

(a) The energy loss of particles in the cathode vs. the residual energy in the scintillator for particles emerging from the natural carbon target at $\theta = 5°$.

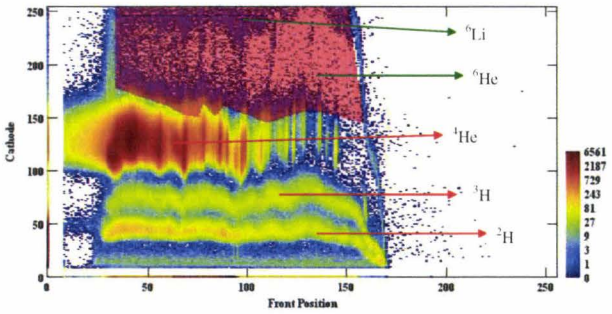

(b) The energy loss of particles in the cathode vs. the front position along the wire at the focal plane detector for particles emerging from the natural carbon target at $\theta = 5°$.

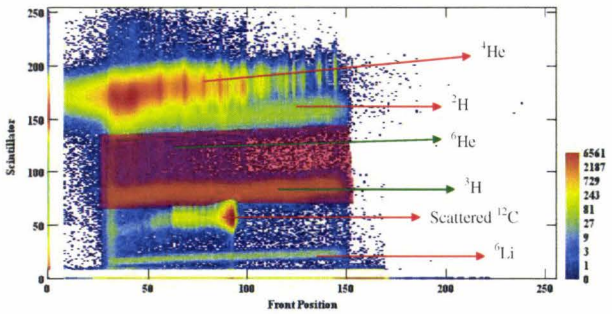

(c) The residual energy of particles in the scintillator vs. the front position along the wire at the focal plane detector for particles emerging from the natural carbon target at $\theta = 5°$.

Figure 6.3: Cathode vs. Scintillator, Cathode vs. Front position and Scintillator vs. Front position 2D histograms for the ^{12}C(^{12}C,^{6}He)^{18}Ne experiment at $E_{\text{beam}} = 80$ MeV. Deuterons, tritons, α-particles, and ^{6}He particles as well as ^{6}Li groups were all present in the raw data and were identified by comparing the above histograms with the simulations. The gates around the ^{6}He groups are shown by a red band. Note that in the cases where some particle groups overlap, the gates may contain some particles which are not of interest, because we prefer to err on the side of caution and not lose any particles of interest. As an example, the gate in Fig. 6.3c includes ^{6}He and tritons (and maybe some deuterons), because of the overlap of the scintillator signals for those ^{6}He and tritons that arrive at the same front position due to the same A/q value (A is the atomic mass and q is the charge). The color code on the right of the figures indicates the intensity (red is higher and blue is lower intensity).

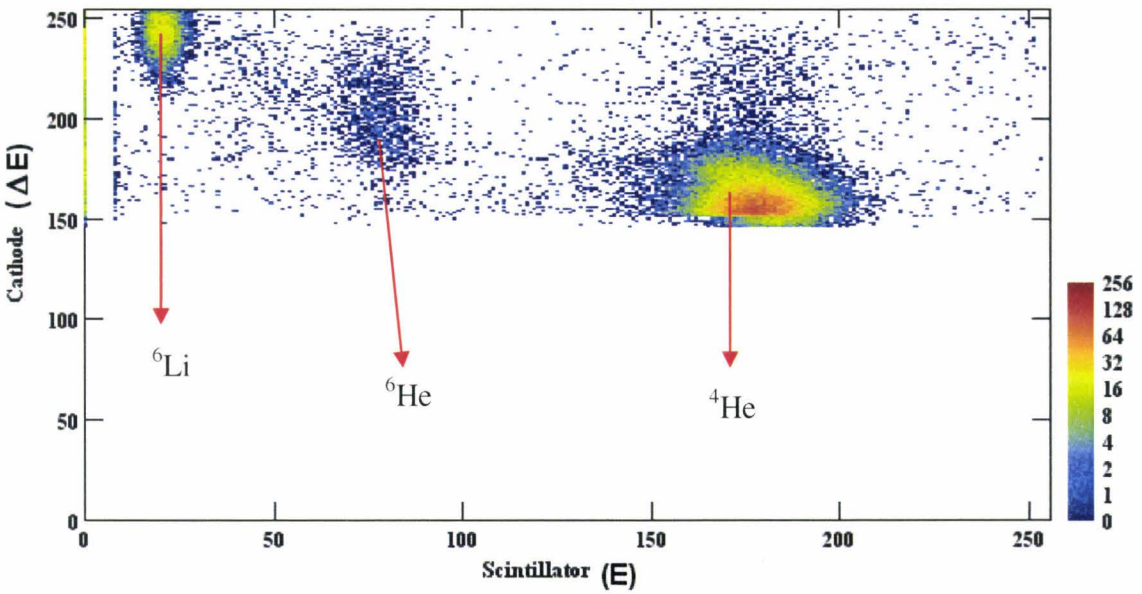

Figure 6.4: In this plot, only those particles that went through the gate shown in Fig. 6.3b (^{6}He particles as well as a small amount of ^{6}Li and α-particles) are plotted on the Scintillator vs. Front Position histogram. Thus, by setting the gate on the Cathode vs. the Front Position histogram, we have been able to eliminate many particle groups (compare this figure with Fig. 6.3b) which are not of interest.

6.2 The ^{20}Ne(^{12}C,^{6}He)^{26}Si Experiment

The Q-value for this reaction is -17.49 MeV, and the Coulomb barrier is approximately 13.81 MeV. In January 2007, the beam energy and other kinematics parameters, e.g. the magnetic field of the spectrometer[3]; relative positions of ^{6}He groups of interest along the focal plane; and the kinematics for contaminant reactions for the ^{20}Ne(^{12}C,^{6}He)^{26}Si experiment were calculated, and a test experiment (lasted approximately 27 hours) was carried out to examine the feasibility of conducting such an experiment. The setup for this test experiment is shown in Table 6.1, where E, P, B, θ, Z, $\Delta\theta$, $\Delta\phi$, V_C and V_{wires} are the beam energy, pressure of the gas inside the focal plane detector, magnetic field of the spectrometer, lab angle, detector position, maximum horizontal acceptance of the spectrometer, maximum vertical acceptance of the spectrometer, voltage across the cathode and voltage across the front and the rear wires, respectively.

Table 6.1: The experimental setup for the ^{20}Ne(^{12}C,^{6}He)^{26}Si test run in January 2007.

E (MeV)	P (Torr)	B (kG)	θ (degrees)	Z	$\Delta\theta$ (mrad)	$\Delta\phi$ (mrad)	V_C (V)	V_{wires} (V)
70	100	13.9938	5	52.8	$\pm$10	$\pm$40	-600	1400

For approximately two-thirds of the run-time, the experiment was done using a 7$\pm$1 μg/cm^2 ^{20}Ne target implanted in approximately 40 μg/cm^2 of carbon. We attempted to detect the ^{6}He particle groups emerging from the target, from which we could then study the excited states of ^{26}Si. In order to detect the ^{6}He groups, we first identified their position along the focal plane using the technique discussed previously. Then, with the application of further gates in different 1D and 2D histograms, the ^{6}He front position spectrum (see Fig. 6.5) that corresponds to the excited states in ^{26}Si was produced. By comparing this spectrum with the expected positions of the

[3]The combination of beam energy and the magnetic field of the spectrometer were calculated in such a way to see most of the excited states of any given nucleus under investigation all across the focal plane between 70 to 86 cm (all particles whose radii of curvature lie between 70 cm and 86 cm reach the focal plane; see Chapter 5), with the proton threshold of that nucleus located approximately in the middle of the focal plane.

excited states of ^{26}Si along the focal plane from the ^{20}Ne(^{12}C,^{6}He)^{26}Si reaction, which is determined by another simulation program called Spec-Plot, we could attempt to identify states in ^{26}Si.

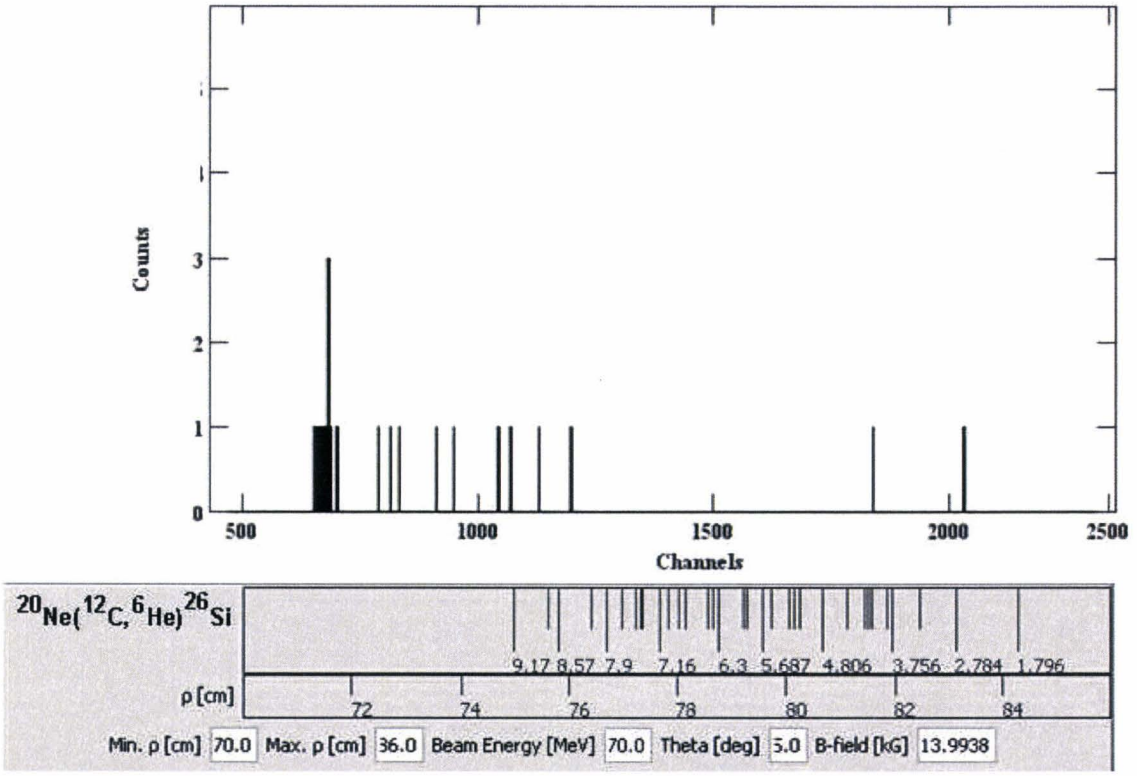

Figure 6.5: (Top) ^{6}He momentum spectrum corresponding to the ^{26}Si states from the ^{20}Ne(^{12}C,^{6}He)^{26}Si reaction at $\theta^{\text{lab}} = 5^{\circ}$ and $E_{\text{beam}} = 70$ MeV. The focal plane starts from channel 500 and ends on channel 2500. (Bottom) The expected positions of the excited states of ^{26}Si from simulation along the focal plane from the ^{20}Ne(^{12}C,^{6}He)^{26}Si reaction at 70 MeV beam energy and $\sim$ 14 kG magnetic field at 5°. ρ on the bottom figure is the radius of the curvature for the trajectories of those particles that reach the focal plane (the minimum and maximum curvatures are 70 cm and 86 cm, respectively). By comparing the states on the top histogram with the lines on the bottom figure (each line represents a state of ^{26}Si on the focal plane; only some of the energies are labeled), we can identify the ^{26}Si states. The vertical and the horizontal axes are counts and channels in arbitrary units, respectively.

As can be seen from Fig. 6.5, we did not see any state of ^{26}Si! Thus, there was something wrong with the ^{20}Ne target. We decided to look for ^{6}He groups from the ^{12}C + ^{12}C reaction. Thus, the rest of the run-time was spent studying the ^{12}C(^{12}C,^{6}He)^{18}Ne reaction, where we changed the ^{20}Ne target to a natural carbon

target of thickness of 91.8 μg/cm^2, and tried to study the ^{12}C(^{12}C,^{6}He)^{18}Ne reaction instead. The experimental setup for this reaction was slightly different from that of the ^{20}Ne(^{12}C,^{6}He)^{26}Si reaction. The beam energy, gas pressure, lab angle, and the maximum horizontal and vertical acceptance did not change. But, the position of the detector and the magnetic field of the spectrometer were changed to 50.6 and 12.055 kG, respectively.

Due to the lower Coulomb barrier (9.06 MeV), the cross section for this reaction is significantly higher than that of the ^{20}Ne(^{12}C,^{6}He)^{26}Si, and thus this reaction gives higher statistics. Fig. 6.6 shows the Cathode vs. Scintillator histogram for this latter reaction.

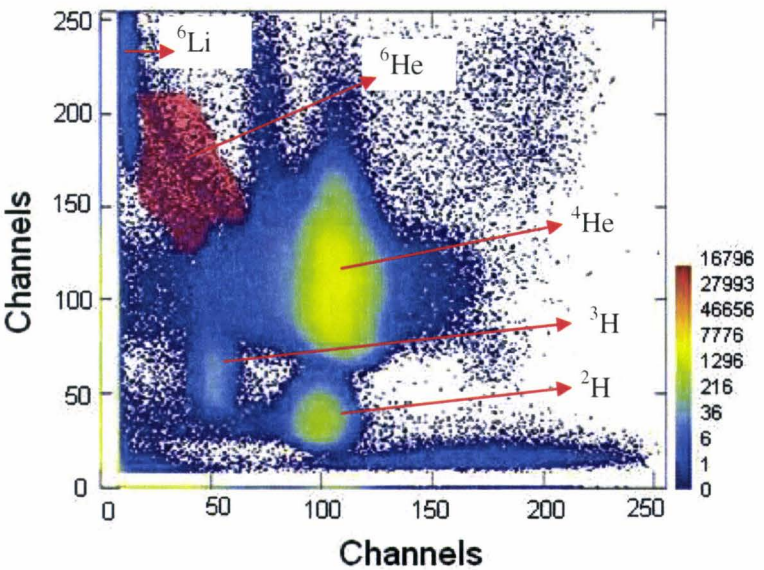

Figure 6.6: The energy loss of particles in cathode vs. the residual energy in the scintillator for particles emerging from the natural carbon target at $\theta = 5°$ and $E_{\text{beam}} = 70$ MeV. Deuterons, tritons, α-particles, ^{6}He, ^{6}Li particles as well as ^{7}Li groups were all present in the raw data, and were identified and labeled. The gates around the ^{6}He groups are shown by a red band. The color code to the right of the figure indicates intensity, where red is high and blue is low intensity.

Just like before, we identified different particle groups using the simulations and gated around the ^{6}He groups. After all the necessary gates were set, the momentum spectrum of the ^{6}He groups corresponding to the states in ^{18}Ne was generated (see Fig. 6.7).

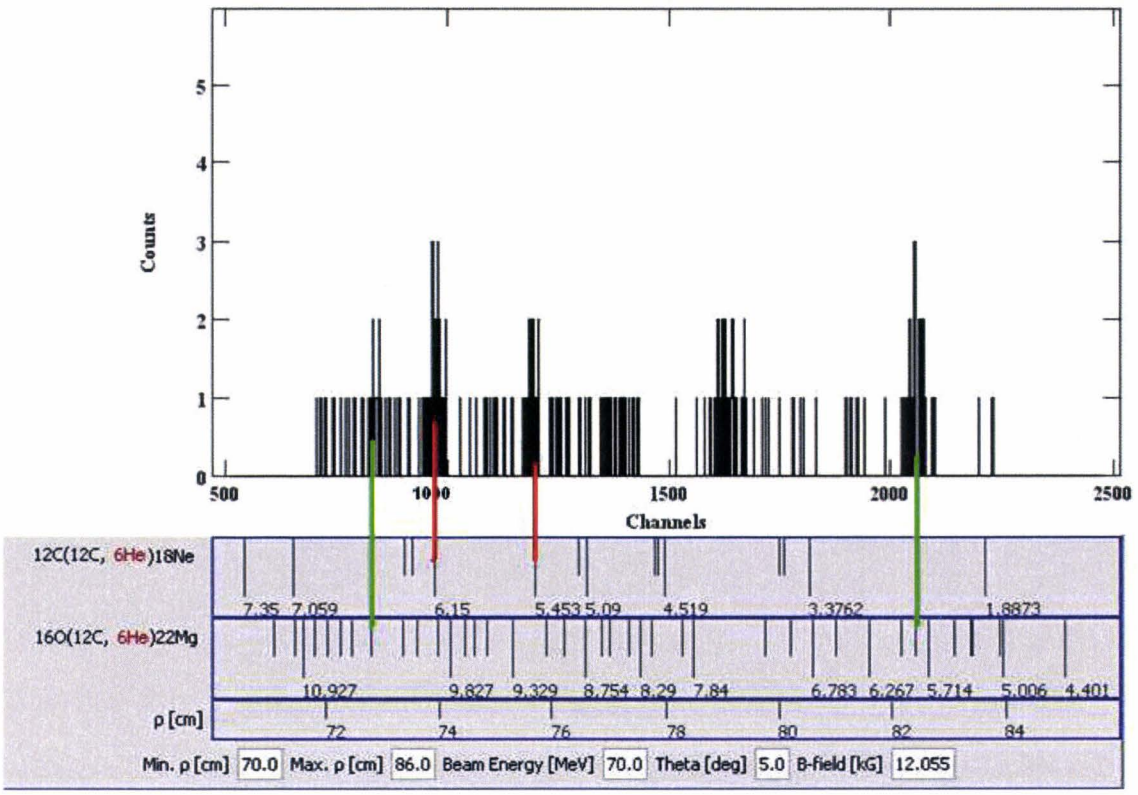

Figure 6.7: (Top) ^{6}He momentum spectrum corresponding to the ^{18}Ne states from the ^{12}C(^{12}C,^{6}He)^{18}Ne reaction at $\theta^{\text{lab}} = 5^{\circ}$ and $E_{\text{beam}} = 70$ MeV. (Bottom) The expected positions of the excited states of ^{18}Ne and ^{22}Mg from the simulations of the ^{12}C(^{12}C,^{6}He)^{18}Ne and the ^{12}C(^{16}O,^{6}He)^{22}Mg (the contaminant reaction) reactions at 70 MeV beam energy and $\sim$ 12 kG magnetic field at 5°. Note that on the bottom figure, ρ shows the curvature of the trajectories of the particles at the focal plane. The minimum and maximum curvatures are 70 cm and 86 cm, respectively. By comparing the states on the top histogram with the lines on the bottom figure (each line represents a state on the focal plane; only some of the energies are labeled), we can identify the ^{18}Ne states. The red and green lines match the states of ^{18}Ne and ^{22}Mg with the peaks on the spectrum, respectively.

By looking at this spectrum and comparing it with the simulation of the expected states on the focal plane, we see some states that might be from ^{22}Mg, which would come from the contaminant reaction ^{12}C(^{16}O,^{6}He)^{22}Mg (due to traces of water). Only two states might match up with the 5.45 and 6.15 MeV states in ^{18}Ne! The same reaction was investigated by Hahn *et al.* [131] with a similar setup (except the beam energy which was 80 MeV, and the focal plane detector which was different) and many states (up to 9.5 MeV; see Fig. 6.8) were seen.

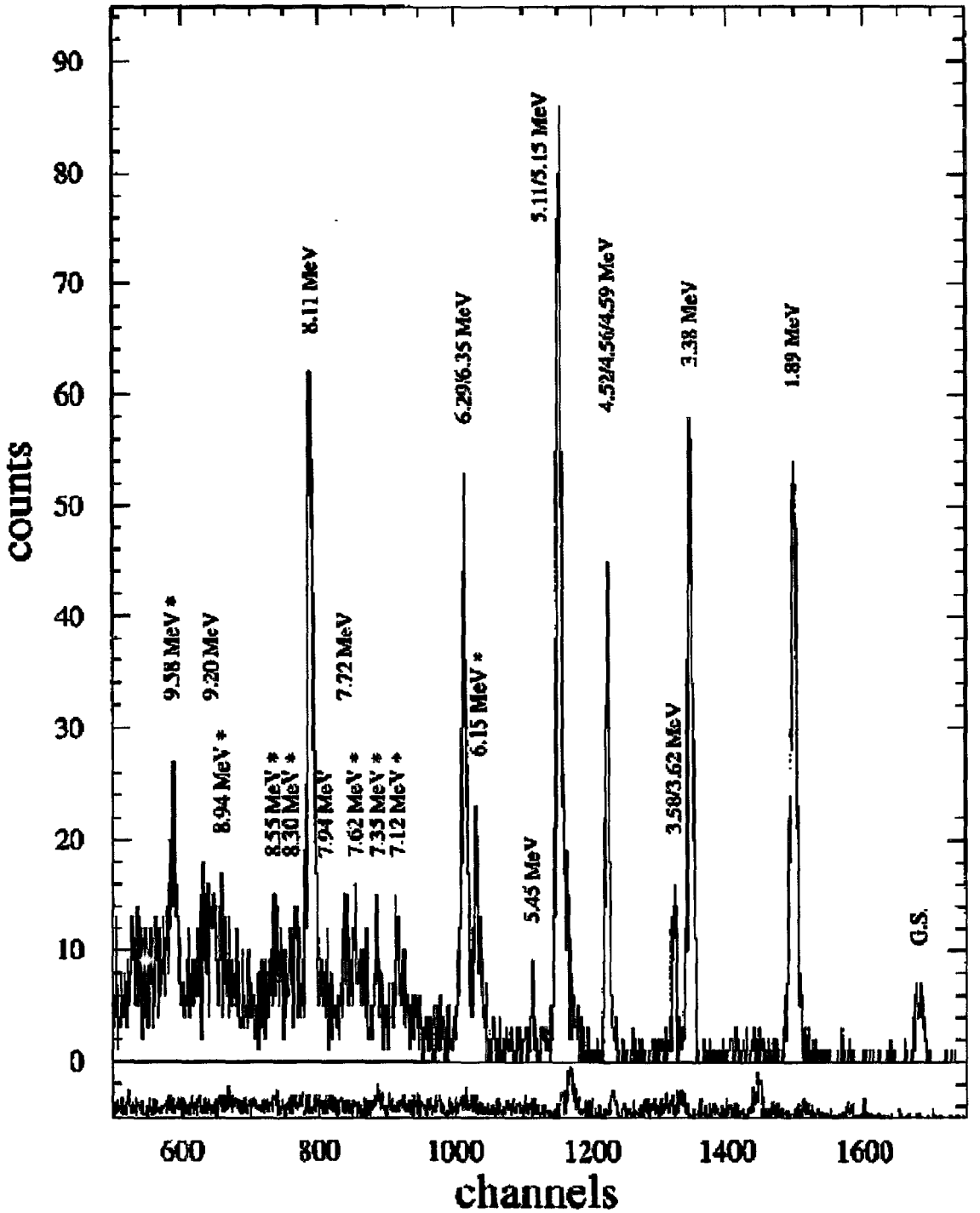

Figure 6.8: (Top) The spectrum of ^{18}Ne from the ^{12}C(^{12}C,^{6}He)^{18}Ne experiment done by Hahn *et al.* [131] with natural carbon target at lab angle of 4°. (Bottom) The same spectrum but for the ^{13}C(^{12}C,^{6}He)^{19}Ne reaction. The asterisk indicates a newly observed level by Hahn *et al.* The diagram is adopted from Ref. [131].

So why could we not see at least the ground and the first few excited states of ^{18}Ne? It seems that there were problems that might have resulted from a number of reasons: it could be that the cross section for the ^{20}Ne(^{12}C,^{6}He)^{26}Si reaction is too low, and the fact that the ^{20}Ne target is so thin makes it more difficult to detect ^{6}He particles; it is also possible that there is too little ^{20}Ne in the target; or the short run time did not allow for enough statistics to be collected; the problem might have also raised by not being able to detect ^{6}He groups. It seems that ^{6}He groups had not reached the scintillator, which could be due to not having enough energy. It is possible that the beam energy was not high enough to produce ^{6}He particles with enough energy to penetrate the ionization chamber. Another way to say the same thing is that the gas pressure inside the detector was too high, so ^{6}He groups lost most of their energy interacting with the gas molecules, and thus they did not have enough energy to deposit in the scintillator. However, the most probable reason was attributed to a failure in the electronics, so that we might have missed a signal. The fact that we did not even see the states of ^{18}Ne strongly suggested that there was either a problem with the electronics and perhaps some signals were missing, or the beam energy was not high enough, so that the ^{6}He groups did not gain enough energy to reach the scintillator to produce the signals that could be detected.

In July 2007, we carried out the ^{20}Ne(^{12}C,^{6}He)^{26}Si experiment again. At first, just to test whether the run condition were the same as in January 2007. we tried the ^{12}C(^{12}C,^{6}He)^{18}Ne experiment which would give us more yield due to higher cross section. The setup parameters are shown in Table 6.2.

Just like before, the ^{6}He particle groups were identified, and the gates were set around them. The momentum spectrum of the ^{6}He groups corresponding to the states in ^{18}Ne was achieved and is shown in Fig. 6.9. Note that this spectrum was achieved after 6 hours and thirty minutes of collecting data.

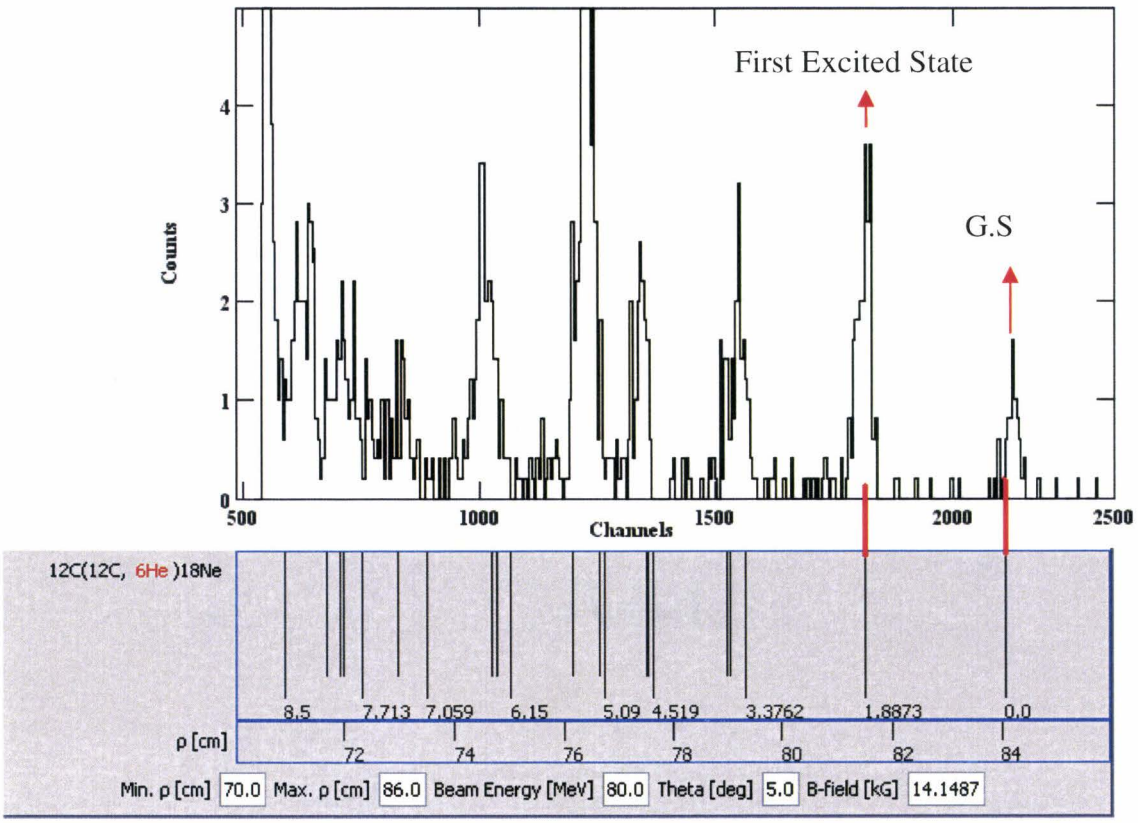

Figure 6.9: (Top) ^{6}He momentum spectrum corresponding to the ^{18}Ne states from the ^{12}C(^{12}C,^{6}He)^{18}Ne reaction at $\theta^{\text{lab}} = 5^{\circ}$ and $E_{\text{beam}} = 80$ MeV. The focal plane starts from channel 500 and ends on channel 2500. (Bottom) The expected positions of the excited states of ^{18}Ne along the focal plane from the simulation of the ^{12}C(^{12}C,^{6}He)^{18}Ne reaction at 80 MeV beam energy and $\sim$ 14 kG magnetic field at 5°. Note that on the bottom figure, ρ shows the curvature of the trajectories of the particles along the focal plane. The minimum and maximum curvatures are 70 cm and 86 cm, respectively. By comparing the peaks on the top histogram with the lines on the bottom figure (each line represents a state of ^{18}Ne on the focal plane; only some of the energies are labeled), we can identify the states of ^{18}Ne.

Table 6.2: The experimental setup for the ^{12}C(^{12}C,^{6}He)^{18}Ne run in July 2007.

E (MeV)	P (Torr)	B (kG)	θ (degrees)	Z	$\Delta\theta$ (mrad)	$\Delta\phi$ (mrad)	q[a]	V_C (V)	V_{wires} (V)
80	100	14.1487	5	51.4	$\pm$40	$\pm$40	5^{+}	-600	1400

[a]Charge state of the beam

From Fig. 6.9, we can clearly match the ground state and the first few excited

state of ^{18}Ne. The other states also match with the simulations and also with the previous work by Hahn (see Fig. 6.8). In the July 2007 run, we did not encounter the problems experienced in January 2007. It should be noted that for the test run, the scintillator signal was used as a trigger for the electronics, and thus if the particles did not reach the scintillator, we would not detect them. In the July 2007 experiment, we changed the trigger to be the cathode signal. By comparing Fig. 6.6 with Fig. 6.3a, it can be concluded that most of the ^{6}He particles of interest did not reach the scintillator in January 2007 run. That was why we could not achieve the proper spectrum. In Fig. 6.6, we gated around some random events that look more like the tail of other particle groups, which were located in the position where ^{6}He groups were expected. But, in Fig. 6.3a, ^{6}He groups are well identified groups.

In order to find the energy corresponding to each channel on the focal plane, we calibrated the focal plane using peaks corresponding to the ground state and the first excited state of ^{18}Ne and six isolated well-identified peaks corresponding to the states of ^{20}Ne from the ^{12}C(^{12}C,^{4}He)^{20}Ne reaction[4]. These peaks are given in Table 6.3.

Table 6.3: The peaks used for calibration of the focal plane and their properties.

Nucleus[a]	Channel Number of the peak	Uncertainty in Channel	Peak Energy (MeV)	Uncertainty (keV)
^{18}Ne	1822.8	1.94	0	0.0001[b]
^{18}Ne	1521	0.0729	1.8873	2
^{20}Ne	2365.96	1.95	0	0.001
^{20}Ne	2233.33	0.145	1.634	15
^{20}Ne	2004.61	0.041	4.248	11
^{20}Ne	1940.34	0.250	4.967	20
^{20}Ne	1880.64	0.084	5.788	26
^{20}Ne	1722.54	0.532	7.833	15

[a]The nucleus to which the peak belongs

[b]Even if the energy of the ground state does not include any uncertainty at the level of precision, we needed to use a non-zero value for the uncertainty in energy just to make the fitting program start working.

It is important to note that the calibration of the focal plane is necessary to

[4]The spectrum of ^{20}Ne was achieved by gating around the α-particles, which were present in the ^{20}Ne(^{12}C,^{6}He)^{26}Si experiment.

find the energies of the peaks in any given spectrum. In order to find the excitation energies, one needs to fit the peaks, whose energies need to be defined, and use the centroid of each peak as an input for a program, called Spanc, which converts the channel number of the peak to the energy. However, in this project, we were only able to fit the peaks shown in Table 6.3. The peaks from the spectrum in Fig. 6.9 or all the other spectra could not be fitted due to low statistics, which resulted in a fit with huge uncertainties in the resultant excitation energies. For the cases where the statistic was relatively high, we could not identify individual peaks due to high densities of the excitation levels (except for the first excited state of ^{18}Ne, which is a well-identified peak). Thus, we could not find the centroid of these peaks to be able to find their energies by the application of Spanc and the calibrated focal plane.

Having confirmed that our setup reproduced known results, we were confident that we were detecting ^{6}He groups properly, and thus we decided to investigate the ^{20}Ne target properties to understand why no ^{26}Si peaks were seen in January 2007. So, we changed the target to the implanted ^{20}Ne target. The setup for the ^{20}Ne(^{12}C,^{6}He)^{26}Si experiment is the same as the ^{12}C(^{12}C,^{6}He)^{18}Ne experiment, except for the magnetic field of the spectrometer and the position of the focal plane detector, which were 14.60055 kG and 53.1, respectively. As with the ^{12}C(^{12}C,^{6}He)^{18}Ne experiment, we gated around ^{6}He particles, and the spectrum of ^{26}Si was obtained (see Fig. 6.10).

By comparing Fig. 6.10 to Fig. 6.9, it is obvious that in the ^{20}Ne(^{12}C,^{6}He)^{26}Si experiment, we see some peaks located above the ground state of ^{18}Ne, which were not present in the ^{12}C(^{12}C,^{6}He)^{18}Ne experiment. Thus, by looking at the simulation of states along the focal plane in Fig. 6.10, these peaks must be coming from either ^{26}Si or ^{19}Ne from the contaminant reaction of ^{13}C(^{12}C,^{6}He)^{19}Ne (^{13}C comprises 1.1% of natural carbon. It should be noted that the ^{20}Ne is implanted in carbon, and thus the implanted ^{20}Ne target also contains ^{13}C). To be able to identify these peaks and to check for the contaminants, we changed the implanted ^{20}Ne target to an isotopically pure ^{13}C target of thickness of 103.8 μg/cm^2. The spectrum that was obtained due to the gates around ^{6}He particles is shown in Fig. 6.11. From this spectrum, it appears that most of the peaks before the ground state of ^{18}Ne in Fig. 6.10 come from the contaminant ^{13}C.

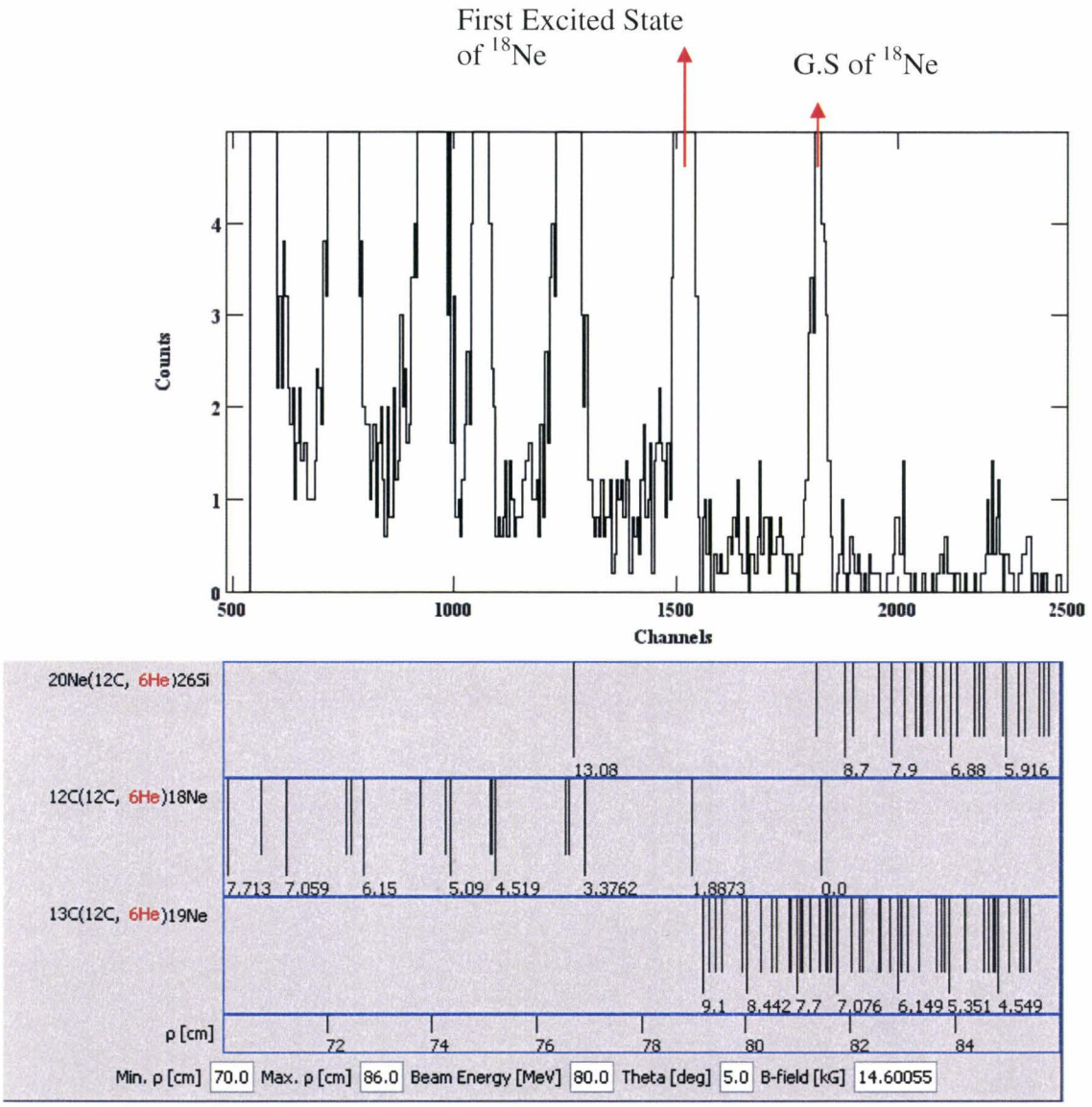

Figure 6.10: (Top) The spectrum achieved by gating around the ^{6}He particles in the ^{20}Ne(^{12}C,^{6}He)^{26}Si experiment at $\theta^{\text{lab}} = 5^{\circ}$ and $E_{\text{beam}} = 80$ MeV. (Bottom) The expected positions of the excited states of ^{26}Si, ^{18}Ne and ^{19}Ne along the focal plane from the simulations of the ^{20}Ne(^{12}C,^{6}He)^{26}Si, ^{12}C(^{12}C,^{6}He)^{18}Ne and the ^{13}C(^{12}C,^{6}He)^{19}Ne reactions, respectively. The latter reactions are contaminant reactions. By comparing the peaks on the top histogram with the lines on the bottom figure (each line represents a state on the focal plane; only some of the energies are labeled), we can identify each peak on the histogram. The ground state and the first excited state of ^{18}Ne are indicated. This spectrum was acquired after approximately 24 hours of data collection.

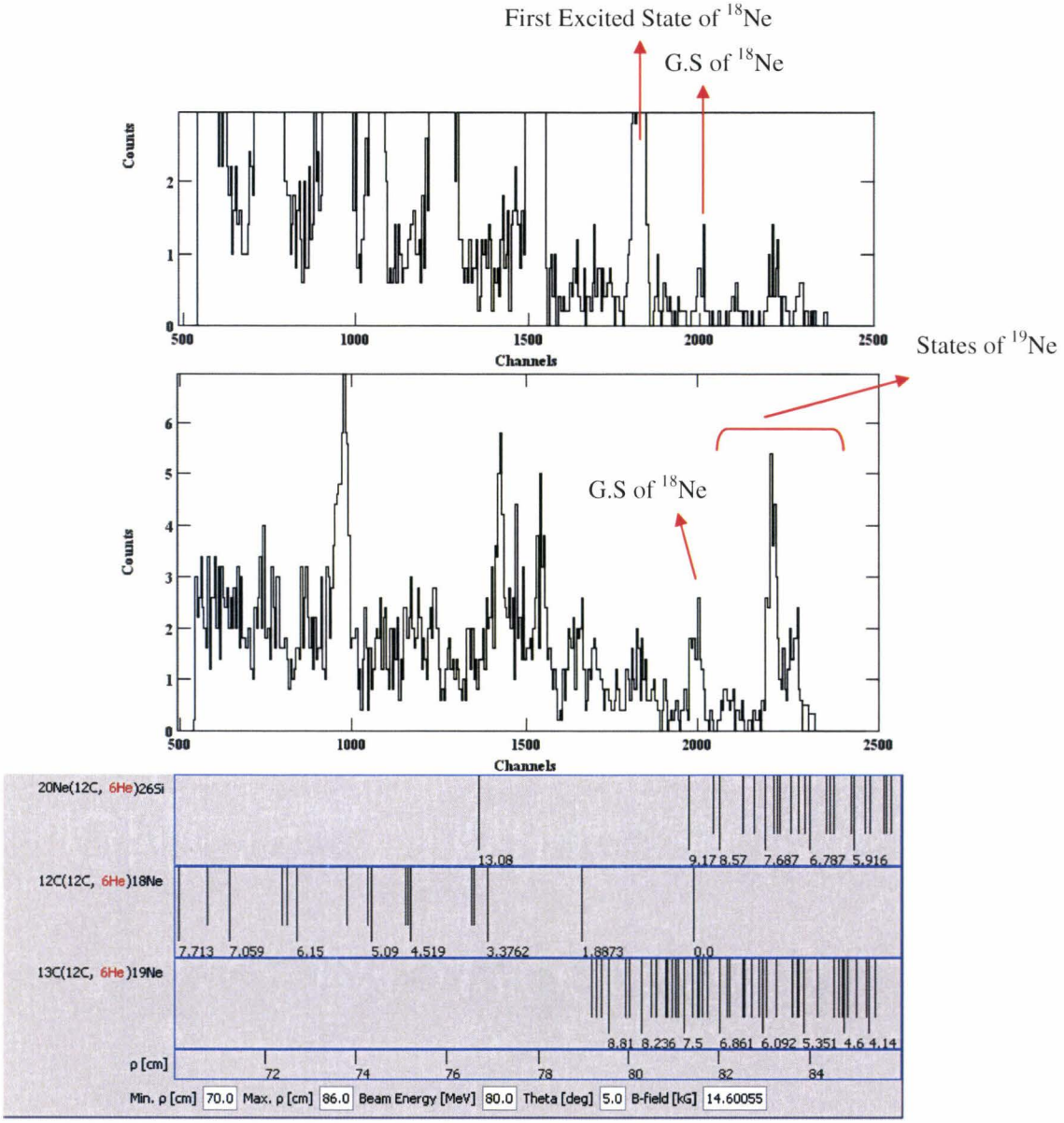

Figure 6.11: (Top) The spectrum achieved by gating around the ^{6}He particles in the ^{20}Ne(^{12}C,^{6}He)^{26}Si experiment at $\theta^{\text{lab}} = 5^{\circ}$ and $E_{\text{beam}} = 80$ MeV. (Middle) The spectrum achieved by gating around the ^{6}He particles in the ^{13}C(^{12}C,^{6}He)^{19}Ne experiment at $\theta^{\text{lab}} = 5^{\circ}$ and $E_{\text{beam}} = 80$ MeV. (Bottom) The expected positions of the excited states of ^{26}Si, ^{18}Ne and ^{19}Ne along the focal plane from the simulations of the ^{20}Ne(^{12}C,^{6}He)^{26}Si, ^{12}C(^{12}C,^{6}He)^{18}Ne and ^{13}C(^{12}C,^{6}He)^{19}Ne reactions, respectively. The latter reaction is the contaminant reaction. This spectrum was achieved after about 40 minutes of data collection. As can be seen, the states above the ground states of ^{18}Ne are the ^{19}Ne states.

Since the implanted ^{20}Ne target that was used resulted in a spectrum which was very similar to that achieved from the ^{12}C target, we suspected that, the ^{20}Ne nuclei might have diffused out of the target due to its age and thinness. To check whether or not there was ^{20}Ne in the target, we investigated the elastic scattering of the ^{12}C beam off the ^{20}Ne, natural carbon and ^{13}C targets in the ^{20}Ne(^{12}C,^{12}C)^{20}Ne, ^{12}C(^{12}C,^{12}C)^{12}C and ^{13}C(^{12}C,^{12}C)^{13}C experiments, respectively. In order to do so, we changed the magnetic field of the spectrometer to 9 kG and its angle was also changed to 15°. The position of the focal plane detector was set at $Z = 40.2$, and the horizontal and vertical slits were set at ±40 and ±10 mrad, respectively. Then, we gated around the scattered ^{12}C particles and the spectra were achieved, as shown in Fig. 6.12 to Fig. 6.14.

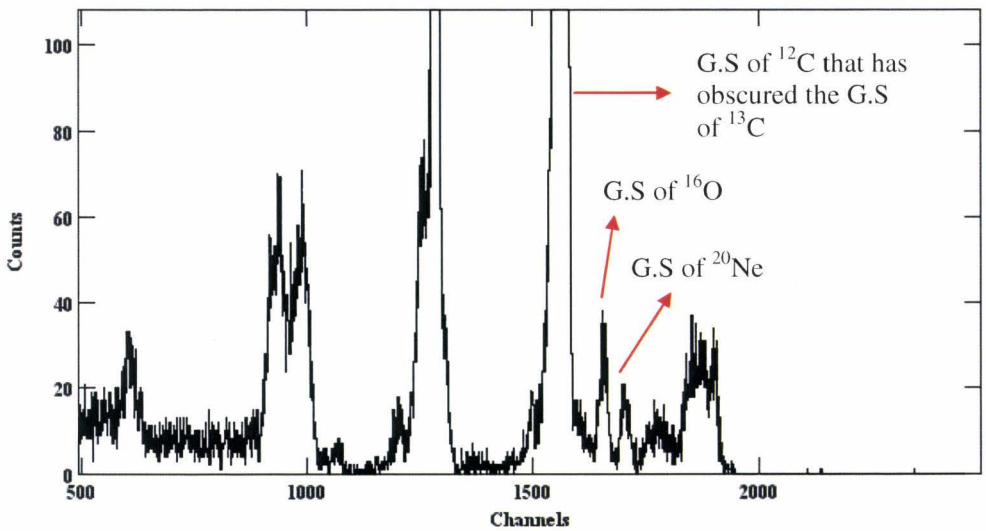

Figure 6.12: The spectrum achieved by gating around the scattered ^{12}C particles in the ^{20}Ne(^{12}C,^{12}C)^{20}Ne scattering experiment at $\theta^{\text{lab}} = 15^{\circ}$ and $E_{\text{beam}} = 80$ MeV. The ground state of ^{12}C has obscured the ground state of ^{13}C. The two mysterious peaks located above the ground state of ^{20}Ne might be coming from the choice of the gates on the Scintillator vs. Front Position and the Cathode vs. Scintillator histograms. These gates contained ^{12}C, deuterons and α-particles, because they overlapped due to the same A/q ratios.

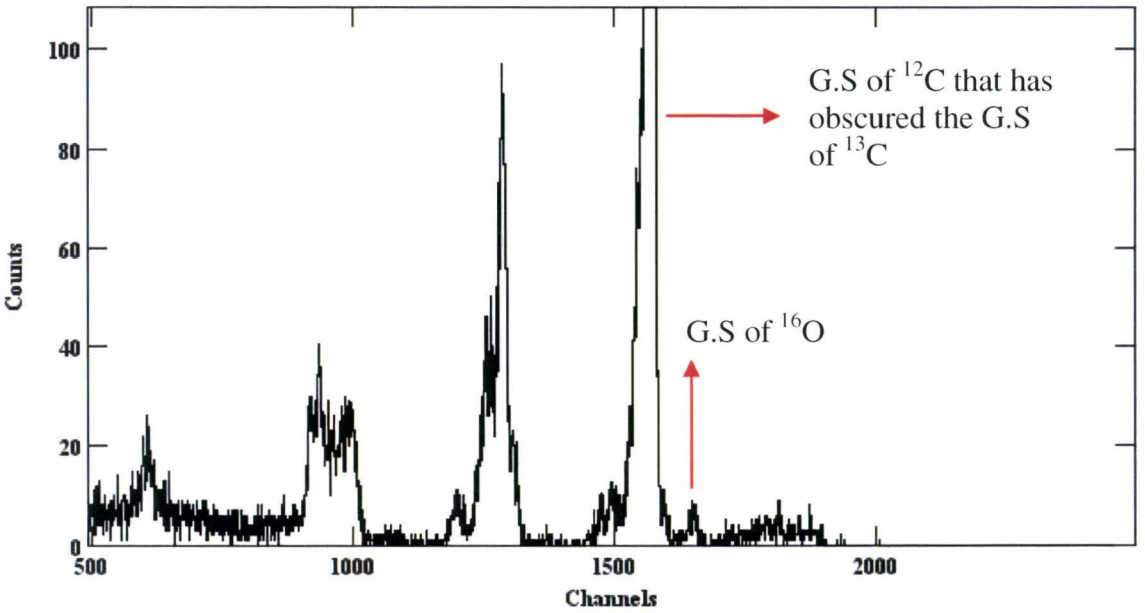

Figure 6.13: The spectrum achieved by gating around the scattered ^{12}C particles in the ^{12}C(^{12}C,^{12}C)^{12}C scattering experiment at $\theta^{\text{lab}} = 15^{\circ}$ and $E_{\text{beam}} = 80$ MeV.

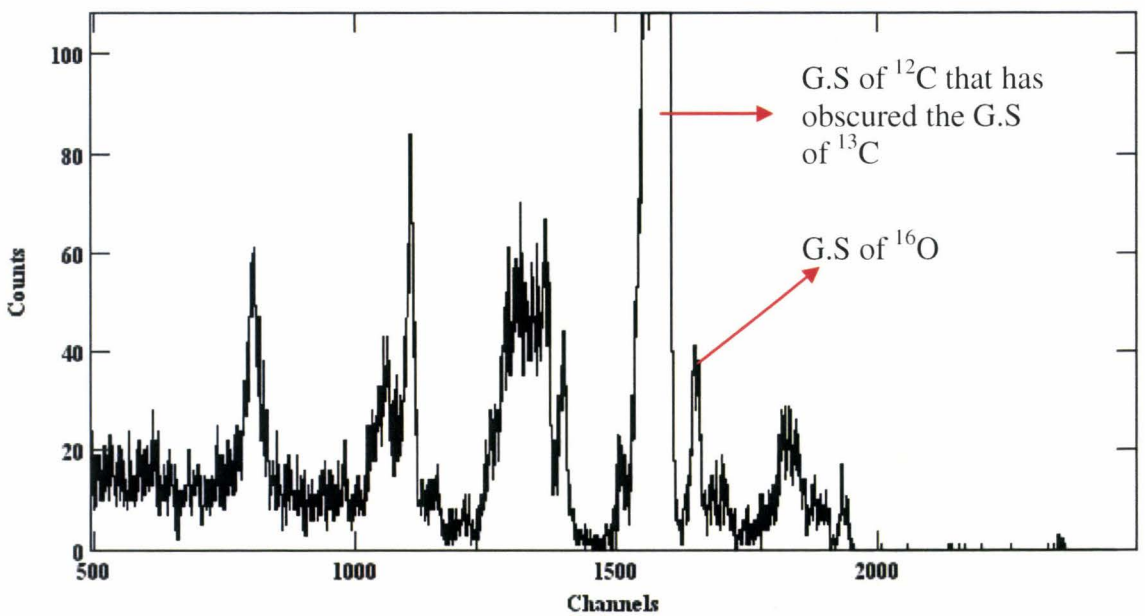

Figure 6.14: The spectrum achieved by gating around the scattered ^{12}C particles in the ^{13}C(^{12}C,^{12}C)^{13}C scattering experiment at $\theta^{\text{lab}} = 15^{\circ}$ and $E_{\text{beam}} = 80$ MeV.

From Fig. 6.12, we were assured that there was still ^{20}Ne inside our target. To check the thickness of the ^{20}Ne target, we used the spectrum shown in Fig. 6.12. The ^{20}Ne target was made by implanting 4 layers of ^{20}Ne (with the original total

thickness of 7±1 $\mu g/cm^2$) into five layers of natural carbon (with the total thickness of 40 $\mu g/cm^2$). From the scattering experiments that were done using this target, and from the Rutherford cross section for the $^{20}Ne(^{12}C,^{12}C)^{20}Ne$ scattering experiment, we found that the current thickness of the ^{20}Ne target which we used is 1.6 $\mu g/cm^2$ of ^{20}Ne implanted in 40 $\mu g/cm^2$ of ^{12}C. So the ^{20}Ne has migrated out in such a way that the remaining number density of the ^{20}Ne nuclei in the target is not enough for the interaction with the beam to produce a significant amount of ^{26}Si. This together with the high Coulomb barrier and low cross section for this reaction resulted in our not being able to study the structure of ^{26}Si via the (^{12}C,^{6}He) reaction mechanism. Therefore, we tried to see whether this reaction mechanism could be used to study the structure of ^{30}S. This latter experiment is discussed in the next section.

6.3 The $^{12}C(^{24}Mg,^{6}He)^{30}S$ Experiment

For this experiment, we first tried to bombard a magnesium target (319.5 $\mu g/cm^2$ of ^{24}Mg on 11.1 $\mu g/cm^2$ of natural carbon backing) with the 70 MeV ^{12}C beam, since the beam was already available. In order to do so, we changed the magnetic field of the spectrometer to 14.594 kG and the position of the focal plane detector was set to $Z = 53.3$. The horizontal and vertical slits were opened to ±40 mrad each. The spectrum that was obtained after about 13 hours is shown in Fig. 6.15. As can be seen from this figure, due to oxidization of the ^{24}Mg target, there was contamination from ^{16}O in the spectra. In addition, the natural carbon backing also contained ^{13}C, which resulted in another source of contamination. Due to high density of the states, the peaks in this spectrum could not be identified properly.

Referring to the simulations of the ^{30}S, ^{22}Mg and ^{19}Ne states along the focal plane at the bottom of Fig. 6.15, we can see that the states of ^{30}S and the first few states of ^{19}Ne overlap with each other.

As a result of contaminants in the ^{24}Mg target, we decided to use a natural carbon target of thickness 91.8 $\mu g/cm^2$ and a ^{24}Mg beam with the energy of 90 MeV. The setup parameters for this latter experiment is shown in Table 6.4.

The location of the ^{6}He group in different histograms was found by simulations (see Fig. 6.16).

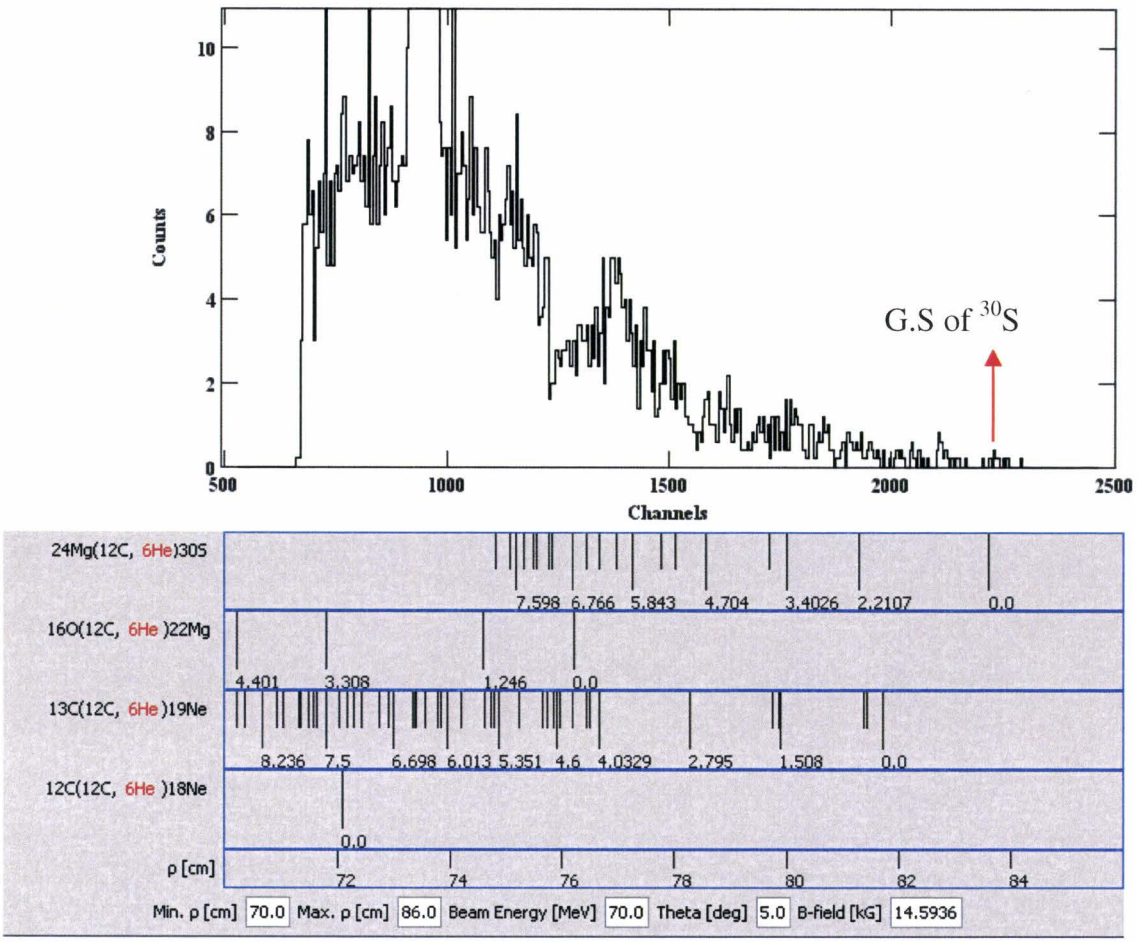

Figure 6.15: Top) The spectrum achieved by gating around the ^{6}He particles in the ^{24}Mg(^{12}C,^{6}He)^{30}S experiment at $\theta^{\text{lab}} = 5^{\circ}$ and $E_{\text{beam}} = 70$ MeV. (Bottom) The expected positions of the excited states of ^{30}S, ^{22}Mg and ^{19}Ne along the focal plane from the simulations. The latter two nuclei are produced by the contaminant reactions ^{16}O(^{12}C,^{6}He)^{22}Mg and ^{13}C(^{12}C,^{6}He)^{19}Ne, respectively. The ground state of ^{30}S is identified and labeled on the spectrum.

Table 6.4: The experimental setup for the ^{12}C(^{24}Mg,^{6}He)^{30}S experiment.

E (MeV)	P (Torr)	B (kG)	θ (degrees)	Z	$\Delta\theta$ (mrad)	$\Delta\phi$ (mrad)	V_C (V)	V_{wires} (V)
90	100	13.1005	5	49.4	$\pm$40	$\pm$40	-600	1400

We used a ^{13}C target of thickness 103.8 μg/cm^2 to find the ^{6}He groups and to draw the gates. The experimental setup was the same as before. The Q-value of the ^{13}C(^{24}Mg,^{6}He)^{31}S reaction is -9.36 MeV and the Coulomb barrier is 15.8 MeV.

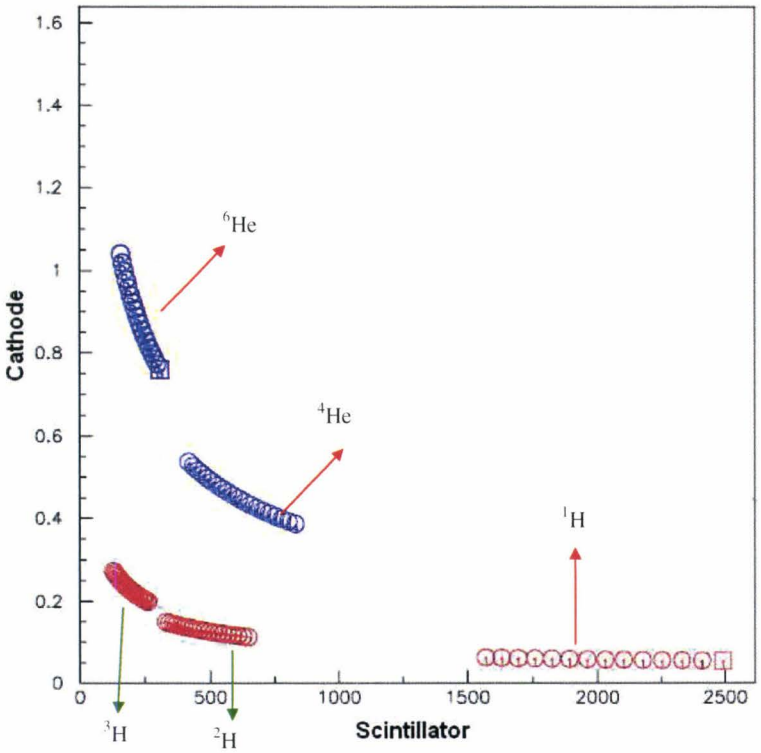

Figure 6.16: Particle simulations for the Cathode vs. Scintillator plot in the ^{12}C(^{24}Mg,^{6}He)^{30}S experiment at $E_{\text{beam}} = 90$ MeV. Different shapes and colors indicate different particle groups.

Thus, with the latter target, we were able to find ^{6}He groups and draw a gate around them on different histograms (see Fig. 6.17). It should be noted that the location of ^{6}He particles on different histograms would not be changed noticeably by changing from the natural carbon target with the ^{13}C one. So, the gates on the histograms produced by the ^{13}C target could be used. A few hours of running with the ^{13}C target yielded enough data to set the gates around ^{6}He groups. Thus, the target was changed back to the natural carbon target and we ran the ^{12}C(^{24}Mg,^{6}He)^{30}S experiment for about 9 hours until the end of our beamtime. The ^{6}He spectrum that was obtained is shown in Fig. 6.18.

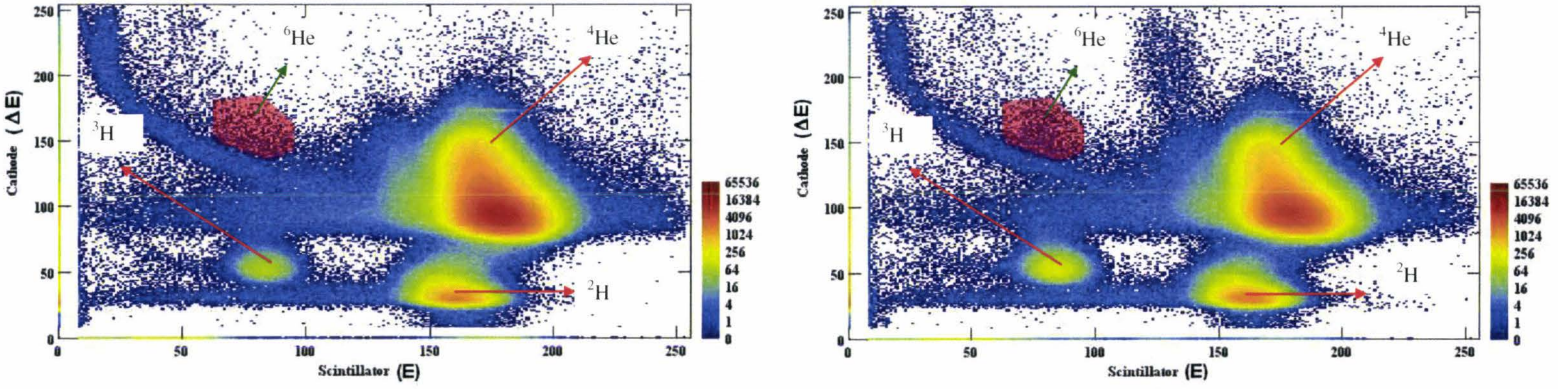

(a) ^{12}C(^{24}Mg,^{6}He)^{30}S (b) ^{13}C(^{24}Mg,^{6}He)^{31}S

Figure 6.17: The energy loss of particles in cathode vs. the residual energy in the scintillator for particles emerging from the natural carbon (Top) and the ^{13}C (Bottom) targets in the ^{12}C(^{24}Mg,^{6}He)^{30}S and the ^{13}C(^{24}Mg,^{6}He)^{31}S experiments at $\theta = 5°$ and $E_{\text{beam}} = 90$ MeV. Deuterons, tritons, α-particles, as well as ^{6}He groups were all present in the raw data, and were identified and are indicated. The gates around the ^{6}He groups are shown by a red band. The ^{6}He groups are more obvious in Fig. 6.17b. This is due to lower Coulomb barrier of this reaction. Thus, the latter ^{6}He groups have more energy. The color code to the right of figure indicates intensity, where red is high and blue is low intensity.

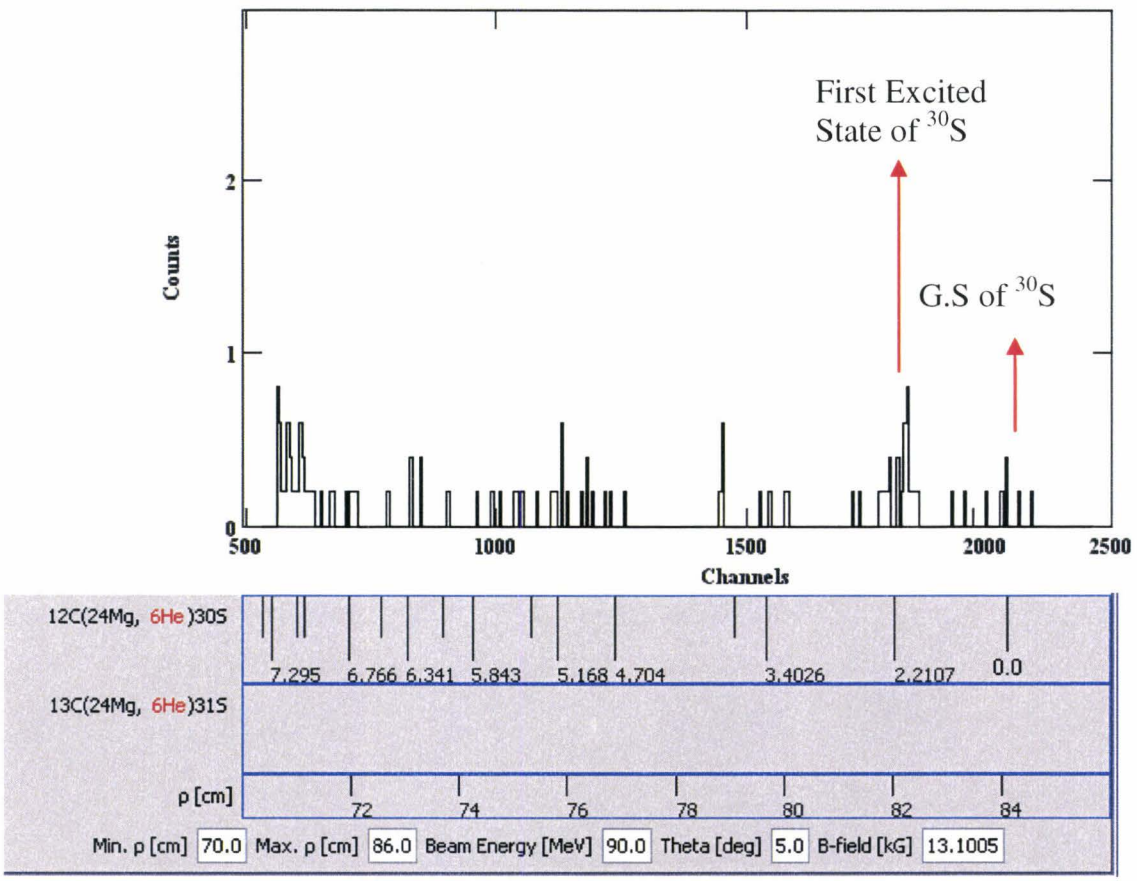

Figure 6.18: (Top) The momentum spectrum of ^{6}He particles corresponding to the states of ^{30}S in the ^{12}C(^{24}Mg,^{6}He)^{30}S experiment at $\theta^{\text{lab}} = 5^{\circ}$ and $E_{\text{beam}} = 90$ MeV. (Bottom) The expected positions of the excited states of ^{30}S along the focal plane from the simulation. The statistics are low; however, the peaks on the spectrum still match with the simulations. The ^{30}S excitation energies up to 5 MeV are populated.

From the simulations at the bottom of Fig. 6.18, we are assured that the only source of contamination which may come from the ^{13}C in the natural carbon target will not play any role with our particular experimental setup: in this experiment, no state of ^{31}S will be populated at the focal plane between 70 to 86 cm. Thus, whatever is detected on the focal plane must have come from ^{30}S. This together with the fact that the states that we see on Fig. 6.18 despite low statistics, convince us that the (^{12}C,^{6}He) reaction mechanism is promising to carry out the studies of the structure of ^{30}S further.

We were not able to calibrate the focal plane for this experiment using either of ^{13}C(^{24}Mg,^{6}He)^{31}S or ^{12}C(^{24}Mg,^{4}He)^{32}S contaminant reactions[5], because the former resulted in peaks so low in statistics that could not be fitted, and the latter resulted in a spectrum that did not show any isolated, well-identified peak.

We have calculated the total and the differential cross sections for the ^{12}C(^{24}Mg,^{6}He)^{30}S reaction. To calculate the cross sections, we have inferred from comparing the simulations with the spectrum (Fig. 6.18) that the ground state of ^{30}S is located between channels 2000 to 2200 (see Fig. 6.18), and the first excited state is located between channels 1800 to 2000. However, this conclusion is uncertain due to low statistics. According to our estimation, the total cross sections for the ground state and the first excited state are 1.43×10^{-1} and 6.85×10^{-1} nb, respectively. The solid angle for the ^{24}Mg(^{12}C,^{6}He)^{30}S reaction is 6.4 msr, and thus the differential cross sections for the ground state and the first excited state would be 0.02 and 0.1 μb/sr, respectively.

6.4 Future Work

It is certainly worthwhile to try to investigate the ^{20}Ne(^{12}C,^{6}He)^{26}Si experiment in inverse kinematics with the use of ^{20}Ne beam impinging on a isotopically pure ^{12}C target. However, this is not possible at Yale University, since ^{20}Ne cannot be made as a negative ion. ^{20}Ne beams are available at ATLAS[6]. They also have a split-pole spectrometer.

[5]The latter reaction can be investigated by gating around α-particles instead of ^{6}He particles.
[6]Argonne Tandem-Linear Accelerator System at Argonne National Laboratory

As for studying the structure of ^{30}S, the (^{12}C,^{6}He) reaction mechanism proved to be a good technique to obtain information on the excitation energies of ^{30}S. For the future work, we have decided to run this experiment again, and if each run lasts for about two weeks during which we investigate one angle at a time, we will be able to collect enough data for a few angles. We will also be trying the ^{32}S(p,t)^{30}S reaction at Yale University as a complementary experiment to populate the excited states in ^{30}S to be able to determine the nuclear structure of this nucleus, which can be further used in the calculation of the ^{29}P(p,γ)^{30}S reaction rate to reduce its uncertainty over the temperature range of interest. This is important in order to better measuring the Si isotopic abundances in presolar grains with high precision, which are in turn crucial in understanding the mechanism of the nova outbursts and to constraining the nova models.

Chapter 7

Conclusion

The present work was motivated by our interest to investigate the impact of nuclear reactions on the stellar yields, as well as to point out that the nuclear structure information is significant in understanding the rate of thermonuclear reactions.

Various phenomena in the universe are powered by thermonuclear reactions. In this project, we have paid attention to the ^{23}Na(p,α)^{20}Ne, ^{23}Na(p,γ)^{24}Mg and ^{26g}Al(p,γ)^{27}Si reactions, whose rates were previously uncertain by many orders of magnitude. Recently, new experimental information on the resonance energies and their strengths that contribute to these reaction rates have been released to the literature, and we have used this information to recalculate these reaction rates, which were then used by a stellar nucleosynthesis code to calculate the resultant AGB yields for the nuclei in the mass range of $20 \leq A \leq 30$.

Despite reducing the uncertainty ranges in all those reaction rates as a result of using the most recent experimental information, most of the AGB yields were not changed significantly by simultaneously varying the ^{23}Na(p,α)^{20}Ne, ^{23}Na(p,γ)^{24}Mg and ^{26g}Al(p,γ)^{27}Si reaction rates to the recommended ones presented in this project. However, there are major changes to a few isotopes: ^{20}Ne is considerably destroyed and ^{23}Na, ^{24}Mg and ^{28}Si are produced significantly as a result of varying all three reaction rates. In the future, it is worthwhile to calculate the yield uncertainties taking into consideration the uncertainty ranges in those reaction rates, as it may shed light on whether the AGB stars are the candidates for introducing the abundance anomalies observed in the globular clusters. As well, the yields can be used as an

input to the GCE models to see wether they can reproduce the observed stellar and galactic abundance patterns.

In the present work, we have has also investigated the (^{12}C,^{6}He) reaction mechanism to study the nuclear structure of ^{26}Si and ^{30}S via the ^{20}Ne(^{12}C,^{6}He)^{26}Si and ^{12}C(^{24}Mg,^{6}He)^{30}S reactions, respectively. Such structures are important in understanding the rates of the ^{25}Al(p,γ)^{26}Si and ^{29}P(p,γ)^{30}S reactions, which are in turn important to understand the yield of galactic ^{26}Al from the classical novae and to gain information about the details of the nova outbursts, respectively.

The results proved that this technique could be a good method to measure the excitation energies of ^{30}S. But, we were unable to determine whether the excitation energies of ^{26}Si can also be studied via this mechanism. This was due to the fact that the implanted ^{20}Ne target we used did not contain enough ^{20}Ne.

Appendix A

Stellar Yields

Tables A.1 to A.12 display the stellar yields for 22 species. Each of these yield tables contains 8 columns which are: the species; the atomic mass number of that species; the stellar yield in solar masses; $\text{mass}_{i,\text{lost}}$ is the amount of that species lost in the wind (in solar masses) integrated over the entire stellar lifetime (most mass is lost during the AGB); $\text{mass}_{i,0}$ is the initial amount of that species in the wind in solar masses; $< X(i) >$ is the average mass fraction of species in the wind lost from the star; $X_0(i)$ is the initial mass fraction; and $\log(\frac{<X(i)>}{X_0(i)})$ is the production factor, respectively. It should be noted that negative yield means the isotope was consumed by nucleosynthesis processes, and hence the final surface abundance is lower than the initial; and positive yield means the isotope was produced by nucleosynthesis processes, and hence the final surface abundance is greater than the initial.

Figures A.1 to A.3 show the percentage differences between the standard yields of 22 selected isotopes (from ^{20}Ne to ^{30}Si) and the yields using one of the updated ^{23}Na(p,α)^{20}Ne, ^{23}Na(p,γ)^{24}Mg or ^{26g}Al(p,γ)^{27}Si reaction rates at a time. It should be noted that any difference between the two sets of yields that is smaller than 5% is negligible.

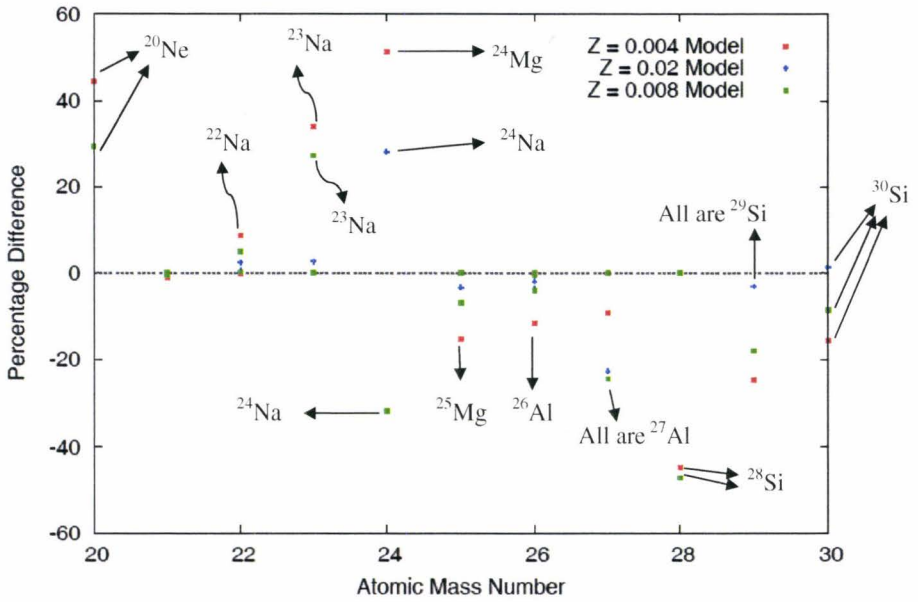

Figure A.1: The percentage differences between the standard yields and the yields obtained from using the updated ^{23}Na(p,γ)^{24}Mg reaction rate. Note that only those isotopes are labeled for which the percentage differences are greater than 5%.

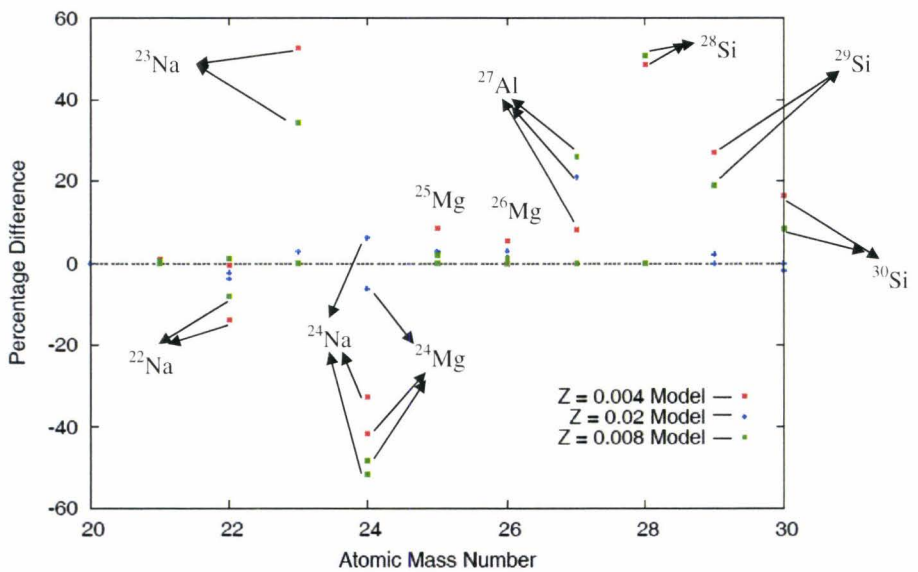

Figure A.2: The percentage differences between the standard yields and the yields obtained from using the updated ^{23}Na(p,α)^{20}Ne reaction rate. Note that only those isotopes are labeled for which the percentage differences are greater than 5%.

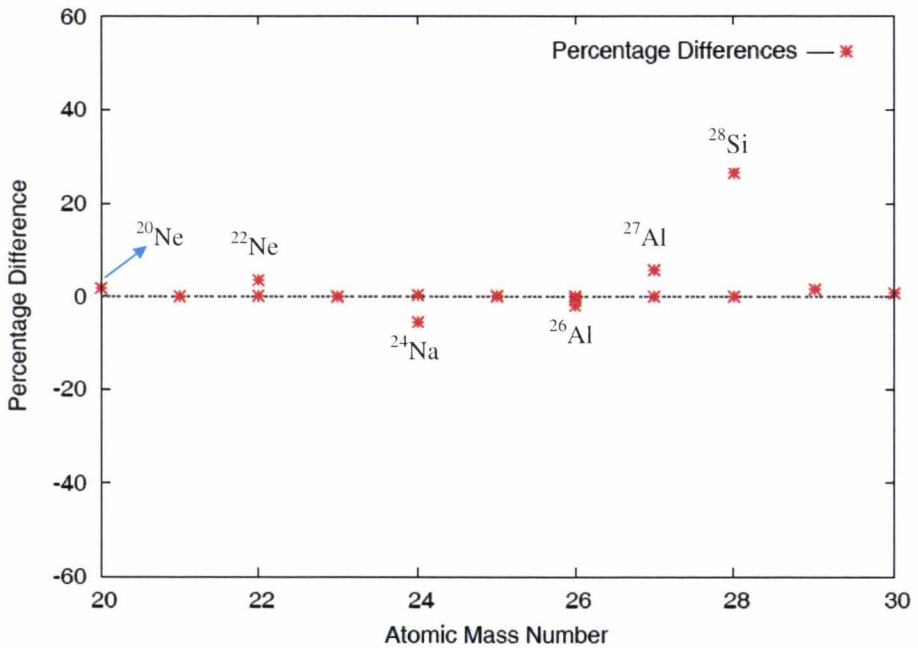

Figure A.3: The percentage differences between the standard yields and the yields obtained from using the updated ^{26g}Al(p,γ)^{27}Si reaction rate for the $Z = 0.02$ model. Using the updated ^{26g}Al(p,γ)^{27}Si reaction rate in the $Z = 0.004$ and $Z = 0.008$ model led to no noticeable effect on any of the yields. On the diagram only those isotopes are labeled for which the percentage differences are either above or below the dotted horizontal line. Note that only for the cases of ^{27}Al and ^{28}Si, the percentage differences are higher than 5% which are 6% and 27%, respectively).

Table A.1: The standard set of stellar yields for the $6\,M_{\odot}$, $Z = 0.02$ model.

Species	Mass Number	Yield	$\text{Mass}_{i,\text{lost}}$	$\text{Mass}_{i,0}$	$< X(i) >$	$X_0(i)$	$\log(\frac{<X(i)>}{X_0(i)})$
^{20}Ne	20	8.9072E-06	8.2301E-03	8.2211E-03	1.6230E-03	1.6213E-03	4.4442E-04
^{21}Ne	21	-1.9881E-05	1.0740E-06	2.0955E-05	2.1178E-07	4.1325E-06	-1.2903E+00
^{22}Ne	22	3.4146E-05	6.9530E-04	6.6115E-04	1.3711E-04	1.3039E-04	2.1844E-02
^{23}Ne	23	0.0000E+00	0.0000E+00	0.0000E+00	0.0000E+00	0.0000E+00	0.0000E+00
^{21}Na	21	0.0000E+00	0.0000E+00	0.0000E+00	0.0000E+00	0.0000E+00	0.0000E+00
^{22}Na	22	1.6466E-10	1.6466E-10	0.0000E+00	3.2471E-11	0.0000E+00	0.0000E+00
^{23}Na	23	9.4718E-04	1.1167E-03	1.6956E-04	2.2022E-04	3.3440E-05	8.1859E-01
^{24}Na	24	1.7796E-43	1.7796E-43	0.0000E+00	3.5032E-44	0.0000E+00	0.0000E+00
^{23}Mg	23	0.0000E+00	0.0000E+00	0.0000E+00	0.0000E+00	0.0000E+00	0.0000E+00
^{24}Mg	24	-2.3440E-05	2.5913E-03	2.6147E-03	5.1099E-04	5.1565E-04	-3.9367E-03
^{25}Mg	25	1.3694E-04	4.8057E-04	3.4363E-04	9.4768E-05	6.7768E-05	1.4564E-01
^{26}Mg	26	2.4722E-04	6.4138E-04	3.9416E-04	1.2648E-04	7.7732E-05	2.1142E-01
^{27}Mg	27	0.0000E+00	0.0000E+00	0.0000E+00	0.0000E+00	0.0000E+00	0.0000E+00
^{25}Al	25	0.0000E+00	0.0000E+00	0.0000E+00	0.0000E+00	0.0000E+00	0.0000E+00
^{26}Al	26	3.8534E-06	3.8534E-06	0.0000E+00	7.5989E-07	0.0000E+00	0.0000E+00
^{26m}Al[a]	26	0.0000E+00	0.0000E+00	0.0000E+00	0.0000E+00	0.0000E+00	0.0000E+00
^{27}Al	27	1.9873E-05	3.1474E-04	2.9487E-04	6.2067E-05	5.8151E-05	2.8301E-02
^{28}Al	28	0.0000E+00	0.0000E+00	0.0000E+00	0.0000E+00	0.0000E+00	0.0000E+00
^{27}Si	27	0.0000E+00	0.0000E+00	0.0000E+00	0.0000E+00	0.0000E+00	0.0000E+00
^{28}Si	28	2.1427E-06	3.3195E-03	3.3174E-03	6.54611E-04	6.5423E-04	2.548E-04
^{29}Si	29	6.7774E-06	1.8082E-04	1.7404E-04	3.5657E-05	3.4322E-05	1.6565E-02
^{30}Si	30	7.5432E-06	1.2704E-04	1.1950E-04	2.5051E-05	2.3565E-05	2.65E-02

[a]The metastable state of ^{26}Al

Table A.2: The stellar yields computed using the updated ^{26g}Al(p,γ)^{27}Si reaction rate for the 6 $M_{\odot}$, $Z = 0.02$ model.

Species	Mass Number	Yield	$\text{Mass}_{i,\text{lost}}$	$\text{Mass}_{i,0}$	$< X(i) >$	$X_0(i)$	$\log(\frac{<X(i)>}{X_0(i)})$
^{20}Ne	20	9.0636E-06	8.2302E-03	8.2211E-03	1.6230E-03	1.6213E-03	4.5268E-04
^{21}Ne	21	-1.9880E-05	1.0748E-06	2.0955E-05	2.1195E-07	4.1325E-06	-1.2900E+00
^{22}Ne	22	3.5344E-05	6.9649E-04	6.6115E-04	1.3735E-04	1.3039E-04	2.2592E-02
^{23}Ne	23	0.0000E+00	0.0000E+00	0.0000E+00	0.0000E+00	0.0000E+00	0.0000E+00
^{21}Na	21	0.0000E+00	0.0000E+00	0.0000E+00	0.0000E+00	0.0000E+00	0.0000E+00
^{22}Na	22	1.6483E-10	1.6483E-10	0.0000E+00	3.2504E-11	0.0000E+00	0.0000E+00
^{23}Na	23	9.4681E-04	1.1164E-03	1.6956E-04	2.2015E-04	3.3440E-05	8.1845E-01
^{24}Na	24	1.6816E-43	1.6816E-43	0.0000E+00	3.3631E-44	0.0000E+00	0.0000E+00
^{23}Mg	23	0.0000E+00	0.0000E+00	0.0000E+00	0.0000E+00	0.0000E+00	0.0000E+00
^{24}Mg	24	-2.3513E-05	2.5912E-03	2.6147E-03	5.1098E-04	5.15645E-04	-3.9489E-03
^{25}Mg	25	1.3711E-04	4.8074E-04	3.4363E-04	9.4802E-05	6.7768E-05	1.4579E-01
^{26}Mg	26	2.4585E-04	6.4001E-04	3.9416E-04	1.2621E-04	7.7732E-05	2.1049E-01
^{27}Mg	27	0.0000E+00	0.0000E+00	0.0000E+00	0.0000E+00	0.0000E+00	0.0000E+00
^{25}Al	25	0.0000E+00	0.0000E+00	0.0000E+00	0.0000E+00	0.00000E+00	0.0000E+00
^{26}Al	26	3.7750E-06	3.7750E-06	0.0000E+00	7.4444E-07	0.00000E+00	0.0000E+00
^{26m}Al	26	0.0000E+00	0.0000E+00	0.0000E+00	0.0000E+00	0.0000E+00	0.0000E+00
^{27}Al	27	2.1015E-05	3.1588E-04	2.9487E-04	6.2292E-05	5.8151E-05	2.9872E-02
^{28}Al	28	0.0000E+00	0.0000E+00	0.0000E+00	0.0000E+00	0.0000E+00	0.0000E+00
^{27}Si	27	0.0000E+00	0.0000E+00	0.0000E+00	0.0000E+00	0.0000E+00	0.0000E+00
^{28}Si	28	2.7139E-06	3.3201E-03	3.3174E-03	6.5472E-04	6.5423E-04	3.2928E-04
^{29}Si	29	6.8862E-06	1.8092E-04	1.7404E-04	3.5678E-05	3.4322E-05	1.6827E-02
^{30}Si	30	7.6013E-06	1.2709E-04	1.1949E-04	2.5063E-05	2.3565E-05	2.6758E-02

Table A.3: The stellar yields computed using the updated ^{23}Na(p,α)^{20}Ne reaction rate for the 6 $M_\odot$, $Z = 0.02$ model.

Species	Mass Number	Yield	$\text{Mass}_{i,\text{lost}}$	$\text{Mass}_{i,0}$	$< X(i) >$	$X_0(i)$	$\log(\frac{<X(i)>}{X_0(i)})$
^{20}Ne	20	-2.7604E-05	8.1935E-03	8.2211E-03	1.6158E-03	1.6213E-03	-1.4866E-03
^{21}Ne	21	-1.9942E-05	1.0123E-06	2.0955E-05	1.9962E-07	4.1325E-06	-1.3160E+00
^{22}Ne	22	3.2879E-05	6.9403E-04	6.6115E-04	1.3686E-04	1.3039E-04	2.1052E-02
^{23}Ne	23	0.0000E+00	0.0000E+00	0.0000E+00	0.0000E+00	0.0000E+00	0.0000E+00
^{21}Na	21	0.0000E+00	0.0000E+00	0.0000E+00	0.0000E+00	0.0000E+00	0.0000E+00
^{22}Na	22	1.6109E-10	1.6109E-10	0.0000E+00	3.1767E-11	0.0000E+00	0.0000E+00
^{23}Na	23	9.7486E-04	1.1444E-03	1.6956E-04	2.2568E-04	3.3440E-05	8.2923E-01
^{24}Na	24	1.8918E-43	1.8918E-43	0.0000E+00	3.7835E-44	0.0000E+00	0.0000E+00
^{23}Mg	23	0.0000E+00	0.0000E+00	0.0000E+00	0.0000E+00	0.0000E+00	0.0000E+00
^{24}Mg	24	-2.1994E-05	2.5927E-03	2.6147E-03	5.1128E-04	5.1565E-04	-3.6944E-03
^{25}Mg	25	1.4105E-04	4.8468E-04	3.4363E-04	9.5579E-05	6.7768E-05	1.4934E-01
^{26}Mg	26	2.5067E-04	6.4483E-04	3.9416E-04	1.2716E-04	7.7732E-05	2.1375E-01
^{27}Mg	27	0.0000E+00	0.0000E+00	0.0000E+00	0.0000E+00	0.0000E+00	0.0000E+00
^{25}Al	25	0.0000E+00	0.0000E+00	0.0000E+00	0.0000E+00	0.0000E+00	0.0000E+00
^{26}Al	26	3.9755E-06	3.9755E-06	0.0000E+00	7.8398E-07	0.0000E+00	0.0000E+00
^{26m}Al	26	0.0000E+00	0.0000E+00	0.0000E+00	0.0000E+00	0.0000E+00	0.0000E+00
^{27}Al	27	2.4013E-05	3.1888E-04	2.9487E-04	6.2883E-05	5.8151E-05	3.3975E-02
^{28}Al	28	0.0000E+00	0.0000E+00	0.0000E+00	0.0000E+00	0.0000E+00	0.0000E+00
^{27}Si	27	0.0000E+00	0.0000E+00	0.0000E+00	0.0000E+00	0.0000E+00	0.0000E+00
^{28}Si	28	4.1791E-06	3.3216E-03	3.3174E-03	6.5501E-04	6.5423E-04	5.2091E-04
^{29}Si	29	6.9350E-06	1.8097E-04	1.7404E-04	3.5688E-05	3.4322E-05	1.6944E-02
^{30}Si	30	7.4229E-06	1.2691E-04	1.1949E-04	2.5028E-05	2.3565E-05	2.6148E-02

Table A.4: The stellar yields computed using the updated ^{23}Na(p,γ)^{24}Mg reaction rate for the 6 $M_{\odot}$, $Z = 0.02$ model.

Species	Mass Number	Yield	$\text{Mass}_{i,\text{lost}}$	$\text{Mass}_{i,0}$	$< X(i) >$	$X_0(i)$	$\log(\frac{<X(i)>}{X_0(i)})$
^{20}Ne	20	2.2841E-05	8.2440E-03	8.2211E-03	1.6257E-03	1.6213E-03	1.1790E-03
^{21}Ne	21	-1.9814E-05	1.1400E-06	2.0956E-05	2.2488E-07	4.1325E-06	-1.2644E+00
^{22}Ne	22	3.4340E-05	6.9549E-04	6.6115E-04	1.3715E-04	1.3039E-04	2.1965E-02
^{23}Ne	23	0.0000E+00	0.0000E+00	0.0000E+00	0.0000E+00	0.0000E+00	0.0000E+00
^{21}Na	21	0.0000E+00	0.0000E+00	0.0000E+00	0.0000E+00	0.0000E+00	0.0000E+00
^{22}Na	22	1.6856E-10	1.6856E-10	0.0000E+00	3.3240E-11	0.0000E+00	0.0000E+00
^{23}Na	23	9.7238E-04	1.1419E-03	1.6956E-04	2.2519E-04	3.3440E-05	8.2828E-01
^{24}Na	24	2.2841E-43	2.2841E-43	0.0000E+00	4.4842E-44	0.0000E+00	0.0000E+00
^{23}Mg	23	0.0000E+00	0.0000E+00	0.0000E+00	0.0000E+00	0.0000E+00	0.0000E+00
^{24}Mg	24	-4.9936E-05	2.5648E-03	2.6147E-03	5.0577E-04	5.1565E-04	-8.4003E-03
^{25}Mg	25	1.3238E-04	4.7601E-04	3.4363E-04	9.3869E-05	6.7768E-05	1.4150E-01
^{26}Mg	26	2.4256E-04	6.3672E-04	3.9416E-04	1.2556E-04	7.7732E-05	2.0825E-01
^{27}Mg	27	0.0000E+00	0.0000E+00	0.0000E+00	0.0000E+00	0.0000E+00	0.0000E+00
^{25}Al	25	0.0000E+00	0.0000E+00	0.0000E+00	0.0000E+00	0.0000E+00	0.0000E+00
^{26}Al	26	3.7146E-06	3.7146E-06	0.0000E+00	7.3253E-07	0.0000E+00	0.0000E+00
^{26m}Al	26	0.0000E+00	0.0000E+00	0.0000E+00	0.0000E+00	0.0000E+00	0.0000E+00
^{27}Al	27	1.5378E-05	3.1024E-04	2.9487E-04	6.1180E-05	5.8151E-05	2.2052E-02
^{28}Al	28	0.0000E+00	0.0000E+00	0.0000E+00	0.0000E+00	0.0000E+00	0.0000E+00
^{27}Si	27	0.0000E+00	0.0000E+00	0.0000E+00	0.0000E+00	0.0000E+00	0.0000E+00
^{28}Si	28	-1.6787E-07	3.3172E-03	3.3174E-03	6.5416E-04	6.5423E-04	-4.7834E-05
^{29}Si	29	6.5674E-06	1.8061E-04	1.7404E-04	3.5615E-05	3.4322E-05	1.6061E-02
^{30}Si	30	7.6454E-06	1.2714E-04	1.1949E-04	2.5071E-05	2.3565E-05	2.6909E-02

Table A.5: The standard set of stellar yields for the $6\,M_{\odot}$, $Z = 0.004$ model.

Species	Mass Number	Yield	$\text{Mass}_{i,\text{lost}}$	$\text{Mass}_{i,0}$	$< X(i) >$	$X_0(i)$	$\log(\frac{<X(i)>}{X_0(i)})$
^{20}Ne	20	2.6843E-04	1.8954E-03	1.6270E-03	3.7742E-04	3.2399E-04	6.6295E-02
^{21}Ne	21	-3.7429E-06	4.0405E-07	4.1470E-06	8.0456E-08	8.2581E-07	-1.0113E+00
^{22}Ne	22	3.1493E-05	1.6234E-04	1.3084E-04	3.2325E-05	2.6056E-05	9.3638E-02
^{23}Ne	23	0.0000E+00	0.0000E+00	0.0000E+00	0.0000E+00	0.0000E+00	0.0000E+00
^{21}Na	21	0.0000E+00	0.0000E+00	0.0000E+00	0.0000E+00	0.0000E+00	0.0000E+00
^{22}Na	22	1.8212E-10	1.8212E-10	0.0000E+00	3.6265E-11	0.0000E+00	0.0000E+00
^{23}Na	23	3.4054E-04	3.7410E-04	3.3557E-05	7.4491E-05	6.6824E-06	1.0472E+00
^{24}Na	24	3.5117E-42	3.5117E-42	0.0000E+00	6.9925E-43	0.0000E+00	0.0000E+00
^{23}Mg	23	0.0000E+00	0.0000E+00	0.0000E+00	0.0000E+00	0.0000E+00	0.0000E+00
^{24}Mg	24	-2.6761E-04	2.4985E-04	5.1745E-04	4.9751E-05	1.0304E-04	-3.1622E-01
^{25}Mg	25	7.1106E-04	7.7907E-04	6.8005E-05	1.5513E-04	1.3542E-05	1.0590E+00
^{26}Mg	26	6.3200E-04	7.1001E-04	7.8005E-05	1.4138E-04	1.5534E-05	9.5912E-01
^{27}Mg	27	0.0000E+00	0.0000E+00	0.0000E+00	0.0000E+00	0.0000E+00	0.0000E+00
^{25}Al	25	0.0000E+00	0.0000E+00	0.0000E+00	0.0000E+00	0.0000E+00	0.0000E+00
^{26}Al	26	4.6810E-05	4.6810E-05	0.0000E+00	9.3211E-06	0.0000E+00	0.0000E+00
^{26m}Al	26	0.0000E+00	0.0000E+00	0.0000E+00	0.0000E+00	0.0000E+00	0.0000E+00
^{27}Al	27	2.9174E-05	8.7528E-05	5.8355E-05	1.7429E-05	1.1621E-05	1.7605E-01
^{28}Al	28	0.0000E+00	0.0000E+00	0.0000E+00	0.0000E+00	0.0000E+00	0.0000E+00
^{27}Si	27	0.0000E+00	0.0000E+00	0.0000E+00	0.0000E+00	0.0000E+00	0.0000E+00
^{28}Si	28	2.3615E-05	6.8014E-04	6.5652E-04	1.3543E-04	1.3074E-04	1.5321E-02
^{29}Si	29	1.1800E-05	4.6243E-05	3.4443E-05	9.2080E-06	6.8588E-06	1.2792E-01
^{30}Si	30	1.2729E-05	3.6376E-05	2.3648E-05	7.2434E-06	4.7091E-06	1.8700E-01

Table A.6: The stellar yields computed using the updated ^{26g}Al(p,γ)^{27}Si reaction rate for the 6 $M_{\odot}$, $Z = 0.004$ model.

Species	Mass Number	Yield	$\text{Mass}_{i,\text{lost}}$	$\text{Mass}_{i,0}$	$< X(i) >$	$X_0(i)$	$\log(\frac{<X(i)>}{X_0(i)})$
^{20}Ne	20	2.6866E-04	1.8957E-03	1.6270E-03	3.7747E-04	3.2399E-04	6.6348E-02
^{21}Ne	21	-3.7428E-06	4.0415E-07	4.1470E-06	8.0477E-08	8.2581E-07	-1.0112E+00
^{22}Ne	22	3.1602E-05	1.6245E-04	1.3084E-04	3.2347E-05	2.6056E-05	9.3928E-02
^{23}Ne	23	0.0000E+00	0.0000E+00	0.0000E+00	0.0000E+00	0.0000E+00	0.0000E+00
^{21}Na	21	0.0000E+00	0.0000E+00	0.0000E+00	0.0000E+00	0.0000E+00	0.0000E+00
^{22}Na	22	1.8218E-10	1.8218E-10	0.0000E+00	3.6277E-11	0.0000E+00	0.0000E+00
^{23}Na	23	3.4109E-04	3.7465E-04	3.3557E-05	7.4601E-05	6.6824E-06	1.0478E+00
^{24}Na	24	-3.1470E-41	-3.1470E-41	0.0000E+00	-6.2666E-42	0.0000E+00	0.0000E+00
^{23}Mg	23	0.0000E+00	0.0000E+00	0.0000E+00	0.0000E+00	0.0000E+00	0.0000E+00
^{24}Mg	24	-2.6742E-04	2.5004E-04	5.1745E-04	4.9788E-05	1.0304E-04	-3.1590E-01
^{25}Mg	25	7.1112E-04	7.7912E-04	6.8005E-05	1.5514E-04	1.3542E-05	1.0590E+00
^{26}Mg	26	6.3204E-04	7.1005E-04	7.8005E-05	1.4139E-04	1.5534E-05	9.5914E-01
^{27}Mg	27	0.0000E+00	0.0000E+00	0.0000E+00	0.0000E+00	0.0000E+00	0.0000E+00
^{25}Al	25	0.0000E+00	0.0000E+00	0.0000E+00	0.0000E+00	0.0000E+00	0.0000E+00
^{26}Al	26	4.6511E-05	4.6511E-05	0.0000E+00	9.2614E-06	0.0000E+00	0.0000E+00
^{26m}Al	26	0.0000E+00	0.0000E+00	0.0000E+00	0.0000E+00	0.0000E+00	0.0000E+00
^{27}Al	27	2.9510E-05	8.7864E-05	5.8355E-05	1.7496E-05	1.1621E-05	1.7771E-01
^{28}Al	28	0.0000E+00	0.0000E+00	0.0000E+00	0.0000E+00	0.0000E+00	0.0000E+00
^{27}Si	27	0.0000E+00	0.0000E+00	0.0000E+00	0.0000E+00	0.0000E+00	0.0000E+00
^{28}Si	28	2.3618E-05	6.8014E-04	6.5652E-04	1.3543E-04	1.3074E-04	1.5323E-02
^{29}Si	29	1.1798E-05	4.6240E-05	3.4443E-05	9.2076E-06	6.8588E-06	1.2790E-01
^{30}Si	30	1.2726E-05	3.6374E-05	2.3648E-05	7.2429E-06	4.7091E-06	1.8697E-01

Table A.7: The stellar yields computed using the updated ^{23}Na(p,α)^{20}Ne reaction rate for the 6 $M_{\odot}$, $Z = 0.004$ model.

Species	Mass Number	Yield	$\text{Mass}_{i,\text{lost}}$	$\text{Mass}_{i,0}$	$< X(i) >$	$X_0(i)$	$\log(\frac{<X(i)>}{X_0(i)})$
^{20}Ne	20	-2.5287E-05	1.6017E-03	1.6270E-03	3.1894E-04	3.2399E-04	-6.8291E-03
^{21}Ne	21	-3.7838E-06	3.6313E-07	4.1470E-06	7.2307E-08	8.2581E-07	-1.0577E+00
^{22}Ne	22	3.1373E-05	1.6222E-04	1.3084E-04	3.2301E-05	2.6056E-05	9.3317E-02
^{23}Ne	23	0.0000E+00	0.0000E+00	0.0000E+00	0.0000E+00	0.0000E+00	0.0000E+00
^{21}Na	21	0.0000E+00	0.0000E+00	0.0000E+00	0.0000E+00	0.0000E+00	0.0000E+00
^{22}Na	22	1.5691E-10	1.5691E-10	0.0000E+00	3.1244E-11	0.0000E+00	0.0000E+00
^{23}Na	23	5.2003E-04	5.5359E-04	3.3557E-05	1.1023E-04	6.6824E-06	1.2174E+00
^{24}Na	24	2.0473E-42	2.0473E-42	0.0000E+00	4.0778E-43	0.0000E+00	0.0000E+00
^{23}Mg	23	0.0000E+00	0.0000E+00	0.0000E+00	0.0000E+00	0.0000E+00	0.0000E+00
^{24}Mg	24	-1.8011E-04	3.3735E-04	5.1745E-04	6.7174E-05	1.0304E-04	-1.8582E-01
^{25}Mg	25	7.7239E-04	8.4040E-04	6.8005E-05	1.6734E-04	1.3542E-05	1.0919E+00
^{26}Mg	26	6.3109E-04	7.0909E-04	7.8005E-05	1.4120E-04	1.5534E-05	9.5856E-01
^{27}Mg	27	0.0000E+00	0.0000E+00	0.0000E+00	0.0000E+00	0.0000E+00	0.0000E+00
^{25}Al	25	0.0000E+00	0.0000E+00	0.0000E+00	0.0000E+00	0.0000E+00	0.0000E+00
^{26}Al	26	4.9393E-05	4.9393E-05	0.0000E+00	9.8353E-06	0.0000E+00	0.0000E+00
^{26m}Al	26	0.0000E+00	0.0000E+00	0.0000E+00	0.0000E+00	0.0000E+00	0.0000E+00
^{27}Al	27	3.1573E-05	8.9928E-05	5.8355E-05	1.7907E-05	1.1621E-05	1.8779E-01
^{28}Al	28	0.0000E+00	0.0000E+00	0.0000E+00	0.0000E+00	0.0000E+00	0.0000E+00
^{27}Si	27	0.0000E+00	0.0000E+00	0.0000E+00	0.0000E+00	0.0000E+00	0.0000E+00
^{28}Si	28	3.5094E-05	6.9162E-04	6.5652E-04	1.3772E-04	1.3074E-04	2.2590E-02
^{29}Si	29	1.4983E-05	4.9426E-05	3.4443E-05	9.8419E-06	6.8588E-06	1.5683E-01
^{30}Si	30	1.4830E-05	3.8478E-05	2.3648E-05	7.6618E-06	4.7091E-06	2.1139E-01

Table A.8: The stellar yields computed using the updated ^{23}Na(p,γ)^{24}Mg reaction rate for the 6 $M_\odot$, $Z = 0.004$ model.

Species	Mass Number	Yield	$\text{Mass}_{i,\text{lost}}$	$\text{Mass}_{i,0}$	$< X(i) >$	$X_0(i)$	$\log(\frac{<X(i)>}{X_0(i)})$
^{20}Ne	20	3.8765E-04	2.0146E-03	1.6270E-03	4.0116E-04	3.2399E-04	9.2786E-02
^{21}Ne	21	-3.7031E-06	4.4389E-07	4.1470E-06	8.8388E-08	8.2581E-07	-9.7048E-01
^{22}Ne	22	3.1455E-05	1.6230E-04	1.3084E-04	3.2318E-05	2.6056E-05	9.3537E-02
^{23}Ne	23	0.0000E+00	0.0000E+00	0.0000E+00	0.0000E+00	0.0000E+00	0.0000E+00
^{21}Na	21	0.0000E+00	0.0000E+00	0.0000E+00	0.0000E+00	0.0000E+00	0.0000E+00
^{22}Na	22	1.9777E-10	1.9777E-10	0.0000E+00	3.9381E-11	0.0000E+00	0.0000E+00
^{23}Na	23	4.5670E-04	4.9026E-04	3.3557E-05	9.7622E-05	6.6824E-06	1.1646E+00
^{24}Na	24	-5.4511E-43	-5.4511E-43	0.0000E+00	-1.0790E-43	0.0000E+00	0.0000E+00
^{23}Mg	23	0.0000E+00	0.0000E+00	0.0000E+00	0.0000E+00	0.0000E+00	0.0000E+00
^{24}Mg	24	-4.0468E-04	1.1285E-04	5.1745E-04	2.2471E-05	1.0304E-04	-6.6139E-01
^{25}Mg	25	6.0267E-04	6.7068E-04	6.8005E-05	1.3355E-04	1.3542E-05	9.9395E-01
^{26}Mg	26	6.3135E-04	7.0935E-04	7.8005E-05	1.4125E-04	1.5534E-05	9.5871E-01
^{27}Mg	27	0.0000E+00	0.0000E+00	0.0000E+00	0.0000E+00	0.0000E+00	0.0000E+00
^{25}Al	25	0.0000E+00	0.0000E+00	0.0000E+00	0.0000E+00	0.0000E+00	0.0000E+00
^{26}Al	26	4.1380E-05	4.1380E-05	0.0000E+00	8.2397E-06	0.0000E+00	0.0000E+00
^{26m}Al	26	0.0000E+00	0.0000E+00	0.0000E+00	0.0000E+00	0.0000E+00	0.0000E+00
^{27}Al	27	2.6476E-05	8.4837E-05	5.8355E-05	1.6892E-05	1.1621E-05	1.6245E-01
^{28}Al	28	0.0000E+00	0.0000E+00	0.0000E+00	0.0000E+00	0.0000E+00	0.0000E+00
^{27}Si	27	0.0000E+00	0.0000E+00	0.0000E+00	0.0000E+00	0.0000E+00	0.0000E+00
^{28}Si	28	1.3059E-05	6.6958E-04	6.5652E-04	1.3333E-04	1.3074E-04	8.5280E-03
^{29}Si	29	8.8863E-06	4.3329E-05	3.4443E-05	8.6278E-06	6.8588E-06	9.9655E-02
^{30}Si	30	1.0739E-05	3.4387E-05	2.3648E-05	6.8472E-06	4.7091E-06	1.6257E-01

Table A.9: The standard set of stellar yields for the $6\,M_{\odot}$, $Z = 0.008$ model.

Species	Mass Number	Yield	$\text{Mass}_{i,\text{lost}}$	$\text{Mass}_{i,0}$	$< X(i) >$	$X_0(i)$	$\log(\frac{<X(i)>}{X_0(i)})$
^{20}Ne	20	2.0673E-04	3.4815E-03	3.2747E-03	6.8899E-04	6.4812E-04	2.6559E-02
^{21}Ne	21	-7.8574E-06	4.8947E-07	8.3468E-06	9.6868E-08	1.6520E-06	-1.2318E+00
^{22}Ne	22	-2.1907E-05	2.4145E-04	2.6336E-04	4.7784E-05	5.2122E-05	-3.7743E-02
^{23}Ne	23	0.0000E+00	0.0000E+00	0.0000E+00	0.0000E+00	0.0000E+00	0.0000E+00
^{21}Na	21	0.0000E+00	0.0000E+00	0.0000E+00	0.0000E+00	0.0000E+00	0.0000E+00
^{22}Na	22	1.6453E-10	1.6453E-10	0.0000E+00	3.2561E-11	0.0000E+00	0.0000E+00
^{23}Na	23	6.0518E-04	6.7272E-04	6.7543E-05	1.3313E-04	1.3368E-05	9.9823E-01
^{24}Na	24	-2.9443E-39	-2.9443E-39	0.0000E+00	-5.8269E-40	0.0000E+00	0.0000E+00
^{23}Mg	23	0.0000E+00	0.0000E+00	0.0000E+00	0.0000E+00	0.0000E+00	0.0000E+00
^{24}Mg	24	-9.9317E-05	9.4220E-04	1.0415E-03	1.8646E-04	2.0613E-04	-4.3549E-02
^{25}Mg	25	5.2152E-04	6.5840E-04	1.3688E-04	1.3030E-04	2.7090E-05	6.8212E-01
^{26}Mg	26	4.8074E-04	6.3775E-04	1.5701E-04	1.2621E-04	3.1074E-05	6.0871E-01
^{27}Mg	27	0.0000E+00	0.0000E+00	0.0000E+00	0.0000E+00	0.0000E+00	0.0000E+00
^{25}Al	25	0.0000E+00	0.0000E+00	0.0000E+00	0.0000E+00	0.0000E+00	0.0000E+00
^{26}Al	26	2.0624E-05	2.0624E-05	0.0000E+00	4.0815E-06	0.0000E+00	0.0000E+00
^{26m}Al	26	0.0000E+00	0.0000E+00	0.0000E+00	0.0000E+00	0.0000E+00	0.0000E+00
^{27}Al	27	2.4752E-05	1.4221E-04	1.1745E-04	2.8143E-05	2.3246E-05	8.3023E-02
^{28}Al	28	0.0000E+00	0.0000E+00	0.0000E+00	0.0000E+00	0.0000E+00	0.0000E+00
^{27}Si	27	0.0000E+00	0.0000E+00	0.0000E+00	0.0000E+00	0.0000E+00	0.0000E+00
^{28}Si	28	2.1494E-05	1.3429E-03	1.3214E-03	2.6577E-04	2.6153E-04	6.9814E-03
^{29}Si	29	1.2978E-05	8.2303E-05	6.9325E-05	1.6288E-05	1.3720E-05	7.4499E-02
^{30}Si	30	1.3227E-05	6.0824E-05	4.7597E-05	1.2037E-05	9.4202E-06	1.0647E-01

Table A.10: The stellar yields computed using the updated ^{26g}Al(p,γ)^{27}Si reaction rate for the 6 $M_{\odot}$, $Z = 0.008$ model.

Species	Mass Number	Yield	$\text{Mass}_{i,\text{lost}}$	$\text{Mass}_{i,0}$	$< X(i) >$	$X_0(i)$	$\log(\frac{<X(i)>}{X_0(i)})$
^{20}Ne	20	2.0581E-04	3.4805E-03	3.2747E-03	6.8881E-04	6.4812E-04	2.6445E-02
^{21}Ne	21	-7.8562E-06	4.9060E-07	8.3468E-06	9.7091E-08	1.6520E-06	-1.2308E+00
^{22}Ne	22	-2.1487E-05	2.4187E-04	2.6336E-04	4.7867E-05	5.2122E-05	-3.6989E-02
^{23}Ne	23	0.0000E+00	0.0000E+00	0.0000E+00	0.0000E+00	0.0000E+00	0.0000E+00
^{21}Na	21	0.0000E+00	0.0000E+00	0.0000E+00	0.0000E+00	0.0000E+00	0.0000E+00
^{22}Na	22	1.6447E-10	1.6447E-10	0.0000E+00	3.2550E-11	0.0000E+00	0.0000E+00
^{23}Na	23	6.0421E-04	6.7175E-04	6.7543E-05	1.3294E-04	1.3368E-05	9.9760E-01
^{24}Na	24	4.4131E-40	4.4131E-40	0.0000E+00	8.7336E-41	0.0000E+00	0.0000E+00
^{23}Mg	23	0.0000E+00	0.0000E+00	0.0000E+00	0.0000E+00	0.0000E+00	0.0000E+00
^{24}Mg	24	-1.0013E-04	9.4139E-04	1.0415E-03	1.8630E-04	2.0613E-04	-4.3924E-02
^{25}Mg	25	5.2121E-04	6.5809E-04	1.3688E-04	1.3024E-04	2.7090E-05	6.8192E-01
^{26}Mg	26	4.7995E-04	6.3696E-04	1.5701E-04	1.2605E-04	3.1074E-05	6.0817E-01
^{27}Mg	27	0.0000E+00	0.0000E+00	0.0000E+00	0.0000E+00	0.0000E+00	0.0000E+00
^{25}Al	25	0.0000E+00	0.0000E+00	0.0000E+00	0.0000E+00	0.0000E+00	0.0000E+00
^{26}Al	26	2.0497E-05	2.0497E-05	0.0000E+00	4.0563E-06	0.0000E+00	0.0000E+00
^{26m}Al	26	0.0000E+00	0.0000E+00	0.0000E+00	0.0000E+00	0.0000E+00	0.0000E+00
^{27}Al	27	2.4882E-05	1.4234E-04	1.1745E-04	2.8169E-05	2.3246E-05	8.3421E-02
^{28}Al	28	0.0000E+00	0.0000E+00	0.0000E+00	0.0000E+00	0.0000E+00	0.0000E+00
^{27}Si	27	0.0000E+00	0.0000E+00	0.0000E+00	0.0000E+00	0.0000E+00	0.0000E+00
^{28}Si	28	2.1588E-05	1.3430E-03	1.3214E-03	2.6578E-04	2.6153E-04	7.0117E-03
^{29}Si	29	1.2989E-05	8.2314E-05	6.9325E-05	1.6290E-05	1.3720E-05	7.4558E-02
^{30}SI	30	1.3231E-05	6.0829E-05	4.7597E-05	1.2038E-05	9.4202E-06	1.0650E-01

Table A.11: The stellar yields computed using the updated ^{23}Na(p,α)^{20}Ne reaction rate for the 6 $M_{\odot}$, $Z = 0.008$ model.

Species	Mass Number	Yield	$\text{Mass}_{i,\text{lost}}$	$\text{Mass}_{i,0}$	$< X(i) >$	$X_0(i)$	$\log(\frac{<X(i)>}{X_0(i)})$
^{20}Ne	20	-3.7031E-05	3.2377E-03	3.2747E-03	6.4075E-04	6.4812E-04	-4.9650E-03
^{21}Ne	21	-7.9046E-06	4.4224E-07	8.3468E-06	8.7519E-08	1.6520E-06	-1.2759E+00
^{22}Ne	22	-2.2187E-05	2.4117E-04	2.6336E-04	4.7728E-05	5.2122E-05	-3.8248E-02
^{23}Ne	23	0.0000E+00	0.0000E+00	0.0000E+00	0.0000E+00	0.0000E+00	0.0000E+00
^{21}Na	21	0.0000E+00	0.0000E+00	0.0000E+00	0.0000E+00	0.0000E+00	0.0000E+00
^{22}Na	22	1.5134E-10	1.5134E-10	0.0000E+00	2.9951E-11	0.0000E+00	0.0000E+00
^{23}Na	23	8.1191E-04	8.7946E-04	6.7543E-05	1.7405E-04	1.3368E-05	1.1146E+00
^{24}Na	24	-1.4186E-39	-1.4186E-39	0.0000E+00	-2.8075E-40	0.0000E+00	0.0000E+00
^{23}Mg	23	0.0000E+00	0.0000E+00	0.0000E+00	0.0000E+00	0.0000E+00	0.0000E+00
^{24}Mg	24	-5.1211E-05	9.9030E-04	1.0415E-03	1.9598E-04	2.0613E-04	-2.1923E-02
^{25}Mg	25	5.3212E-04	6.6900E-04	1.3688E-04	1.3240E-04	2.7090E-05	6.8906E-01
^{26}Mg	26	4.8141E-04	6.3842E-04	1.5701E-04	1.2634E-04	3.1074E-05	6.0917E-01
^{27}Mg	27	0.0000E+00	0.0000E+00	0.0000E+00	0.0000E+00	0.0000E+00	0.0000E+00
^{25}Al	25	0.0000E+00	0.0000E+00	0.0000E+00	0.0000E+00	0.0000E+00	0.0000E+00
^{26}Al	26	2.0873E-05	2.0873E-05	0.0000E+00	4.1307E-06	0.0000E+00	0.0000E+00
^{26m}Al	26	0.0000E+00	0.0000E+00	0.0000E+00	0.0000E+00	0.0000E+00	0.0000E+00
^{27}Al	27	3.1130E-05	1.4858E-04	1.1745E-04	2.9405E-05	2.3246E-05	1.0208E-01
^{28}Al	28	0.0000E+00	0.0000E+00	0.0000E+00	0.0000E+00	0.0000E+00	0.0000E+00
^{27}Si	27	0.0000E+00	0.0000E+00	0.0000E+00	0.0000E+00	0.0000E+00	0.0000E+00
^{28}Si	28	3.2401E-05	1.3538E-03	1.3214E-03	2.6792E-04	2.6153E-04	1.0495E-02
^{29}Si	29	1.5425E-05	8.4750E-05	6.9325E-05	1.6772E-05	1.3720E-05	8.7222E-02
^{30}SI	30	1.4350E-05	6.1948E-05	4.7597E-05	1.2260E-05	9.4202E-06	1.1442E-01

Table A.12: The stellar yields computed using the updated ^{23}Na(p,γ)^{24}Mg reaction rate for the 6 $M_{\odot}$, $Z = 0.008$ model.

Species	Mass Number	Yield	$\text{Mass}_{i,\text{lost}}$	$\text{Mass}_{i,0}$	$< X(i) >$	$X_0(i)$	$\log(\frac{<X(i)>}{X_0(i)})$
^{20}Ne	20	2.6790E-04	3.5426E-03	3.2747E-03	7.0110E-04	6.4812E-04	3.4124E-02
^{21}Ne	21	-7.8067E-06	5.4014E-07	8.3468E-06	1.0690E-07	1.6520E-06	-1.1890E+00
^{22}Ne	22	-2.1960E-05	2.4140E-04	2.6336E-04	4.7773E-05	5.2122E-05	-3.7838E-02
^{23}Ne	23	0.0000E+00	0.0000E+00	0.0000E+00	0.0000E+00	0.0000E+00	0.0000E+00
^{21}Na	21	0.0000E+00	0.0000E+00	0.0000E+00	0.0000E+00	0.0000E+00	0.0000E+00
^{22}Na	22	1.7236E-10	1.7236E-10	0.0000E+00	3.4110E-11	0.0000E+00	0.0000E+00
^{23}Na	23	7.7091E-04	8.3845E-04	6.7543E-05	1.6593E-04	1.3368E-05	1.0939E+00
^{24}Na	24	-2.0071E-39	-2.0071E-39	0.0000E+00	-3.9721E-40	0.0000E+00	0.0000E+00
^{23}Mg	23	0.0000E+00	0.0000E+00	0.0000E+00	0.0000E+00	0.0000E+00	0.0000E+00
^{24}Mg	24	-2.9255E-04	7.4896E-04	1.0415E-03	1.4822E-04	2.0613E-04	-1.4323E-01
^{25}Mg	25	4.8513E-04	6.2201E-04	1.3688E-04	1.2310E-04	2.7090E-05	6.5743E-01
^{26}Mg	26	4.7887E-04	6.3587E-04	1.5701E-04	1.2584E-04	3.1074E-05	6.0743E-01
^{27}Mg	27	0.0000E+00	0.0000E+00	0.0000E+00	0.0000E+00	0.0000E+00	0.0000E+00
^{25}Al	25	0.0000E+00	0.0000E+00	0.0000E+00	0.0000E+00	0.0000E+00	0.0000E+00
^{26}Al	26	1.9767E-05	1.9767E-05	0.0000E+00	3.9119E-06	0.0000E+00	0.0000E+00
^{26m}Al	26	0.0000E+00	0.0000E+00	0.0000E+00	0.0000E+00	0.0000E+00	0.0000E+00
^{27}Al	27	1.8697E-05	1.3615E-04	1.1745E-04	2.6945E-05	2.3246E-05	6.4127E-02
^{28}Al	28	0.0000E+00	0.0000E+00	0.0000E+00	0.0000E+00	0.0000E+00	0.0000E+00
^{27}Si	27	0.0000E+00	0.0000E+00	0.0000E+00	0.0000E+00	0.0000E+00	0.0000E+00
^{28}Si	28	1.1369E-05	1.3328E-03	1.3214E-03	2.6376E-04	2.6153E-04	3.6948E-03
^{29}Si	29	1.0641E-05	7.9966E-05	6.9325E-05	1.5825E-05	1.3720E-05	6.1988E-02
^{30}Si	30	1.2086E-05	5.9683E-05	4.7597E-05	1.1811E-05	9.4202E-06	9.8241E-02

Bibliography

[1] Bethe H. A. and Critchfield C. L. *Phys. Rev.*, 54:248, 1938.

[2] Weizsäcker C. F. von. *Physik. Zeits.*, 38:176, 1937.

[3] Claus E. Rolfs and William S. Rodney. *Cauldrons in the Cosmos.* The University of Chicago Press, 1988.

[4] Burbidge E. M., Burbidge G. R., Fowler W. A., and Hoyle F. *Rev.Mod.Phys.*, 29:547–650, 1957.

[5] Alan A. Chen. PhD thesis, Yale University, U.S.A, 1999.

[6] Gehrz R. D., Truran J. W., Williams R. E., and Starrfield S. *Publications of the Astronomical Society of the Pacific*, 110:3, 1998.

[7] Herwig F. AGB stars evolution and nucleosynthesis. In *Proceedings of the International Symposium on Nuclear Astrophysics-Nuclei in the Cosmos-IX*, CERN, Switzerland, June 2006.

[8] Lattanzio J. C. *New Astronomy Rev.*, 46:469–474, 2002.

[9] Wiescher M., Görres J., and Schatz H. *Journal of Physics G: Nuclear and Particle Physics*, 25:133, 1999.

[10] Iben I. Jr. and Renzini A. *Ann. Rev. Astron. Astrophys.*, 21:271–342, 1983.

[11] Vassiliadis E. and Wood P. R. *The Astrophysical J.*, 413:641–657, 1993.

[12] Lattanzio J. C. and Frost C. A. *The Astrophysical J.*, 473:383–387, 1996.

[13] Herwig F., Blöcker T., Schonberner D., and El Eid M.F. *Astron. & Astrophys.*, 324:L81, 1997.

[14] Blöcker T. *Astrophysics and Space Science*, 275:1–14, 2001.

[15] Amanda I. Karakas. PhD thesis, School of Mathematics & Statistics, Monash University, Australia, 2003.

[16] Harm J Habing and Hans Olofsson (Editors). *Asymptotic Giant Branch Stars.* Springer, 2004.

[17] Herwig F. *Annu. Rev. Astron. Astrophys.*, 43:435–479, 2005.

[18] Herwig F. (arXiv:astro-ph/0007139), 2000.

[19] *Post-Main Sequence Stars.* Website, 2006. `http://outreach.atnf.csiro.au/education/senior/astrophysics/stellarevolution_postmain.html`.

[20] Marigo P. (arXiv:astro-ph/0702711), 2007.

[21] Bernard E. J. Pagel. *Nucleosynthesis and Chemical Evolution of Galaxies.* Cambridge University Press, 1997.

[22] Pols O. R., Tout C. A., Lattanzio J. C., and Karakas A. I. Thermal pulses and dredge-up in AGB stars. In *Evolution of Binary and Multiple Star Systems*, 2001. APS Conference Series, Vol. 229.

[23] Iben I. Jr. *The Astrophysical J.*, 196:525–547, 1975.

[24] Uberseder E., Heil M., Käppeler F., Görres J., and Wiescher M. *Phys. Rev. C*, 75:035801, 2007.

[25] Karakas A. I., Lugaro M. A., Wiescher M., Görres J., and Ugalde C. *The Astrophysical J.*, 643:471–483, 2006.

[26] Lattanzio J. C. (arXiv:astro-ph/9810094), 1998.

[27] Smith V. V., Plez B., and Lambert D. A. *The Astrophysical J.*, 441:735–746, 1995.

[28] Smith V. V. and Lambert D. A. *Astrophys. J. Suppl. Ser.*, 72:387–416, 1990.

[29] Mowlavi N. and Meynet G. *Astron. & Astrophys.*, 361:959, 2000.

[30] Donald D. Clayton. *Principles of Stellar Evolution and Nucleosynthesis.* The University of Chicago Press, 1983.

[31] Decressin T., Meynet G., Charbonnel C., Prantzos N., and Ekström S. (arXiv:astro-ph/0611379), 2006.

[32] Izzard R. G., Lugaro M., Iliadis C., and Karakas A. I. Reaction rate uncertainties: NeNa and MgAl in AGB stars. In *Proceedings of the International Symposium on Nuclear Astrophysics-Nuclei in the Cosmos-IX*, CERN, Switzerland, June 2006.

[33] Görres J., Wiescher M., and Rolfs C. *The Astrophysical J.*, 343:365–368, 1989.

[34] Bizzaro M., Baker J. A., and Haack H. *Nature*, 431:275–278, 2002.

[35] Izzard R. G., Lugaro M., Karakas A. I., Iliadis C., and Raai M. van. *Astron. & Astrophys.*, 466:641, 2007.

[36] Karakas A. I. and Lattanzio J. C. *Publications of the Astronomical Society of Australia*, 20:279–293, 2003. (arXiv:astro-ph/0305011).

[37] Marigo P. *Astron. & Astrophys.*, 387:507–519, 2002.

[38] Piovan L., Tantalo R., and Chiosi C. (arXiv:astro-ph/0306583), 2003.

[39] Gilman R. C. *The Astrophysical J.*, 178:423, 1972.

[40] Christian Iliadis. *Nuclear Physics of Stars.* Wiley-VCH, 2007.

[41] Croat T. K., Stadermann F. J., and Bernatowicz T. J. *The Astrophysical J.*, 631:976–987, 2005.

[42] Lugaro M. and Höfner S. What can presolar grains tell us about AGB stars. In *Highlights of Astronomy XXVIth General Assembly of the IAU*, 2006. Vol. 14 K. A. van der Hucht, ed.

[43] Lugaro M., Davis A. M., Gallino R., Pellin M. J., Straniero O., and Käppeler F. *The Astrophysical J.*, 593:486–508, 2003.

[44] Yong D., Grundahl F., Lambert D. L., Nissen P.E., and Shetrone M.D. *Astronomy and Astrophysics*, 402:985, 2003.

[45] Kippenhahn and Weigert A. *Stellar Structure and Evolution.* Springer-Verlag Berlin Heidelberg, 1990.

[46] Gamow von G. *Z. Phys.*, 51:204–212, 1928.

[47] Atkinson R. and Houtermans F. *Z. Phys.*, 54:656–665, 1929.

[48] Bethe H. A. and Critchfield C. L. *Phys. Rev.*, 54:248, 1938.

[49] Bethe H. A. *Phys. Rev.*, 55:436, 1939.

[50] Weizsäcker C. F. von. *Physik Z.*, 39:633, 1938.

[51] Shawn Bishop. PhD thesis, Simon Fraser University, Canada, August 2003.

[52] David J. Griffiths. *Introduction to Quantum Mechanics.* Prentice Hall, 1995.

[53] Haubould H. J. and Mathai A. M. *Astrophysics and Space Science*, 127:45–53, 1986.

[54] Mitler H. E. *The Astrophysical J.*, 212:513, 1977.

[55] Henry R. B. C. (arXiv:astro-ph/0305513), 2003.

[56] Hirschi R., Meynet G., and Maeder A. *Astron. & Astrophys.*, 433:1013–1022, 2005.

[57] Meynet G. and Maeder A. *Astron. & Astrophys.*, 390:561, 2002.

[58] Marigo P. *Astron. & Astrophys.*, 370:194–217, 2001.

[59] Frost C. A. and Lattanzio J. C. *The Astrophysical J.*, 473:383, 1986.

[60] Lattanzio J. C. *The Astrophysical J.*, 311:708, 1986.

[61] Wood P. R. and Zarro D. M. *The Astrophysical J.*, 248:311, 1981.

[62] Henyey L. G., Wilets L., Bohm K., Leverrier R., and Levee R. D. *Astrophys. J*, 316:294, 1959.

[63] Hoppe P., Amari S., Zinner E., Ireland T., and Lewis R. S. *The Astrophysical J.*, 430:870, 1994.

[64] Lugaro M., Ugalde C., Karakas A. I., Görres J., Wiescher M., Lattanzio J. C., and Cannon R. C. *The Astrophysical J.*, 615:934–946, 2004.

[65] Ben Messenger. PhD thesis, School of Mathematics & Statistics, Monash University, Australia, 2002.

[66] Maria Lugaro. PhD thesis, Monash University, Australia, February 2001.

[67] Izzard R. G., Tout C. A., Karakas A. I., and Pols O. R. *Mon. Not. R. Astron. Soc.*, 350:407–426, 2004.

[68] Höfner S. (arXiv:astro-ph/0702444), 2007.

[69] Stancliffe R. J. and Jeffery C. S. *Mon. Not. R. Astron. Soc.*, 375:1280–1290, 2007.

[70] Cannon R. C. *MNRAS*, 263:817, 1993.

[71] Caughlan G. R. and Fowler W. A. *Atom. Data Nucl. Data Tables*, 40:283, 1988.

[72] Thielemann F. *et al. Adv. Nucl. Astrophys.*, 525, 1987.

[73] Hale S. E., Champagne A. E., Iliadis C., Hansper V. Y., Powel D. C., and Blackmon J. C. *Phys. Rev. C*, 70:045802, 2004.

[74] Kenneth S. Krane. *Introductory Nuclear Physics.* John Wiley and Sons, Inc., 1988.

[75] Angulo C. *et al. Nucl. Phys. A*, 656:3–187, 1999.

[76] Iliadis C., Champagne A. E., and José J. *J. Phys. G: Nucl. Part. Phys.*, 31:S1785–S1789, 2005.

[77] Philip R. Bevington and D. Keith Robinson. *Data Reduction and Error Analysis for the Physical Sciences.* McGraw-Hill, New York, third edition, 2003.

[78] Arnould M., Goriely S., and Jorissen A. *Astron. & Astrophys.*, 347:572–582, 1999.

[79] Rowland C., Iliadis C., Champagne A. E., Fox C., José J., and Runkle R. *The Astrophysical J.*, 615:L37, 2004.

[80] Diehl R. *et al. Astron. Astrophys.*, 298:445–460, 1995.

[81] Knödlseder J., Dixon D., and Bloemen H. *et al. Astron. & Astrophys.*, 345:813, 1998.

[82] Plüschke S., Diehl R., and Schönfelder V. *et al. ESA-SP*, 459:55, 2001.

[83] Naya J. E. *et al. Nature*, 384:44–46, 1996.

[84] Diehl R. *et al. Astron. & Astrophys.*, 411:L451, 2003. and references therein.

[85] Diehl R. *New Astronomy Reviews*, 50:534–539, 2006.

[86] Smith D. *The Astrophysical J.*, 589:L55, 2003.

[87] Ruiz C. *et al. Phys. Rev. Lett.*, 96:252501, 2006.

[88] Champagne A. E. *et al. Nucl. Phys. A*, 556:123, 1993.

[89] Bradley W. Carrol and Dale A. Ostlie. *An Introduction to Modern Astrophysics.* Addison-Wesley Publishing Company, Inc., 1996.

[90] Gratton R., Sneden C., and Carretta E. *Annu. Rev. Astron. Astrophys.*, 42:385–440, 2004.

[91] Charbonnel C. and Prantzos N. (arXiv:astro-ph/0606220), 2006.

[92] Gavilán M., Mollá M., and Buell J. F. *Astron. & Astrophys.*, 450:509–521, 2006.

[93] José J. and Hernanz M. *Eur. Phys. J. A*, 27,s01:107–115, 2006.

[94] José J., Hernanz M., García-Berro E., and Gil-Pons P. Classical vs. Primordial Nova Explosions. In *Proceedings of the International Symposium on Nuclear Astrophysics-Nuclei in the Cosmos-IX*, CERN, Geneva, Switzerland, 25 - 30 June 2006.

[95] Gil-Pons P., García-Berro E., José J., Hernanz M., and Truran J. W. *Astron. & Astrophys.*, 407:1021, 2003.

[96] *Anatomy of the Classical Nova Outburst.* Website. `http://observe.arc.nasa.gov/nasa/space/stellardeath/stellardeath_4a2.html`.

[97] José J., García-Berro E., Hernanz M., and Gil-Pons P. *The Astrophysical J.*, 662:L103–L106, 2007.

[98] Gil-Pons P., Suda T., Fujimoto M. Y., and García-Berro E. *Astron. & Astrophys.*, 433:1037, 2005.

[99] Hernanz M. and José J. *New Astronomy Reviews*, 50:504–508, 2006.

[100] Ma Z. *et al. Phys. Rev. C*, 76:015803, 2007.

[101] José J., Hernanz M., Amari S., Lodders K., and Zinner E. *The Astrophysical J.*, 612:414–428, 2004.

[102] José J., Hernanz M., García-Berro E., and Gil-Pons P. The ^{25}Al(p,γ)^{26}Si Reaction Rate in Novae. In *Proceedings of the International Symposium on Nuclear Astrophysics-Nuclei in the Cosmos-IX*, CERN, Geneva, Switzerland, 25 - 30 June 2006.

[103] José J., Coc A., and Hernanz M. *The Astrophysical J.*, 520:347, 1999.

[104] Bardayan D. W. *et al.* 2007. to be submitted.

[105] Iliadis C., Champagne A., José J., Starrfield S., and Tupper P. *Astrophys. J. Suppl. Ser.*, 142:105–137, 2002.

[106] Clement P. R. C. *et al. Phys. Rev. Lett.*, 92:172502, 2004.

[107] Wiescher M., Görres J., Thielemann F. K., and Ritter H. *Astron. & Astrophys.*, 160:56, 1986.

[108] Iliadis C., Buchmann L., Endt P. M., Herndl H., and Wiescher M. *Phys. Rev. C*, 53:475, 1996.

[109] Galaviz D. *et al. Nucl. Phys. A*, 788:381c–384c, 2007.

[110] Wiescher M. and Görres J. *Z. Phys. A-Atomic Nuclei*, 329:121, 1988.

[111] *Table of Radioactive Isotopes.* Website. `http://ie.lbl.gov/toi/nuclide.asp?iZA=140026`.

[112] Anuj Ramesh Parikh. PhD thesis, Yale University, U.S.A, 2006.

[113] Caggiano J. A., Bradfield-Smith W., Lewis R., Parker P. D., and Visser D. *Phys. Rev. C*, 65:055801, 2002.

[114] Bardayan D. *et al. Phys. Rev. C*, 74:045804, 2006.

[115] Bardayan D. *et al. Nucl. Phys. A*, 718:505c–507c, 2003.

[116] Thomas J. C. *et al. Eur. J. Phys. A*, 21:419, 2004.

[117] Parpottas Y., Grimes S. M., Al-Quraishi S., Brune C. R., Massey T. N., and Oldendick J. E. *Phys. Rev. C*, 70:065805, 2004.

[118] Parpottas Y., Grimes S. M., Al-Quraishi S., Brune C. R., Massey T. N., Oldendick J. E., Salas A., and Wheeler R. T. *Phys. Rev. C*, 73:049907(E), 2006.

[119] Proposal for nuclear physics experiment at ri beam factory (ribf np-pac-01,2007). 2006. ^{25}Al + p Resonances through Elastic Scattering with CRIB, Spokesperson: Alan A. Chen.

[120] National superconducting cyclotron laboratory proposal form-pac 28. 2006. Measurement of ^{25}Al + p resonances with the p(^{27}Si,^{26*}Si)d reaction, Sopkesperson: Alan A. Chen.

[121] Seweryniak D., Woods P. J., Carpenter M. P., Davinson T., Janssens R. V. F., Jenkins D. G., Lauritsen T., and Lister C. J. *Phys. Rev. C*, 75:062801, 2007.

[122] Bardayan D. *et al. Phys. Rev. C*, 65:032801, 2002.

[123] *List of Levels for ^{26}Si.* Website. `http://www.nndc.bnl.gov/nudat2/getdataset.jsp?nucleus=26SI&unc=nds`.

[124] *Table of Radioactive Isotopes.* Website. `http://nucleardata.nuclear.lu.se/nucleardata/toi/listnuc.asp?sql=&A1=30&A2=30&Z=16`.

[125] Paddock R. A. *Phys. Rev. C*, 5:485, 1972.

[126] Caraça J. M. G., Gill R. D., Cox A. J., and Rose H. J. *Nucl. Phys. A*, 193:1, 1972.

[127] Kuhlmann E., Albercht W., and Hoffmann A. *Nucl. Phys. A*, 213:82, 1973.

[128] Yokata H., Fujioka K., Ichimaru K., Mihara Y., and Chiba R. *Nucl. Phys. A*, 383:298, 1982.

[129] Fynbo H. O. U. *et al. Nucl. Phys. A*, 677:38, 2000.

[130] Iliadis C., D'Auria J. M., Starrfield S., Thompson W. J., and Wiescher M. *Astrophys. J. Suppl. Ser.*, 134:151, 2001.

[131] Kevin I. Hahn. PhD thesis, Yale University, U.S.A, 1993.

[132] Hahn K. I. *et al. Phys. Rev. C*, 54:1999–2013, 1996.

[133] Hyder H. R. McK., Baris J., Gingell C. E. L., McKay C., Parker P. D., and Bromley D. A. *Nuclear Instruments and Methods in Physics Research A*, 268:285–294, 1988.

[134] Ashenfelter J. *PRAMANA Journal of Physics*, 59:713–717, 2002.

[135] *The ESTU-1 Tandem Van de Graaff Accelerator.* Website. `http://wnsl.physics.yale.edu/estu/`.

[136] Overley J. C. *et al. Nucl. Instr. Meth.*, 68:61, 1969.

[137] Rachel Lewis. PhD thesis, Yale University, U.S.A, 2005.

[138] Spencer J. E. and Enge H. A. *Nucl. Instr. Meth.*, 49:181, 1967.

[139] Glenn F. Knoll. *Radiation Detection and Measurement.* John Wiley and Sons, Inc., 2000.

[140] Cameron A. G. W. *The Astrophysical J.*, 121:144, 1955.

[141] Laguro M., Herwig F., Lattanzio J. C., Gallino R., and Straniero O. *The Astrophysical J.*, 586:1305–1319, 2003.

[142] Cameron A. G. W. *Astron. J.*, 65:485, 2002.

[143] Weigert A. *Z. Ap.*, 64:395, 1966.

[144] Schwarzschild M. and Härm R. *The Astrophysical J.*, 150:961, 1967.

[145] Jorissen A., Smith V. V., and Lambert D. L. *Astron. & Astrophys.*, 261:164, 1992.

[146] Becker S. A., Iben I. Jr., and Renzini A. *Dordrecht:Reidel*, page 141, 1981.

[147] Forestini M., Goriely S., Jorissen A., and Arnould M. *Astron. & Astrophys.*, 261:157, 1992.

[148] García-Hernádez D. A., García lario P., Plez B., Manchado A., D'Antona F., lub J., and Habing H. *Astron. & Astrophys.*, 462:711–730, 2007.

[149] Iben I. Jr. *The Astrophysical J.*, 260:821, 1982.

[150] Grundahl F., Briley M., Nissen P. E., and Feltzing S. *Astron. & Astrophys.*, 385:L14, 2002.

[151] David Arnett. *Supernovae and Nucleosynthesis.* Princeton University Press, 1996. p49.

[152] Iben I. Jr. and Truran J. W. *The Astrophysical J.*, 220:980, 1978.

[153] Renzini A. and Voli M. *Astron. & Astrophys.*, 94:175, 1981.

[154] Izzard R. G. *Mem. S.A.It.*, 75:754, 2004.

[155] Ugalde C. *et al. Nucl. Phys. A*, 758:577c–580c, 2005.

[156] Ugalde C. *et al. Phys. Rev. C*, 2007. to be submitted.

[157] Bao Z., Beer H., Käppeler F., Voss F., Wisshak K., and Rauscher K. *At. Data Nucl. Data Tables*, 76:70, 2000.

[158] Adelberger E. G. *et al. Rev. Mod. Phys.*, 70:1265, 1998.

[159] Iliadis C., D'Auria J. M., Starrfield S., Thompson W. J., and Wiescher M. *ApJS*, 134:151, 2001.

[160] Hale S. E., Champagne A. E., Iliadis C., Hansper V. Y., Powel D. C., and Blackmon J. C. *Phys. Rev. C*, 65:015801, 2002.

[161] Rowland C., Iliadis C., Champagne A. E., and Mosher J. *Phys. Rev. C*, 65:064609, 2002.

[162] Prantzos N. and Diehl R. *Phys. Rep.*, 267:1, 1996.

[163] G. J. Wasserburg and D. A. Papanastassiou. *Essays in nuclear astrophysics.* Cambridge Press, 1982.

[164] Lee T. *et al. Geophys. Res. Lett.*, 3:41, 1976.

[165] Lee T. *et al. The Astrophysical J.*, 211:L107, 1977.

[166] Lorin J. C. *et al. Meteoritics*, 12:299, 1977.

[167] Bradley J. G. *et al. J. Geophys. Res.*, 83:244, 1978.

[168] Esat T. M. *et al. Geophys. Res. Lett.*, 5:807, 1978.

[169] Lee T. *et al. The Astrophysical J.*, 228:L93, 1979.

[170] Mahoney W. A. *et al. The Astrophysical J.*, 334:L81, 1988.

[171] Oberlack U. *et al. Astron. & Astrophys. Suppl. Ser.*, 120:311, 1996.

[172] S. Pluschke *et al. Exploring the Gamma-Ray Universe: Proceedings of the Fourth INTEGRAL Workshop.* Cambridge Press, 2001.

[173] Smith D. M. *et al. The Astrophysical J.*, 583:L55, 2003.

[174] Diehl R. *et al. Nature*, 439:45, 2006.

[175] Kretschmer K. *et al. Astron. & Astrophys.*, 412:L47, 2006.

[176] ^{26}*Al All-Sky Map.* Website, 2005. `http://heasarc.gsfc.nasa.gov/docs/cgro/epo/posters/Greatest_Hits/COMPTEL_26Al.html`.

[177] Knodlseder J. *et al. The Astrophysical J.*, 510:915, 1999.

[178] PAlacios A. *Astron. & Astrophys. Suppl. Ser.*, 429:613, 2005.

[179] Mowlavi N. and Meynet G. *Astron. & Astrophys.*, 361:959, 2000.

[180] José J. *et al. The Astrophysical J.*, 479:L55, 1997.

[181] Higdon J. C. *et al. The Astrophysical J.*, 611:L29, 2004.

[182] Timmes F. X. *et al. The Astrophysical J.*, 449:204, 1995.

[183] Wesley K., Baron E., and Branch D. (arXiv:astro-ph/07054086), 2007.

[184] Gianni Fiorentini and Alessandro Pascolini.

[185] Hack M., Selvelli P., and Duerbeck H. W. Classical novae and recurrent novae: General properties. In Hack M., Ladous C., Jordan S. D., Thomas R. N., Goldberg L., and Pecker J. C., editors, *NASA, Washington, Cataclysmic Variables and Related Objects p 261-369 (SEE N95-27068 09-89)*, September 1993. `http://adsabs.harvard.edu/abs/1993cvro.nasa..261H`, Provided by the Smithsonian/NASA Astrophysics Data System.

[186] José J., Hernanz M., and Iliadis C. *Nucl. Phys. A*, 777:550–578, 2006.

[187] Runkle R. C., Champagne A. E., and Engel J. *The Astrophysical J.*, 556:970–978, 2001.

[188] Swartz K. B. *et al. Nucl. Instr. Meth. Phys. Res. A*, 463:354, 2001.

[189] *Jam.* Website. `http://sourceforge.net/projects/jam-daq`.

[190] Lee T., Papanastassiou D. A., and Wasserburg G. J. *Astrophys. J.*, 211:L107, 1977.

[191] Anders E. and Zinner E. *Meteorites*, 28:490, 1993.

[192] Ott U. *Nature (London)*, 365:25, 1993.

[193] Koehler P. E., Kavanagh R. W., Vogelaar R. B., Gledenov Yu. M., and Popov Yu. P. *Phys. Rev. C*, 56:1138, 1997.

[194] Amari S., Gao X., Nittler L. R., Zinner E., José J., Hernanz M., and Lewis R. S. *Astrophys. J.*, 551:1065, 2001.

[195] Amari S. *New Astronomy Reviews*, 46:519–524, 2002.